DOCTORAL THESIS

Simulation of Neutron Rich Isotopes at Beta Decay Station in SPES

Author:
Marco Perri

Supervisor:
Alessandro Saltarelli

July 5, 2023

Contents

Introduction

The aim of this thesis is to explore the capabilities of the beta decay station to be installed at the LNL for the study of the decay of radioactive nuclei produced at the ISOL facility SPES. The β-decay station will perform γ and β energy measurements of exotic ions implanted on a moving tape. Studying the beta decay of exotic isotopes provides crucial insights into nuclear structure, astrophysical processes, fundamental interactions, and the limits of our current understanding of the universe. It helps advance our knowledge in various scientific disciplines and contributes to both fundamental research and practical applications. In particular, these kind of measurements offer the possibility to test and probe the limits of the Standard Model of particle physics and help in understanding the processes that occur in stars, such as nucleosynthesis. Moreover, beta decay studies have practical implications that extend to fields such as nuclear medicine, where they contribute to the advancement of imaging techniques and cancer treatment methods.

Unfortunately, due to delays that have accumulated in recent years in the implementation of measurement devices, largely caused by COVID and technical difficulties encountered, the first beams will not be ready until the end of next year to make a real experiment. So this thesis is basically focused on the performance simulation of the experimental apparatus, which is preliminary mounted in the experimental room of the SPES building, waiting to be connected on the SPES RIBs beam line.

We have simulated an experiment with ^{148}Cs isotopes, that was already realized at ISOLDE (CERN) radioactive ion beam (RIB) facility in 2016, in order to investigate the region of n-rich Ba nuclei, which is known to exhibit strong octupole correlations. GEANT4 built-in radioactive decay option do not consider β decays with delayed neutron emission and furthermore the database may not be entirely up to date for exotic isotopes. To this purpose,

we have first built four Wolfram Mathematica software, that shoul be run in advance of the simulation, with the purpose of obtaining as much information as possible for an exhaustive simulation. Given an ion of interest, the four software are capable of finding a complete list of all the decay processes, optimize the measuring and implantation time windows, the radioactive activities left on the tape and finally calculating the conversion coefficients to update the GEANT4 database. The simulation have provided satisfying results and we expect it to became a useful tool that can help to better understand the measurements that will be performed in the future, once the beta decay station will be fully operational.

This PhD project was done also in collaboration with CAEN S.p.A, in Appendix A is described the CAEN A5202 board and in particular its performance in γ spectroscopy. The A5202 board in an application specific integrated circuit (ASIC) based front end, optimized to work in conjunction with silicon photo multipliers (SiPM). ASIC technology strength lays in the possibility of accommodating a large number of acquisition channel in reduced dimensions and with low power consumption. The ASIC chip employed is the Citiroc-1A, which performs energy acquisition through a pulse height analysis algorithm. The Citiroc-1A have been used to take measurements with a 6x6x15 mm3 Cerium-doped Lutetium Yttrium Orthosilicate (LYSO(Ce)), Caesium Iodine (CsI) and Bismuth Germanate (BGO) paired with a single 6x6 mm^2 SiPM and ^{22}Na, ^{137}Cs and ^{60}Co radioactive sources. The energy resolution of the photopeaks are comparable with what obtained with the same crystal, radioactive source and a charge integration digitizer (CAEN DT5720A) and whith results found on literature. The results obtained are discussed in further detail in ref. [1]. In the future, the beta decay station in SPES will also include scintillator arrays for neutron measurements in order to have a better understanding of the decaying isotopes, and the A5202 can be suitable set-up for this kind of measurements.

Chapter 1

Nuclear Decay

1.1 Introduction

In this chapter, we will introduce some theoretical concepts to use in the construction of our simulation, as well as to describe the beta decay station and the SPES project. We will first introduce the basic principles of radioactive decay, through which we derive the Bateman equations to evaluate the population in a radioactive decay chain [2]. Then, we introduce the nuclear fission mechanism, since the isotopes provided by SPES beams are produced through proton-induced fission on uranium carbide (UC_x) targets [3].

Finally, we provide a detailed description of β-decay mechanism, with a focus on allowed and forbidden transitions, as well as in the case of a β-decay into an excited state of the daughter nuclide [4].

1.2 Decay of a Radioactive Nucleus

Consider a collection of $N_A(t)$ identical atoms, and let λ (s^{-1}) be the radioactivity constant, which represents the probability that any of the atoms will decay per unit time. The activity of a radioactive substance is defined as the total number of decays per unit time, which is given by $N_A(t) \times \lambda$. The rate of decay is described by the differential equation:

$$\frac{dN_A(t)}{dt} = -N_A(t)\lambda, \tag{1.1}$$

where the minus sign indicates that the number of atoms is decreasing with time. If we assume that the probability of decay for each atom is independent of its age, then we can integrate Eq. 1.1 to obtain:

$$\int \frac{dN_A(t)}{N_A(t)} = -\int \lambda dt. \tag{1.2}$$

The number of atoms at time $t = 0$ is $N_A(0)$, and the solution to Eq. 1.2 is:

$$\ln \frac{N_A(t)}{N_A(0)} = -\lambda t, \tag{1.3}$$

which can be rewritten as an exponential:

$$N_A(t) = N_A(0)e^{-\lambda t}, \tag{1.4}$$

where $N_A(0)$ is the initial number of atoms in the substance. Eq. 1.4 provides the number of atoms at any time in a radioactive substance composed of $N_A(0)$ atoms at $t = 0$, under the assumptions that the radioactive constant λ is the same for all atoms and independent of time. By recalling the definition of activity, Eq. 1.4 can be expressed in terms of activity by multiplying both sides by λ:

$$\frac{N_A(t)\lambda}{N_A(0)\lambda} = e^{-\lambda t}, \tag{1.5}$$

where the numerator on the left-hand side is the activity at time t, and the denominator is the activity at time $t = 0$.

In reality, many radioactive nuclides can decay through multiple alternative modes, such as ^{152}Eu, which can decay via electron or positron emissions. In such cases, the probability of each decay mode per unit time is denoted by λ_1, λ_2, λ_3, and so on, and the total radioactive constant is the sum of these quantities:

$$\lambda = \lambda_1 + \lambda_2 + \lambda_3 + \dots \tag{1.6}$$

If we consider a group of N_A nuclides with multiple decay modes, the "partial activity," or the activity of a single decay mode, is given by:

$$\frac{dN_{A_i}(t)}{dt} = \lambda_i N_A(t) = \lambda_i N_A(0) e^{-\lambda t}, \tag{1.7}$$

while the total activity is the sum of the partial activities:

$$\frac{dN_A(t)}{dt} = \sum_i \frac{dN_A(t)}{dt}_i = N_A(t) \sum_i \lambda_i = \lambda N_A(0) e^{-\lambda t}. \tag{1.8}$$

1.2.1 Radioactive Daughter Product

Let's consider now a radioactive nuclide A that decays to a daughter nuclide B, which subsequently decays to nuclide C, with decay constants λ_A and λ_B, respectively. The variation B nuclei at any point in time can be expressed as:

$$\frac{dN_B(t)}{dt} = N_A(t)(\lambda_A - N_B(t)\lambda_B) \tag{1.9}$$

Here, N_A and N_B represent the number of atoms of nuclides A and B, respectively. Equation 1.9 indicates that the rate of change of B atoms is equal to the supply of B from the decay of A nuclide, minus the B nuclides which decay themselves. If λ_B is zero, then B is a stable nuclide. If the only source of supply of B is A, and at $t = 0$ there are $N_A(0)$ atoms, then $N_A = N_A(0)e^{-\lambda_A t}$ and we obtain:

$$\frac{dN_B(t)}{dt} = N_A(0)\lambda_A e^{-\lambda_A t} - N_B(t)\lambda_B. \tag{1.10}$$

The general solution for Eq. 1.10 is:

$$N_B(t) = N_A(0)(h_A e^{-\lambda_A t} + h_B e^{-\lambda_B t}) \tag{1.11}$$

Here, the coefficients h_A and h_B are given by:

$$\begin{cases} h_A = \frac{\lambda_A}{\lambda_B - \lambda_A} \\ h_B = -h_A \end{cases}$$

The coefficients h_A and h_B are obtained from Eqs. 1.11 and 1.10 with the initial condition that $N_B(t) = 0$ at $t = 0$. The general solution is then:

$$N_B(t) = N_A(0)\frac{\lambda_A}{\lambda_B - \lambda_A}(e^{-\lambda_A t} - e^{-\lambda_B t}) \tag{1.12}$$

At this point, the activity of B is given by:

$$N_B(t)\lambda_B = N_A(t)\lambda_A \frac{\lambda_A}{\lambda_B - \lambda_A}(1 - e^{-(\lambda_B - \lambda_A)t}). \tag{1.13}$$

The maximum number of daughter atoms is reached at a specific time t_m at which the rate of change of $N_B(t)$ is zero, or in other words when the derivative of $N_B(t)$ respect to time is zero. Mathematically, this can be expressed as:

$$\left.\frac{dN_B(t)}{dt}\right|_{t=t_m} = 0 = -\lambda_A e^{-\lambda_A t_m} + \lambda_B e^{t_m} \tag{1.14}$$

Solving for t_m yields:

$$t_m = \frac{\ln\left(\frac{\lambda_B}{\lambda_A}\right)}{(\lambda_B - \lambda_A)}. \tag{1.15}$$

Alternatively, the time t_m can be expressed in terms of the mean life τ and the half-life period T as:

$$t_m = \tau_B \frac{T_A}{T_A - T_B} \ln\left(\frac{T_A}{T_B}\right). \tag{1.16}$$

Here, τ_B represents the mean life of the daughter nuclide B, and T_A and T_B are the half-life periods of the parent and daughter nuclides, respectively. Fig. 1.1 is a graph showing the change in population in time for ^{148}Cs (blue) and its daughter nucleus ^{148}Ba (orange), with the population of ^{148}Cs normalized to one at t = 0 s. The half lives of ^{148}Cs and ^{148}Ba are 146 ms and 612 ms respectively, in the example the daughter nucleus reaches the maximum population at t_m = 0.40 s.

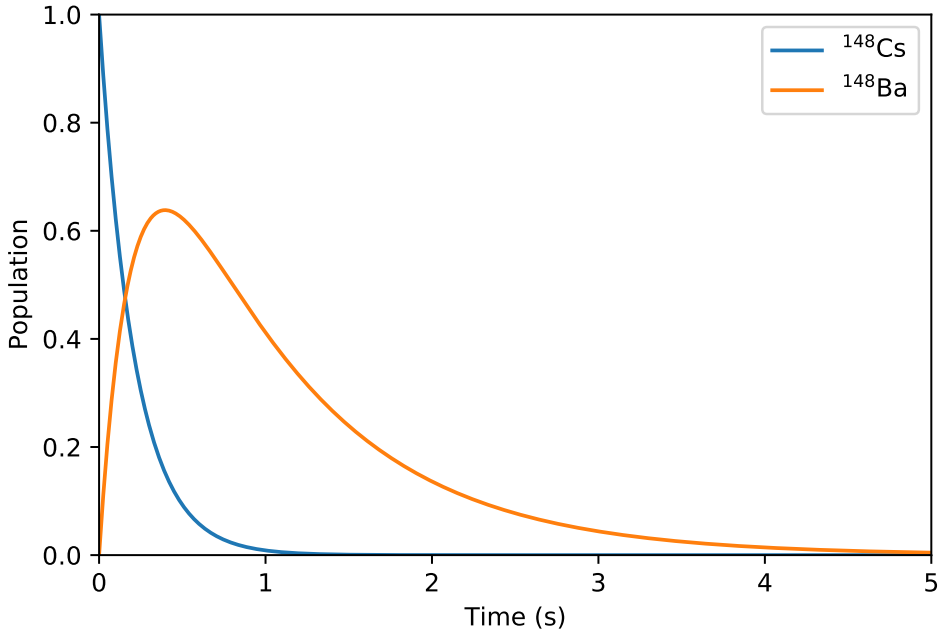

FIGURE 1.1: Change in population in time for ^{148}Cs (blue) and its daughter nucleus ^{148}Ba (orange), with the population of ^{148}Cs normalized to one at t = 0 s.

1.2.2 General Radioactive Decay Growth

Let us now consider a scenario in which not only the daughter nuclide, but also the granddaughter nuclide continues to decay. We denote the daughter species as C, N_C as the number of C atoms and λ_C as the radioactive constant. The rate of change of C is similar to the case of the daughter atom B and can be expressed as:

$$\frac{dN_C(t)}{dT} = N_B(t)\lambda_B - N_C(t)\lambda_C \tag{1.17}$$

Here, at the beginning, only A atoms are present and so, at $t = 0$, $N_A(t) = N_A(0)$, $N_B(0) = 0$ and $N_C(0) = 0$. In this scenario, the solution to equation 1.17 is:

$$N_C(t) = N_A(0)(h_A e^{\lambda_A} + h_B e^{-\lambda_B t} + h_C e^{\lambda_C t}) \tag{1.18}$$

Here, the coefficients h are defined as:

$$\begin{cases} h_A = \frac{\lambda_A}{\lambda_C - \lambda_A}\frac{\lambda_B}{\lambda_B - \lambda_A} \\ h_B = \frac{\lambda_A}{\lambda_A - \lambda_B}\frac{\lambda_B}{\lambda_C - \lambda_B} \end{cases}$$

If $N_C(t) = 0$ at $t = 0$, from $h_A + h_B + h_C = 0$ follows that h_C is:

$$h_C = \frac{\lambda_A}{\lambda_A - \lambda_C}\frac{\lambda_B}{\lambda_B - \lambda_C} \tag{1.19}$$

The activity of species C can then be expressed as:

$$N_C(t)\lambda_C = N_A(0)\lambda_A\left(\frac{\lambda_B}{\lambda_B - \lambda_A}\frac{\lambda_C}{\lambda_C - \lambda_A}e^{-\lambda_A t} + \frac{\lambda_B}{\lambda_A - \lambda_B}\frac{\lambda_C}{\lambda_C - \lambda_B}e^{-\lambda_B t}\right. \tag{1.20}$$

$$\left. + \frac{\lambda_B}{\lambda_B - \lambda_C}\frac{\lambda_C}{\lambda_A - \lambda_C}e^{-\lambda_C t}\right)$$

Equations 1.5, 1.13 and 1.20 have been generalized for a decay chain with several species by Bateman [5]. Consider the case where there are N_{A_0} nuclei at $t = 0$ which then decay in the chain to species A, B, C, ..., M and N, with radioactive constants λ_A, λ_B, λ_C, ..., λ_N, then at any time, the rate of change in the population of species N is:

$$\frac{dN_N}{dt} = N_M\lambda_M - N_N\lambda_N \tag{1.21}$$

where M is evaulated in a similar way as previously explained. To determine the population of a particular radioactive species at any given time t, we must integrate equation 1.21 as previously explained. The resulting population is given by the Bateman equation:

$$N_N = N_{A0}(h_A e^{-\lambda_A t} + h_B e^{-\lambda_B t} + ... + h_N e^{-\lambda_N t}) \tag{1.22}$$

where the coefficients h_i are given by:

$$h_i = \frac{\lambda_A}{\lambda_A - \lambda_i}\frac{\lambda_B}{\lambda_B - \lambda_i}...\frac{\lambda_M}{\lambda_M - \lambda_i} \tag{1.23}$$

for $i = A, B, ..., N$. It is important to note that the sum of all coefficients must be equal to zero to satisfy the initial condition that $N_N = 0$ at $t = 0$:

$$h_A + h_B + ... + h_M + h_N = 0 \tag{1.24}$$

The Bateman equation can be used to determine the activity of a radioactive species in various scenarios, such as the amount of a particular radioactive product produced after nuclear bombardment, or the radioactive activity in a decay chain at a specific time t. In cases where the primary radioactive source is removed, the Bateman equation can still be used to calculate the number of atoms of a particular species N_N, since the supply of N atoms is provided by the independent decay of the previous species A, B, and so on,

as described by the Bateman equations. Mathematically, we can express the activity of N as:

$$N_N(t)\lambda_N = (\text{growth from } A_0) + ... + (\text{growth from } M_0) + (\text{residue of } N_0). \tag{1.25}$$

In summary, the Bateman equations can be applied to various scenarios involving radioactive decay and accumulation, regardless of the initial conditions.

1.3 Fissions Processes

In this work, our primary focus will be on β decay and nuclear fission. The reason for this is that the nuclides of interest for the SPES facity at the LNL laboratories is predominantly produced through the fission of uranium carbide targets and isotopes that primarily undergo β^- decay [3]. We will delve into greater detail on this topic later in our discussion.

1.3.1 Spontaneus Fission

In nuclear fission reactions a nucleus is split into two fragments, in general with different masses and the process can be described in the following way:

$$^{A_p}X_{Z_p} \longrightarrow ^{A_D^1}Y_{Z_D^1} + ^{A_D^2}Z_{Z_D^2} \tag{1.26}$$

with

$$\begin{cases} Z_p = Z_D^1 + Z_D^2 \\ A_p = A_D^1 + A_D^2 \end{cases}$$

where A_p and Z_p are the mass and proton numbers of the fissioning nucleus, while A_D and Z_D of the daughters. The most simple case is the symmetric fission, where the daughters have the same Z and A

$$(A_p, Z_p) \longrightarrow 2(\frac{A_p}{2}, \frac{Z_p}{2})$$

In order to understand this process we must first introduce the Q-value of a reaction. The Q-value is the amount of energy absorbed or released during a nuclear reaction and, from the conservation of energy and the mass energy equivalence, it follows that the Q-value can be defined as:

$$Q = K_f - K_i = (m_i - m_f)c^2 \tag{1.27}$$

where K_f and K_i are the initial and final kinetic energies, while m_i and m_f are the initial and final masses. In case of spontaneous reactions the Q-value is a positive quantity, otherwise the reaction is endothermic and requires an energy input to happen. According to the liquid drop model, the binding energy of a nucleus can be broken down into several components, including the surface energy (which arises due to the fact that the nucleons at the surface of the nucleus are not as tightly bound as those in the inner part of the nucleus), the Coulomb energy (which arises due to the electrostatic repulsion between protons), and the volume energy (which arises due to the strong nuclear force that holds the nucleons together). The Weizsäcker formula for the binding energy in the liquid drop model is:

$$B(A,Z) = -\frac{E(A,Z)}{A} = b - \frac{c}{A^{\frac{1}{3}}} - d\frac{Z(Z-1)}{A^{\frac{4}{3}}} - e\frac{(A-2Z)^2}{A^2} - f(-1)^{Z+1}\frac{1+(-1)^A}{2A^{\frac{3}{2}}}. \tag{1.28}$$

where b, d, e and f are coefficient found empirically. The last two terms are the asymmetry and pairing terms and can be neglected in the symmetric case

we are considering now. The Q-value in terms of the Weizsäcker formula for nuclear fission in the symmetric case is:

$$Q = 2\left[b\frac{A_p}{2} - c(\frac{A_p}{2})^{\frac{2}{3}} - d\frac{Z_p}{2}(\frac{Z_p}{2}-1)(\frac{A_p}{2})^{-\frac{1}{3}} - e(\frac{Z_p}{2}-\frac{N_p}{2})^2(\frac{A_p}{2})^{-1}\right] \tag{1.29}$$

$$-[bA_p - cA^{\frac{2}{3}} - dZ_p(Z_p-1)A_p^{-\frac{1}{3}} - e(Z_p-N_p)^2A_p^{-1}]$$

once we simplify the equal terms in the equation we obtain

$$Q = \left[c\cdot A_p^{\frac{2}{3}} + d\cdot Z_p\cdot(Z_p-1)\cdot A^{-\frac{2}{3}}] - 2\cdot[c\cdot(\frac{A_p}{2})^{\frac{2}{3}} + d\cdot\frac{Z_p}{2}\cdot(\frac{Z_p}{2}-1)\cdot(\frac{A_p}{2})^{\frac{1}{3}}\right]$$

$$Q = c\cdot A^{\frac{2}{3}}\cdot(1-2^{\frac{1}{3}}) + d\cdot\frac{Z_p}{A^{\frac{1}{3}}}\cdot[(1-2^{-\frac{2}{3}}\cdot Z_p + (2^{\frac{1}{3}}-1]$$

$$Q = d\cdot Z_p\cdot A_p^{-\frac{1}{3}}\cdot[0.37\cdot Z_p + 0.26]\cdot c\cdot 0.26\cdot A_P^{\frac{2}{3}}. \tag{1.30}$$

Since the Q value must be positive and $Z_p \sim \frac{A_p}{3}$ we obtain

$$Q = (\frac{d}{3})\cdot[0.37\cdot(\frac{A_p}{3}) + 0.26] - c\cdot 0.26 > 0$$

$$A_p > \frac{3}{0.37}\cdot(\frac{0.78\cdot c}{d} - 0.26) \sim 157. \tag{1.31}$$

Eq. 1.31 demonstrate that all isotopes with mass $A_p > 157$ could decay by spontaneous symmetric fission and, in Fig 1.2 the isotopes enclosed in the dotted line should satisfy the condition for spontaneous symmetric fission. In principle, the spontaneous fission has a probability of happening different from zero only for nuclides with $Z_p^2/A_p \geq 40$. However, it is also

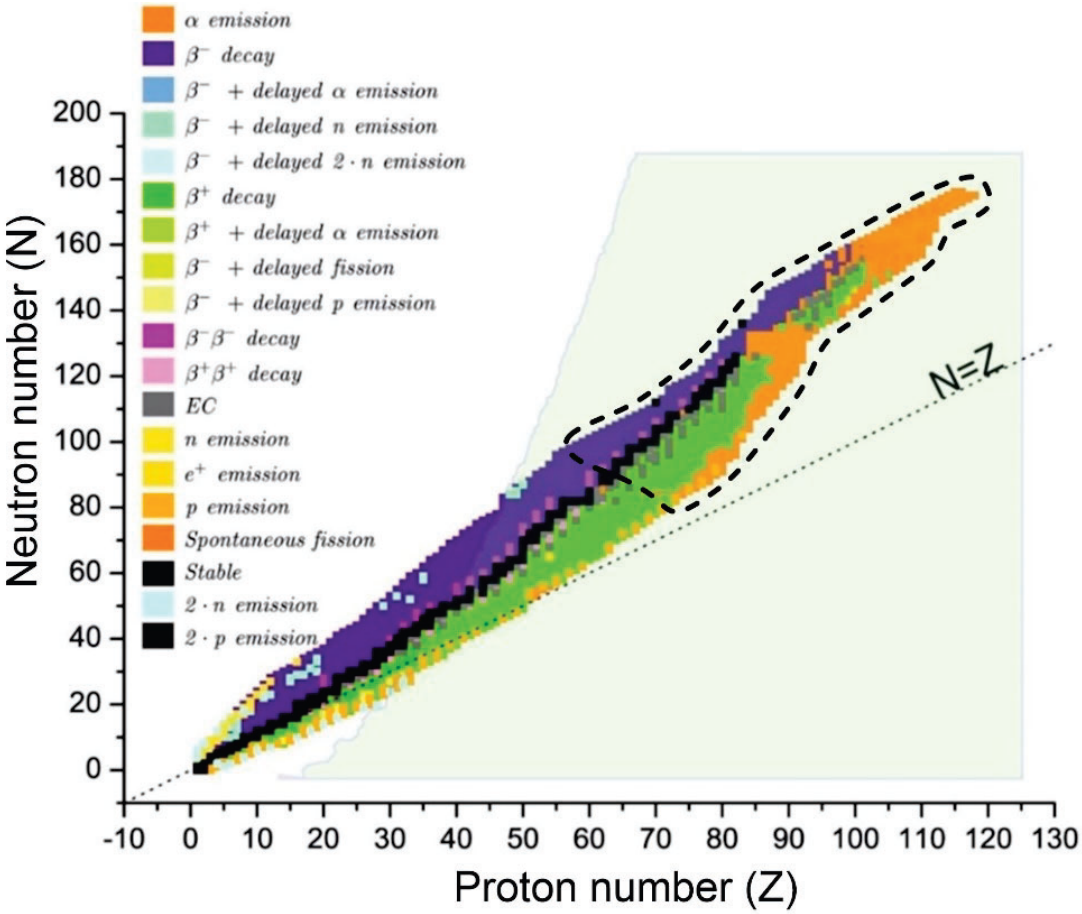

FIGURE 1.2: Nucilde chart, the isotopes enclosed in the dotted line satisfy the condition for spontaneous symmetric fission. Image taken from Alessandro Saltarelli *"Lectures on Nuclear Physics"*.

possible among actinides but the decay rate are negligible respect to other decay modes, some examples of actinineds spontaneous fission half lives, compared with half lives of other decays are shown in Tab.1.1.

In order to properly describe the nuclear fission process, we must not consider the nuclei perfectly spherical like in the liquid drop model. In fact there are evidences that especially high masses nuclei have deformed surfaces (Fig. 1.3). In the simplest case they are ellipsoidal shaped with symmetry along the axis. When the fission process happens, the nucleus deforms as the two ends split away into two fragments. This process is caused by the

Nuclide	$T_{\frac{1}{2}}$ (years) spontaneous fission	$T_{\frac{1}{2}}$ (years)	Z_p^2/A_p
235-Uranium	3.5×10^{17}	7.04×10^8	36
238-Uranium	8.4×10^{15}	4.47×10^9	35.6
237-Neptunium	3×10^{18}	2.144×10^6	36.5
241-Americium	1.14×10^{14}	432	37.4
244-Curium	10^7	181	37.8
248-Californium	3×10^4	0.9	38.7
252-Californium	2.65	2.65	38.1

TABLE 1.1: Table showing actinides spontaneous fission half lives compered to the half lives of their alternate decay mode.

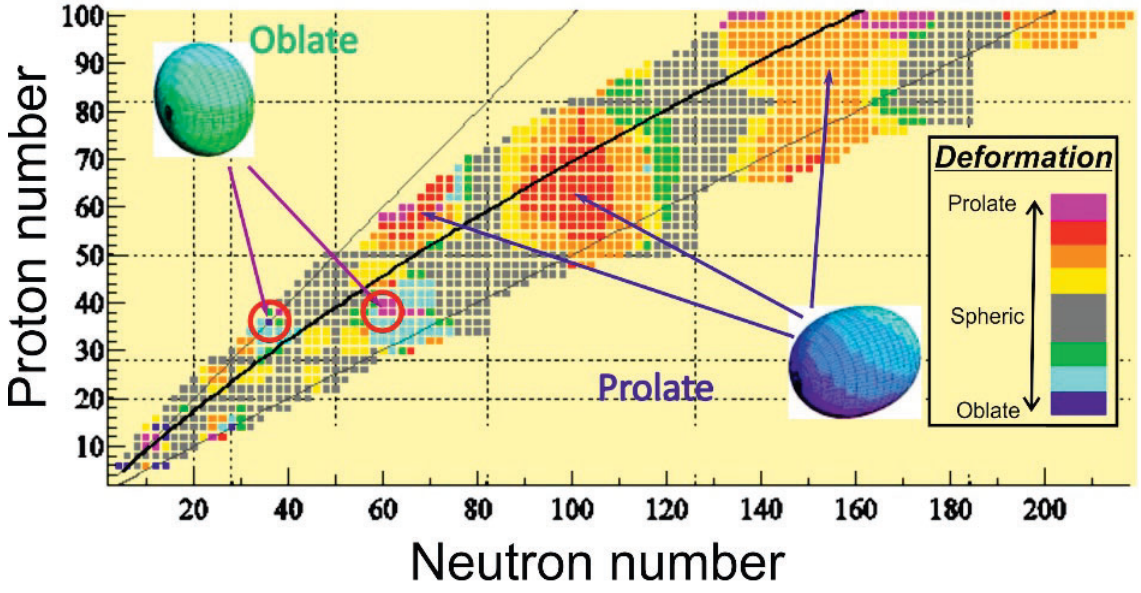

FIGURE 1.3: Nuclear deformation as a function of the proton and neutron number. Image taken from Alessandro Saltarelli *"Lectures on Nuclear Physics"*.

fact that the nuclear attraction forces acts at short distance, while the Coulombian repulsion is long range. We can then describe the nuclear fission with the presence of barrier that strongly opposes the deformation, where the nucleus can undergo spontaneous fission process through tunnel effect, as it is described in Fig. 1.4. During the fission the nucleus loses, little by little, its spherical shape, elongating increasingly, until it becomes energetically more convenient to split into two fragments. Along the two heavy fragments, neutrons are also emitted during the nuclear fission, so the entire process can be described as:

$$ {}^{A_p}X_{Z_p} \longrightarrow {}^{A_D^1}X_{Z_D^1} + {}^{A_D^2}X_{Z_D^2} + \kappa \cdot n \tag{1.32} $$

with

$$ \begin{cases} Z_p = Z_D^1 + Z_D^2 \\ A_p = A_D^1 + A_D^2 + \kappa \end{cases} $$

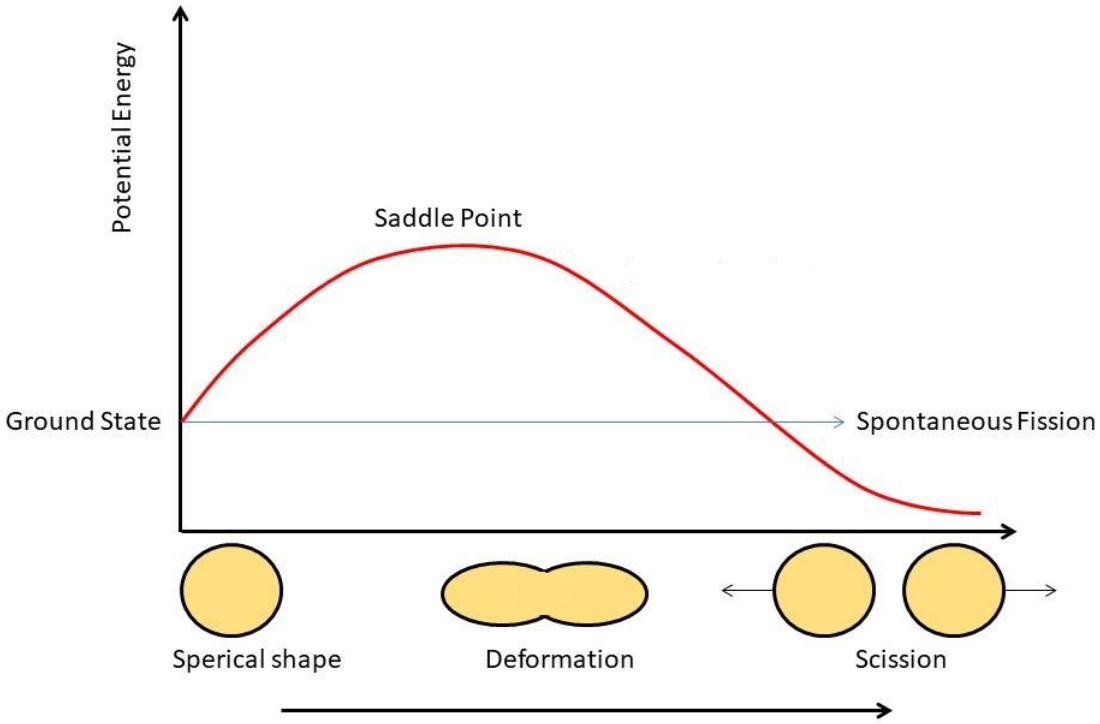

FIGURE 1.4: Potential energy in the fission process as a function of the distance between the two fragments. Image taken from Alessandro Saltarelli *"Lectures on Nuclear Physics"*.

The yield of the fission is the probability of emission of the fragments and it is strongly dependent on the father nucleus and on the excitation energy of the fissioning system. The yield of fission usually leads to a binary distribution, with the two peaks centered around the two most probable masses emitted. For example in the case of ^{252}Cf the two most probable fragments are ^{106}Ru and ^{142}Xe. Fig. 1.5 shows the yield of ^{106}Ru and ^{142}Xe as obtained in

ref. [6], along with the decay chain of the resulting fragments in the bottom panel .

The yield of the fission is reproduced analytically by:

$$Y_{proj}[A] = \frac{N}{\sqrt{2\pi}\sigma}(e^{-\frac{(A-A_D^1)^2}{2\sigma^2}} + e^{-\frac{(A-A_D^2)^2}{2\sigma^2}}) \tag{1.33}$$

The parameters N, A_D^1, A_D^2 and σ, in the case we were considering of ^{252}Cf have been found through a fit and are reported in Tab.1.2

$^{252}_{154}Cf_{98}$ parameters	
N	4.44
A_D^1	107
A_D^2	142
σ	6.135

TABLE 1.2: Parameters for the yield of ^{252}Cf.

The number of neutrons emitted in the fission, also called prompt neutrons, instead can be regarded as a poisson distribution, as well as their kinetic energy as can be seen in Fig. 1.6.

Let's consider now a generic fission process

$$A_p \longrightarrow A + (A_P - A - \kappa) + \kappa \tag{1.34}$$

where A is the mass of the first fragment, A_p is the mass of the father and κ represents the neutron emitted. The emission probability of the fragment $^{A_D^1}Y_{Z_D^1}$ and the κ neutrons are

$$Y_{corr}[A,\kappa] = Y_{proj}[A] \cdot P[\kappa, \overline{\nu_{pt}}] = \frac{N}{\sqrt{2\pi}\sigma}(e^{-\frac{(A-A_D^1)^2}{2\sigma^2}} + e^{-\frac{(A-A_D^2)^2}{2\sigma^2}})\frac{\overline{\nu^\kappa pt} \cdot e^{-\overline{\nu^\kappa pt}}}{\kappa!} \tag{1.35}$$

It only remains to add how the yield Y_{corr} varies with Z. Since the fission probability will be greater if the Coulomb repulsion is strong, then Y_{corr} will be proportional to Z. The fission yield can then be expressed as:

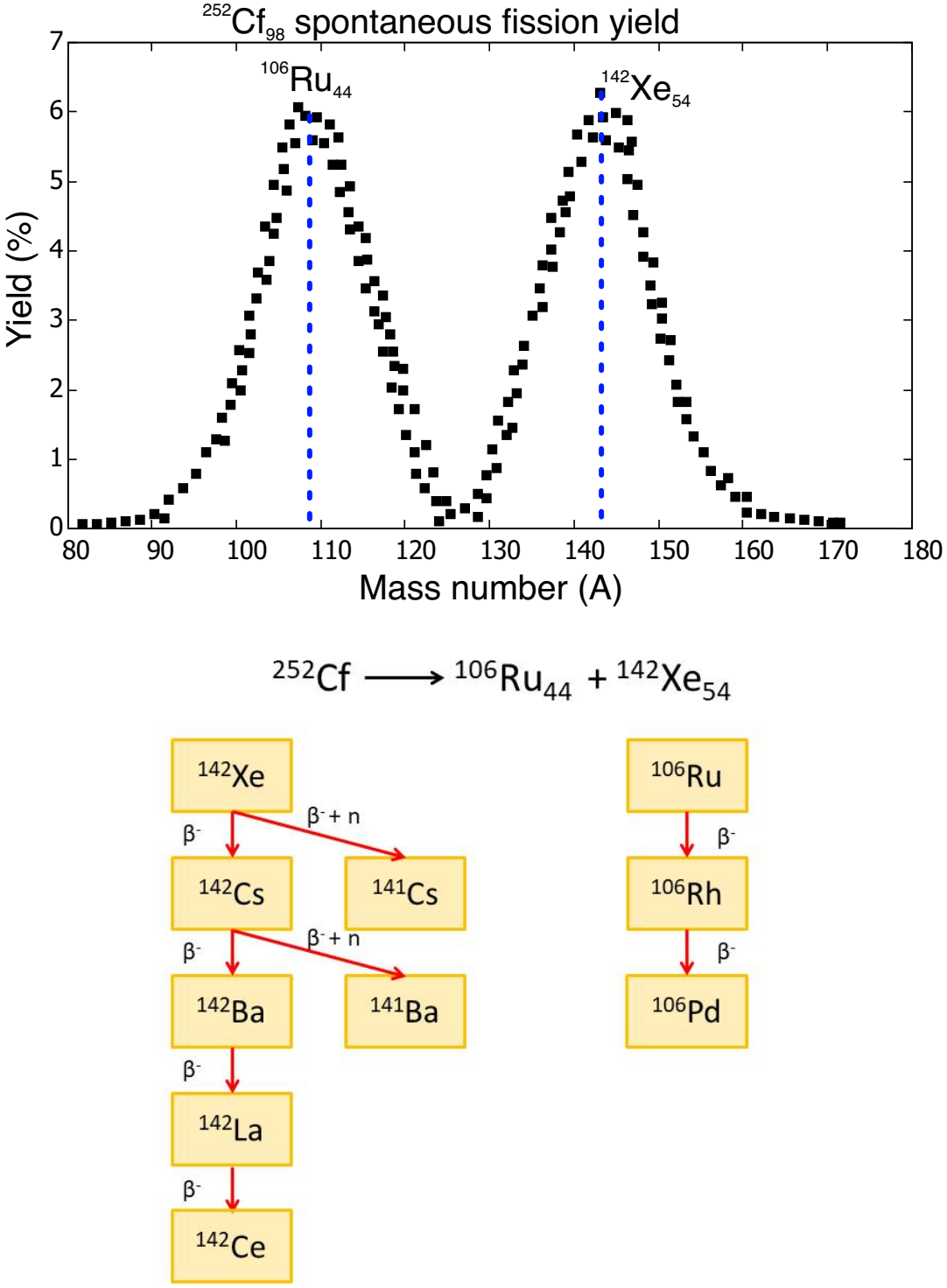

FIGURE 1.5: The upper panel shows the fission yield of $^{2}52$Cf as obtained in ref. [6]. The Bottom panel shows the decay of the ^{252}Cf fragments through β^-, β^- + n and α decays.

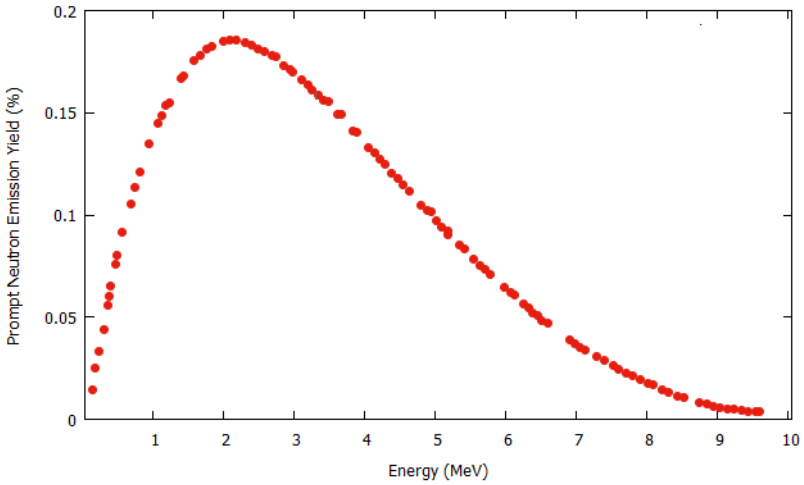

FIGURE 1.6: Prompt neutron energy distribution for the spontaneous fission of ^{252}Cf.

$$Y_{corr}[A,Z,\kappa] = \frac{Z\cdot(Z_p - Z)}{\sum_{Z\in Isotopes[A]} Z\cdot(Z_p - Z)} Y_{corr}[A,\kappa] \tag{1.36}$$

and it follows that the mean energy emitted in the fission process is

$$\overline{E_{fiss}} = \kappa\cdot\overline{K_n} + \sum_{A,Z,\kappa}[E(A_p,Z_p) - E(A,Z) - E(E_p - A - \kappa, Z_p - Z)]\cdot Y_{corr}[A,Z,\kappa] \tag{1.37}$$

1.3.2 Particle induced fission

It is possible to increase the fission probability of heavy atoms by proton or neutron absorption. Fig. 1.7 shows the cross section, for thermal neutron capture, against the atomic number for various actinides. The most common cases are the thermal neutron fission induced in ^{235}U and ^{238}U. It is actually worth noting that while the neutron capture process widely increases the fission rate for ^{235}U, it is not the case for ^{238}U. In fact, the neutron absorption process for ^{235}U produces ^{236}U* in an excited state with energy $E^*_{239_U}$ = 6.5 MeV, while ^{238}U becomes ^{239}U with energy $E^*_{236_U}$ = 4.8 MeV. In the first case, the nucleus ^{235}U undergoes a transition from an odd-even to an even-even

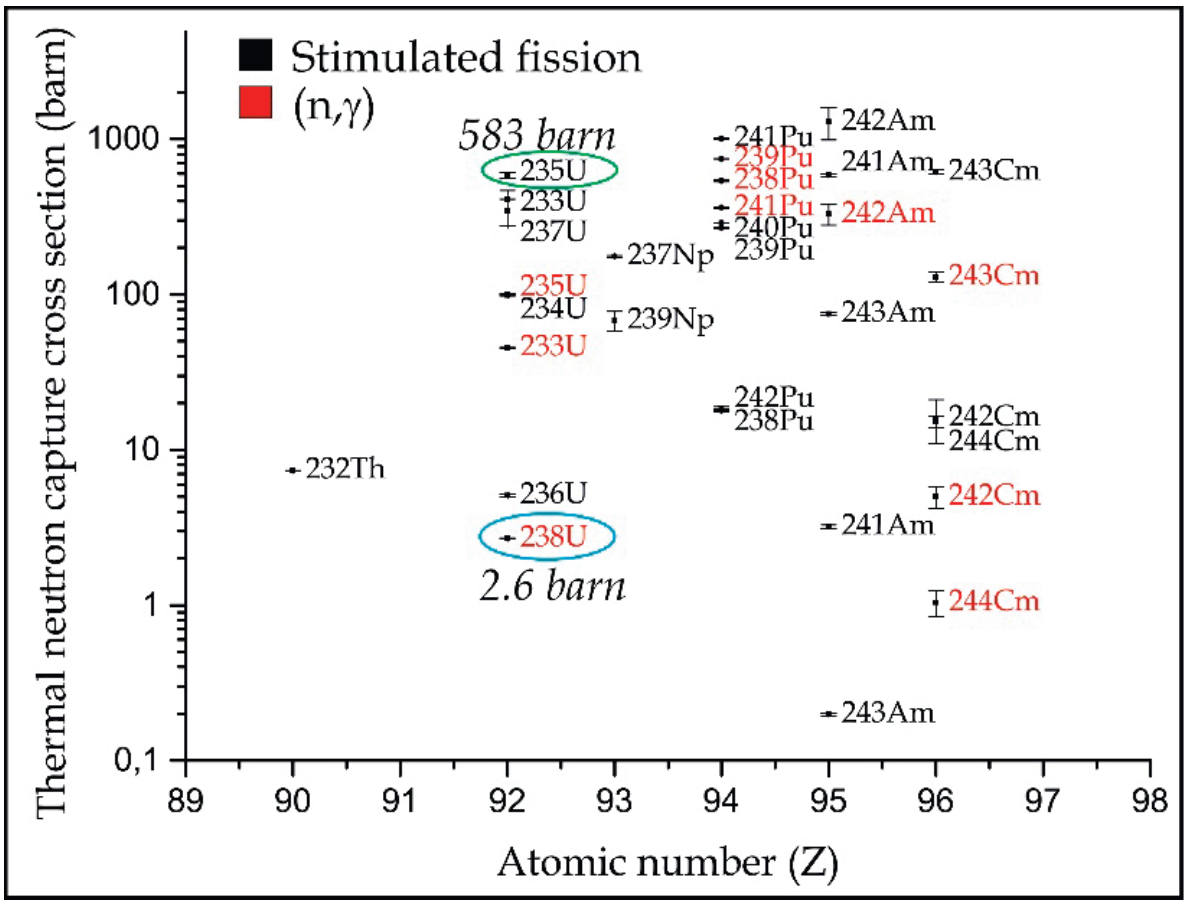

FIGURE 1.7: Cross section for neutron capture in different actinides. Image taken from Alessandro Saltarelli *"Lectures on Nuclear Physics"*.

configuration, where even-even nuclei generally exhibit higher binding energies. The Weizsäcker formula provides a quantitative measure of this effect, yielding an excitation energy of 6.5 MeV for the resulting ^{236}U nucleus.

$$E_{236_U} = |E_{Even-Even}(92.236)| - |E_{odd}(92.236)| = 6.5MeV$$

Conversely, in the second case, the target nucleus has an even number of protons and neutrons, which leads to a decrease in the coupling term in the Weizsäcker formula and a smaller difference in binding energies between the target and compound nuclei. This yields an excitation energy of 4.8 MeV for the resulting ^{239}U nucleus.

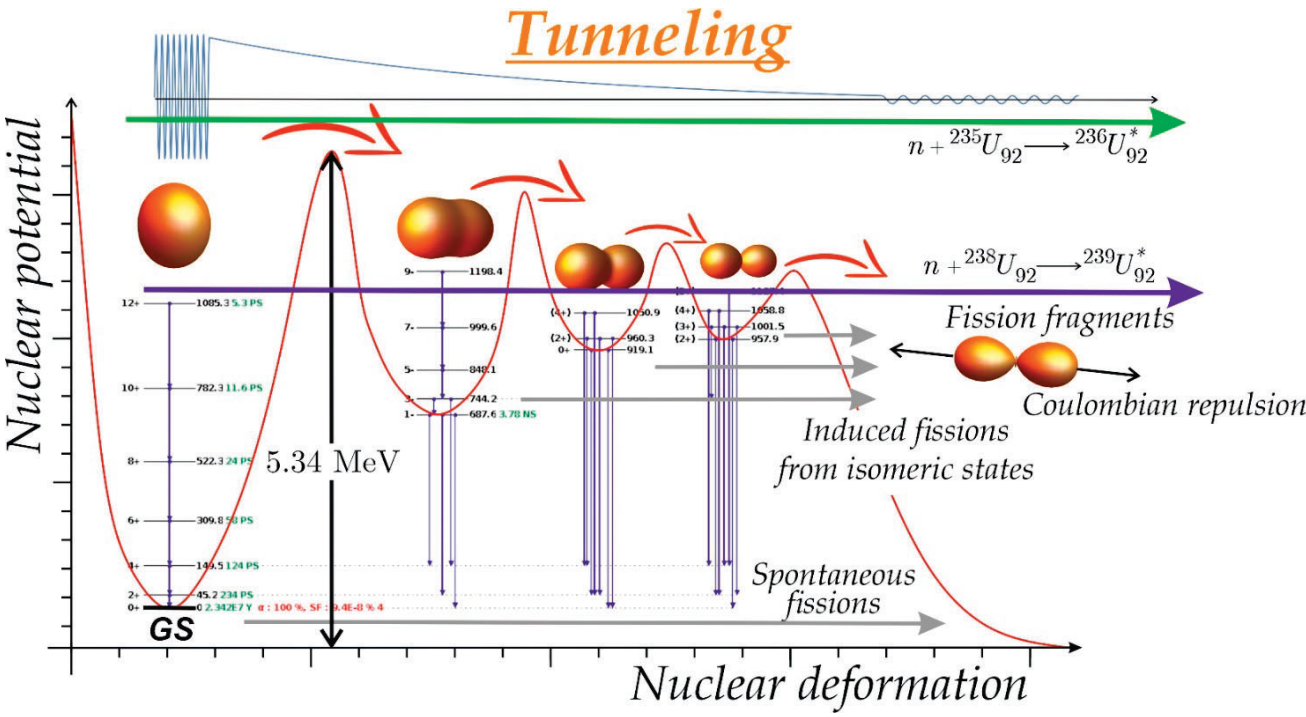

FIGURE 1.8: Thermal fission processes for ^{235}U and ^{238}U. Image taken from Alessandro Saltarelli *"Lectures on Nuclear Physics"*.

$$E_{239_U} = |E_{Even-Even}(92,239)| - |E_{odd}(92,238)| = 4.8MeV$$

This difference in excitation energies has an important implication for the fission barrier height, which is lower for ^{236}U* (with A $\sim$ 240 and Z $\sim$ 92) due to its higher excitation energy, at 5.34 MeV. However, for ^{239}U, the fission barrier height is higher, despite its lower excitation energy, due to its higher mass and greater number of protons and neutrons. This fact is also described in Fig. 1.8, which shows the nuclear potential as a function of the nuclear deformation.

Proton-induced fission instead, refers to the fission process that occurs when a high-energy proton is used to bombard a target nucleus, resulting in the splitting of the target nucleus into two or more fragments. The process is similar to neutron-induced fission, but instead of a neutron being absorbed by the nucleus, a proton is used to induce fission.

The fission process induced by protons can produce a wide range of fission products with various masses and charge numbers. However, similar to neutron-induced fission, the most probable fission fragments produced from proton-induced fission of ^{235}U at 50-60 MeV proton energy are ^{141}Ba and ^{92}Kr.

The yield of the fission products from proton-induced fission depends on various factors, such as the target nucleus, the proton energy, and the angle of incidence. Fig. 1.9 shows examples of the fission yields obtained from ^{235}U and ^{238}U, the fission in this case were induced by 50 MeV protons [7].

Proton-induced fission has been used in various applications, including the production of isotopes for medical and industrial purposes. In particular, it is commonly used as a method for producing short-lived isotopes in the context of Isotope Separation On-Line (ISOL) targets. ISOL targets are used to produce radioactive isotopes for a wide range of applications, such as nuclear medicine, radiography, and nuclear physics research. In particular, ISOL targets of uranium will be used in SPES for the production of exotic isotopes at the INFN Laboratori Nazionali di Legnaro. The procedure in question will be described in detail in Chapter 2.

1.4 Beta Decay

Beta decay is a radioactive decay mode that is the most common among isotopes. It involves the transformation of a nucleus into a different nucleus with proton number Z and neutron number N changed by one unit. There are three types of beta decay: beta-minus (β^-) decay, in which the nucleus emits an electron and an antineutrino, resulting in an increase of the proton number Z by one; and beta-plus (β^+) decay, in which the nucleus emits a positron and a neutrino, resulting in a decrease of the proton number Z by one. Finally the third type is electron capture (EC), which is a competitive process to the β^+ and populates the same daughter states as the positron emission. In

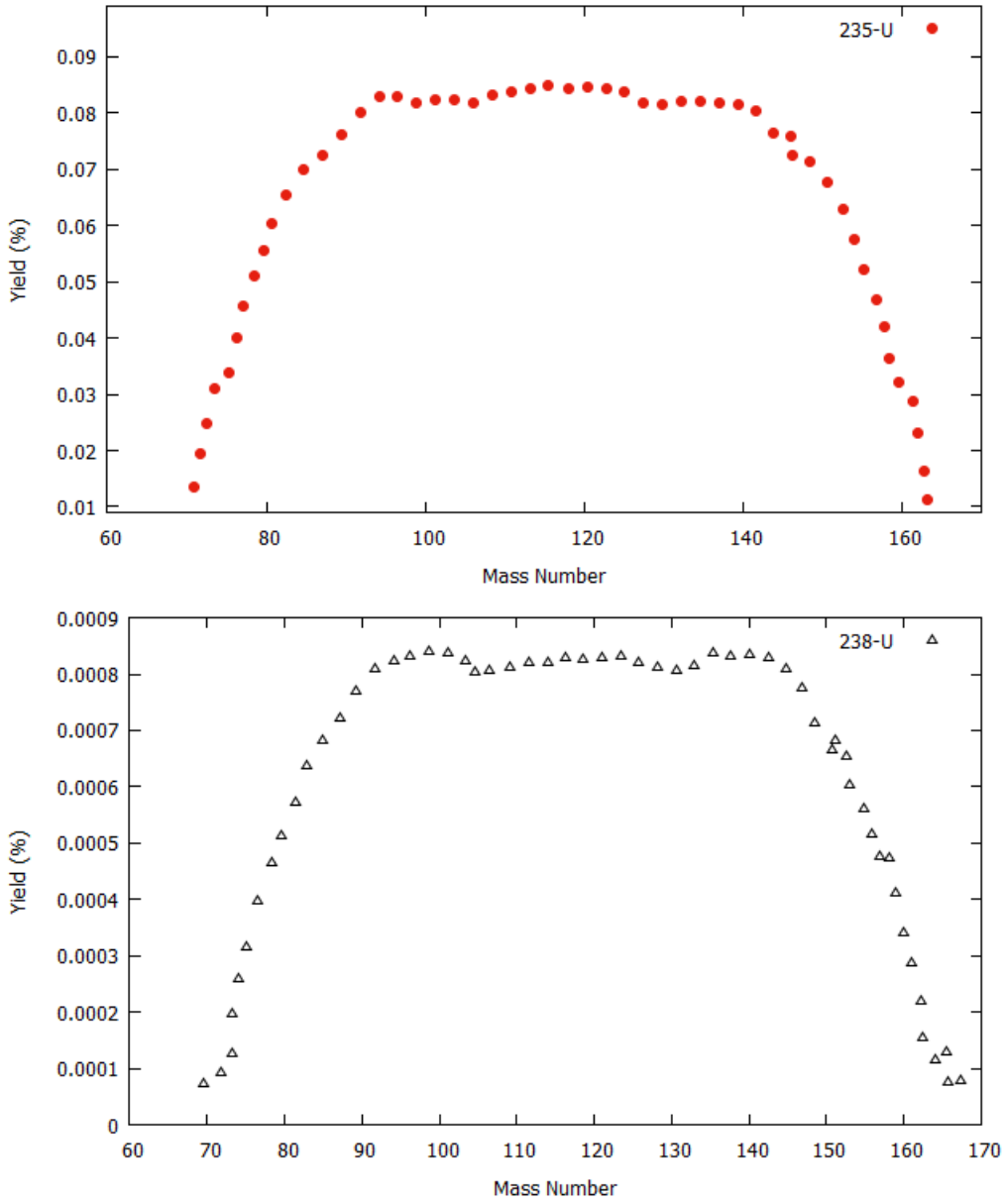

FIGURE 1.9: Example of fission yield induced in ^{235}U and ^{238}U with 50 MeV protons [7].

this process the nucleus absorbs and atomic electron and consequently emits a neutron and a neutrino. These three processes can be described as follows:

$$\begin{cases} \beta^- : & n \longrightarrow p + e^- + \overline{\nu} \\ \beta^+ : & p \longrightarrow n + e^+ + \nu \\ EC : & p + e^- \longrightarrow n + \nu \end{cases}$$

In terms of a general father isotope X and a daughter Y, the β decays processes can be described instead in the following way:

$$\begin{cases} \beta^- : & {}^A_Z X_N \longrightarrow {}^A_{Z+1} Y_{N-1} + e^- + \overline{\nu} \\ \beta^+ : & {}^A_Z X_N \longrightarrow {}^A_{Z-1} Y_{N+1} + e^+ + \nu \\ EC : & {}^A_Z X_N + e^- \longrightarrow {}^A_{Z-1} Y_{N+1} + n + \nu \end{cases}$$

The existence of neutrino has been discovered starting from the observation that the energy distribution of a β particle is continuous and, if it were a two body decay instead, electrons would have specific energies depending on the final excited state in the daughter nucleus. Two examples of beta particle energy distribution are shown in Fig. 1.10, for the case of β^- decay of ^{146}Eu and ^{148}Pm [8] [9]. In fact beta particles are emitted in a range of energies between zero and an upper limit and it was proven that the "missing energy" in the process is taken by the neutrino.

The conservation of charge requires the neutrino to be neutral and, from the conservation of angular momentum, to have spin $\frac{1}{2}$.

The Q value of the decay can be expressed in terms of the neutrino and the electron energies, T_e and $T_{\overline{\nu}}$. As a result we can write:

$$Q = T_{M(^AY)} + T_e + T_{\overline{\nu}} \tag{1.38}$$

however the recoil energy of the nucleus ($T_{M(^AY)}$) is of the order of few keV and is negligible, hence the Q value of a β decay is:

$$Q = T_e + T_{\overline{\nu}} \tag{1.39}$$

In other words the Q value represents the energy shared between the antineutrino and the electron. The same argument can be repeated for the positron and neutrino in the case of the β^+ decay.

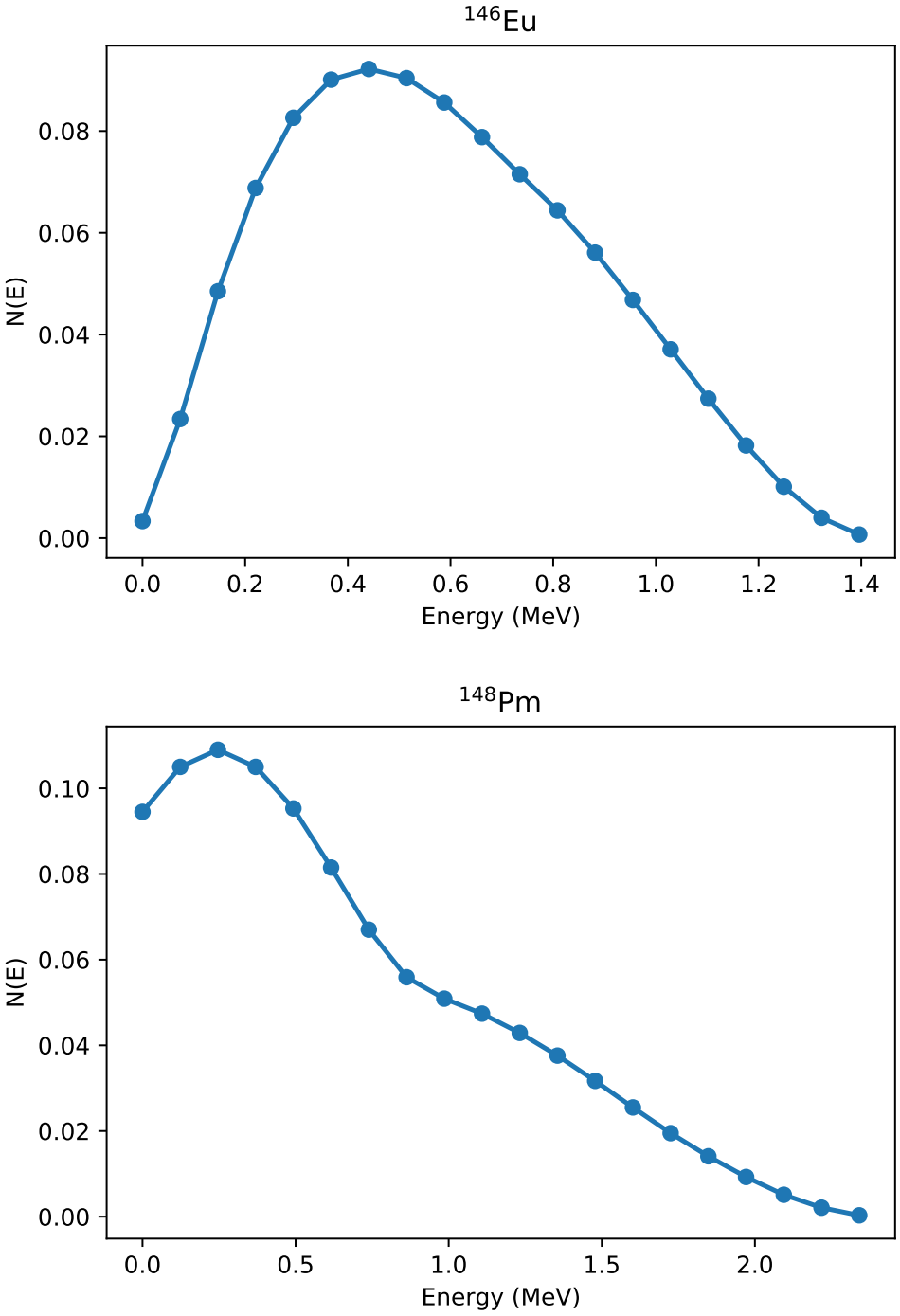

FIGURE 1.10: Electrons energy distribution in the beta decay of ^{146}Eu [8] and ^{148}Pm [9].

In considering the rate of beta decay, several factors must be taken into account. First, for a given amount of energy released in the decay, there is a density of final states available for both the electron (or positron) and the neutrino (or antineutrino) emitted. The electron or positron will also encounter the Coulomb barrier produced by the protons in the nucleus. In addition, the product of the electron or positron wavefunction and the neutrino or antineutrino wavefunction has parity (-1)^l, where l is the orbital angular momentum. The rate of β-decay can be described through the Fermi theory and Gamow-Teller modification. Beginning with the Fermi golden rule for the rate of decay (λ):

$$\lambda = \frac{2\pi}{\hbar} \times | < \psi_f | V | \psi_i > |^2 \times \rho(E_f) \tag{1.40}$$

where $\rho(E_f)$ represents the density of final states for the neutrino and antineutrino. The matrix element can be quantified by the matrix element between the initial state of the parent nucleus and the state of the daughter nucleus, where, ψ_f and ψ_i represent the final and initial nuclear states, respectively, while V is the operator responsible for the β decay. The Fermi golden rule can be applied to calculate the electron yield, which is the number of electrons emitted per unit time. The electron yield (Y) can be obtained by integrating the transition rate over all electron energies:

$$Y = \int \lambda(E) dE$$

To calculate the electron yield, we need to express the transition rate in terms of the electron energy (E) and take into account the Coulomb force experienced by the emitted electron or positron. In fact, the Coulomb interaction between the emitted beta particle and the positively charged daughter nucleus generates a distortion in the beta spectrum, which is dependent on the atomic number of the daughter nucleus and the momentum of the

emitted electron or positron. For electrons, small momentum emissions are favored, while for positrons, large momentum emissions are favored. To account for this effect mathematically, a corrective factor called the Coulomb correction factor, denoted by F(Z,E), can be introduced. The expression for the Coulomb correction factor was derived by fitting it to numerous experimental data and is:

$$F(Z_D, \epsilon) = \frac{(1 - e^{\mp 2\pi Z_D \alpha}) \cdot \frac{\epsilon}{\sqrt{\epsilon^2 - 1}}}{(1 - e^{\mp 2\pi Z_D \alpha \cdot \frac{\epsilon}{\sqrt{\epsilon^2 - 1}}})} \tag{1.41}$$

where the minus and plus signs in the exponential are for β^- and β^+ respectively, while α is a fine structure constant and is $\alpha \sim 1/137$. Taking into account the Coulomb correction, the corrected transition rate λ_C is given by:

$$\lambda_C(E) = \int \lambda(E) F(Z_D, \epsilon) \tag{1.42}$$

The square of the matrix element in eq. 1.40 is the transition probability B:

$$B = |M_{fi}|^2 = | < \psi_f^* | V | \psi_i > |^2 \tag{1.43}$$

The matrix element M_{fi} is proportional to the inverse of a quantity known as the ft-value, given by $ft = t / |f(Z, E_0)|^2$, where t is the partial half-life for the transition and $f(Z, E_0)$ is the Fermi integral that takes into account the effects of the neutrino and electron wavefunctions. That is,

$$M_{fi} \propto \frac{1}{ft}. \tag{1.44}$$

The logarithm of the ft-value serves as a useful metric for comparing the probability of β-decay between different isotopes. The logarithm is utilized

due to the wide range of half-life values associated with this type of transition, and the corresponding variability in ft-value. Specifically, $\log(ft)$ is used to categorize different types of transitions, with $\log(ft) < 6$ corresponding to *allowed* transitions, and transitions with higher $\log(ft)$ values referred to as $forbidden$. However, such a classification is imprecise as the latter type of transition is not strictly forbidden, but rather slower than the *allowed* transitions. Fig. 1.11 shows the number of allowed and forbidden transitions as a function of the logharitm of the ft-value, it is woth noting that the $\log(ft)$ value may be much larger then 6 even for allowed transitions. Additionally the superallowed term in the figure refers to Fermi decays, that will be described later.

Fermi assumed that the interaction would take place at the center of the nucleus, meaning that the coupled neutrino and electron would carry zero angular momentum or $L = 0$. Considering the total change in momentum:

$$I_i = I_f + L + S, \tag{1.45}$$

where I_i is the spin of the parent isotope, I_f is the spin of the daughter isotope, L represents the angular momentum change due to the emission of the electron and antineutrino, and S is the sum of the electron and neutrino spins. In the allowed approximation, as the angular momentum change is zero, the only change in nuclear angular momentum must come from spin (S). S can have a value of 0 or 1, since both the neutrino and electron have a spin value of $s = \pm\frac{1}{2}$, and hence $\Delta I = I_i - I_f = 0, 1, -1$. Transitions with parallel spins between the neutrino and electron, and changes of 0 or ± 1 between the parent and daughter isotopes, are classified as *allowed* transitions. If the electron and neutrino spins are antiparallel and hence $S = 0$, the transition is referred to as a Fermi transition, while if the spins are parallel ($S = 1$), the transition is a Gamow-Teller transition (GT). Fig 1.12 provides a quick

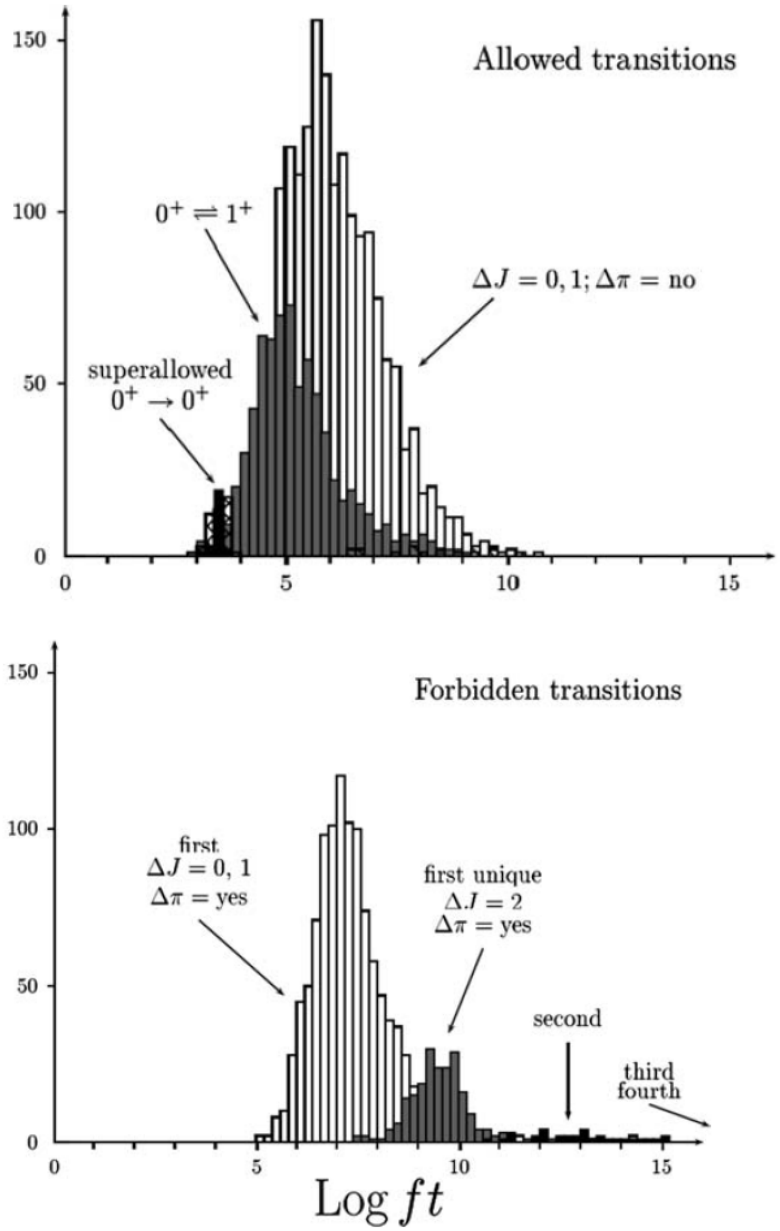

FIGURE 1.11: Number of allowed transitions (up) and forbidden transitions (low) in terms of the logarithm of the ft-value [4].

scheme of the Fermi and Gamow-Teller transitions.

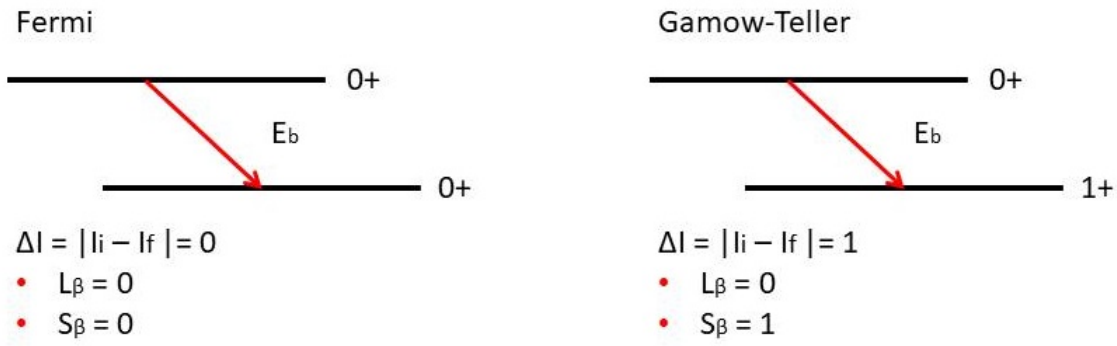

FIGURE 1.12: Schemes of the Fermi (left) and Gamow-Teller (right) transitions.

Forbidden transitions, which occur with $L \neq 0$, are less probable than their *allowed* counterparts, and are classified based on the change in angular momentum. Transitions with $L = 1$ are referred to as $first - forbidden$ transitions, with $L = 2$ classified as $second - forbidden$, and are even less probable than the $first - forbidden$ transitions, and so on. In general, by including the parity of the transition, the following selection rules can be used to classify a transition:

$$\begin{cases} J_f = J_i & \text{and } \pi_i \pi_f = +1 \text{ for Fermi transitions} \\ J_f - J_i = 0, 1 & (0 \longrightarrow 0),\ \pi_i \pi_f = +1 \text{ for GT transitions} \\ L \neq 0 & \text{and } \pi_i \pi_f = -1 \text{ for forbidden transitions} \end{cases}$$

The allowed and forbidden transitions are classified in Tab. 1.3, depending on the spin and parity change.

Type of transition	Order of forbiddeness	ΔI	$\pi_i\pi_f$
Allowed		0,+1	+1
Forbidden unique	1	∓ 2	-1
	2	∓ 3	+1
	3	∓ 4	-1
	4	∓ 5	+1
Forbidden	1	$0, \mp 1$	-1
	2	∓ 2	+1
	3	∓ 3	-1
	4	∓ 4	+1

TABLE 1.3: Table categorizing the allowed and forbidden transitions for ΔI and parity change.

1.5 Daughter Nuclei Excited States

As a result of the β - decay the daughter nucleus can be in an excited state, the daughter will then continue through the decay with three types of de-excitation processes:

- γ-ray de-excitation
- internal conversion
- β delayed neutron emission.

1.5.1 γ-ray de-excitation

The de-excitation process by γ-ray emission is a prevalent phenomenon that occurs more rapidly than β-decay. It involves the decay of a daughter nucleus from its excited state by releasing γ-rays, with excited state lifetimes being between few picoseconds to nanoseconds. The energy, parities, spin, and half-life of the excited states can be inferred by analyzing the properties of the emitted γ-rays, such as their energies, multipolarities, and intensities. These properties depend heavily on the wave functions of the states involved and the transition operator for electromagnetic transitions, both of which are

contained within the reduced transition probability. The transition rate is calculated by expanding the electromagnetic radiation field in multipoles, with the lowest order term being the most probable transition. In other words, the most likely transition is the one with the lowest multipolarity permitted by the selection rules dictated by the conservation of angular momentum and parity. Transitions in γ de-excitation processes can be electric or magnetic. In general, electric multipole transitions involve the emission or absorption of photons that arise from the interaction of the electric charge distribution within the system. Magnetic multipole transitions, on the other hand, involve the emission or absorption of photons that arise from the interaction of the magnetic moment distribution within the system. The most common multipolarities for gamma de-excitation are electric dipole (E1), electric quadrupole (E2), and magnetic dipole (M1). Higher multipole transitions, such as electric octupole (E3) and magnetic quadrupole (M2), are less common but can still occur. The selection rules for gamma de-excitation depend on the multipolarity and parity of the transition. The angular momentum (L) of a transition is determined by the expression $|J_f - J_i| \leq L \leq |J_f + J_i|$, where J_f and J_i are the final and initial angular momentum. The nature of the transition is then characterized as $^{(-1)}$L for electric transitions and $^{(-1)}$(L+1) for magnetic transitions. Overall the selection rules are summirized in Tab. 1.4 considering also the parity of the transition.

$\Delta J = \lvert J_f - J_i \rvert$	0^*	1	2	3
$\pi_i \pi_f$ = -1	E1	E1	M2	E3
$\pi_i \pi_f$ = +1	M1	M1	E2	M3

TABLE 1.4: Hierarchy classification of allowed transitions.

1.5.2 Internal Conversion

In this scenario, the energy associated with the nuclear de-excitation is transferred to a bound electron, resulting in its ejection. The energy of the ejected

electron corresponds to the difference between the transition energy and the electron binding energy, E_e, as well as the recoil energy. The ejected electron can originate from any atomic shell, such as K, L, M, etc. The emission of internal conversion electrons represents a competitive process with γ emission during nuclear de-excitation, as both can occur within the same nucleus. The relative strengths of these two processes are characterized by the internal conversion coefficient, α, which represents the ratio between the emitted γ and the internal conversion electron. The same concept can be extended to single atomic shells through the introduction of partial internal conversion coefficients, denoted by α_K, α_L, α_M, and so on. The sum of all partial internal conversion coefficients yields the internal conversion coefficient. The values of the internal conversion coefficients are highly dependent on the transition energy and multipolarity. The probability of a nuclear transition between two states is the sum of the probabilities of γ emission and internal conversion electron emission, as these are competing processes.

The conversion coefficient is related to the atomic number Z of the material in which the gamma ray interacts. As Z increases, the conversion coefficient also increases, which means that the probability of electron ejection increases. In Fig. 1.13 is shown the logarithm conversion coefficient α for different values of Z in the case of electric (left) and magnetic (right) transitions [10].

1.5.3 β-Delayed Neutron Emission

The β-decay of a father nucleus can lead to the population of excited states of the daughter nucleus at energies higher than the energy required to remove a nucleon from the nucleus, which can then be emitted. The emission of β-delayed particles is a process that is particularly enhanced in nuclei with a large number of protons or neutrons, as the separation energy is inversely

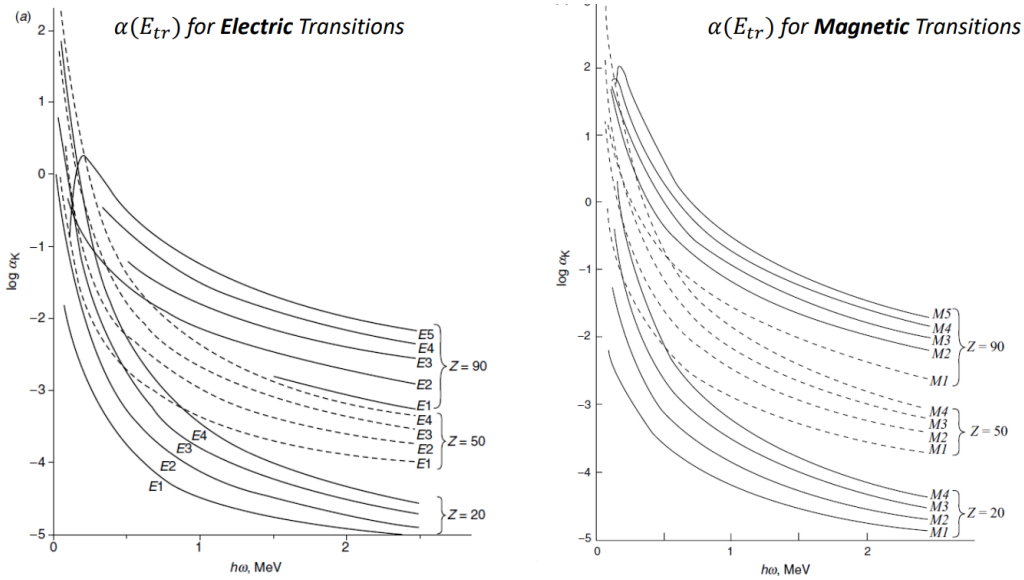

FIGURE 1.13: Logarithm conversion coefficient α for different values of Z in the case of electric (left) and magnetic (right) transitions. This figure can be found in ref. [10]

proportional to the number of nucleons. The limit for proton emission is much closer to the stability line than that for neutron emission due to the Coulomb interaction. In the case of studying β^- decays with delayed neutron emission, an important aspect is the probability P_{x_n} of emitting x neutrons, which represents the probability of populating excited states of the daughter nucleus $^{A-x}(Z{+}1)$ in the β decay of the ^{A}Z father nucleus.

The energy E_n of the emitted neutron can be expressed in terms of the energies E_i^* and E_f^* of the initial and final excited states involved, as well as the separation energy S_n of the neutron, using the following equation:

$$E_n = \frac{A-1}{A}(E_i^* - S_n - E_f^*) \tag{1.46}$$

The selection rules for neutron emission are given by the following equations:

$$J_i = J_f + l_n + \frac{1}{2} \tag{1.47}$$

$$\pi_i = \pi_f \cdot (-1)^{l_n} \tag{1.48}$$

where J_i and J_f are the total angular momenta of the initial and final states, π_i and π_f are the parities of the initial and final states, and l_n is the orbital angular momentum of the emitted neutron. The β neutron delayed process is schematized in Fig. 1.14, the parent nucleus undergoes β decay into the quasi-continuum state of the daughter. At this point the de-excitation process may proceed throguh the usual γ ray cascade to the ground state, or a neutron can be emitted and the nucleus transits to a new nuclear species. The γ cascade from the quasi continuum state can cause something called the Pandemonium effect.

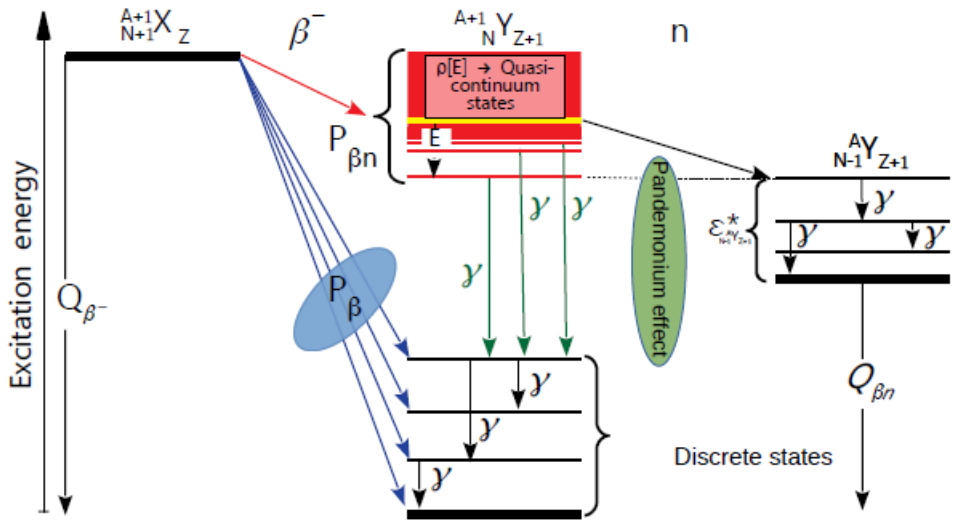

FIGURE 1.14: Scheme of a β-n decay. The parent nucleus undergoes β decay into the quasi-continuum state of the daughter. At this point the de-excitation process may proceed throguh the usual γ ray cascade to the ground state, or a neutron can be emitted and the nucleus transits to a new nuclear species.

The pandemonium effect, firstly introduced by Hardy in 1977 [11], refers to the problem of reconstructing a complex level scheme from a beta decay process. When a nucleus decays with a high Q-value, it will feed a high

number and a high density of the daughter excited states, which in turns cause a considerable gamma cascade. A energy level scheme is reconstructed from gamma-decay measurements either in single or in coincidence mode, however this method heavily relies on the experimental set up detection efficiency. For complex de-excitation processes, many gamma rays may not be detected, leading to an incorrect decay pattern and an incomplete level scheme. The excited levels of the daughter nucleus can be fed in two different ways, either by direct β decay, or by γ de-excitation. The total intensity of the gamma rays emitted by a particular energy level should be the sum of these two contriubution:

$$I_T = I_\beta + \sum_i I_i$$

where I_T is the total γ intensity from the energy level in question, I_β is the contribution coming from β feeding and the I_is come from the *gamma* de-excitation. It should be noted that in this case the effects from internal conversion process are not considered. The problem arises since the β feeding can not be measured directly and so it has to be deduced from the previous equation:

$$I_\beta = I_T - \sum_i I_i$$

When the β reaction Q-value is particularly high, the decay process feeds many levels and this in turns can cause the γ the transitions difficult to detect with low intensities. This effect is especially emphasized when high energy levels with a high density of states (quasi continuum) are involved. In such cases, due to relatively poor efficiency of detectors, respect to the total number of γ rays involved, less I_i are detected and it could lead to the erroneous assumption that $I_\beta \sim I_T$. Fig 1.15 shows and example of a β decay with probability to decay in three excited energy levels of the daughter nucleus. If I_1

and I_2 cannot be detected efficiently, due to the poor intensity of the transitions or the energy of the γ emitted, it is possible to mistakenly consider the β decay as feeding only level 3 of the daughter nuclide.

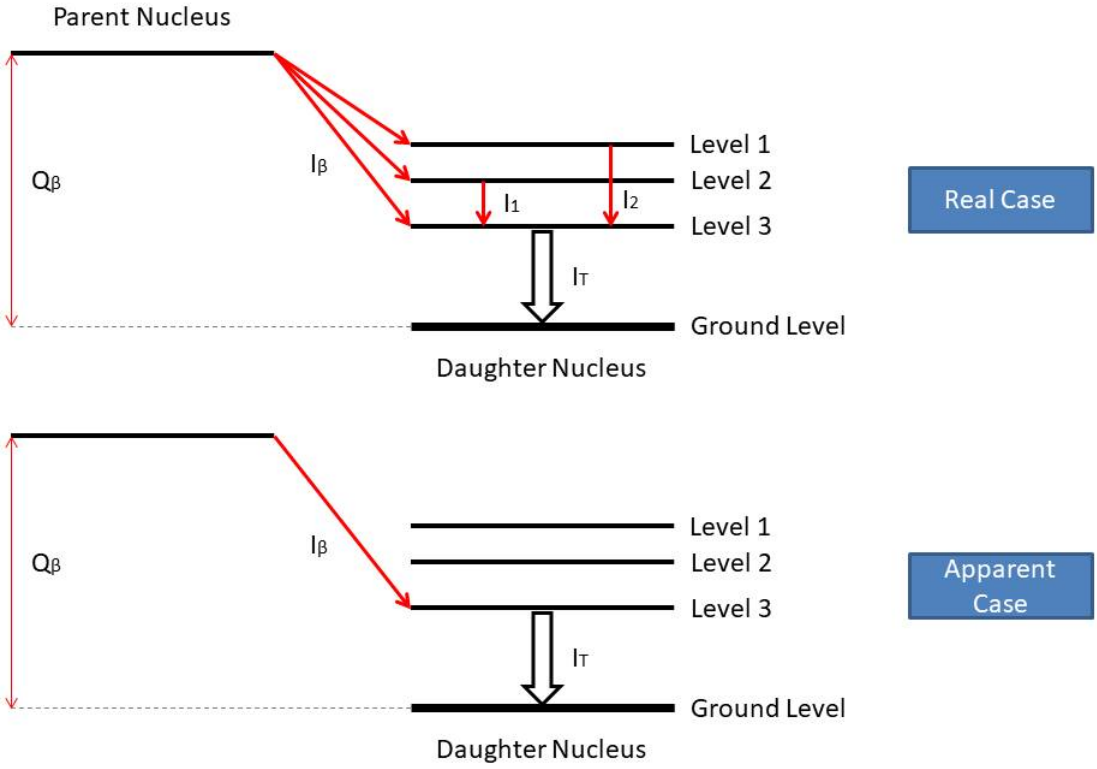

FIGURE 1.15: Scheme showing a simple example of the pandemonium effect. The β decay feeds three energy levels of the daughter nuclide, which then decay to the ground state (upper figure). If poor intensities of the transitions or the energy of the γ emitted prevents us to correctly estimate I_1 and I_2, it is possible to mistakenly assume that the β decay only feeds level 3 of the daughter nuclide.

Chapter 2

SPES Facility for Exotic Isotope Beams

2.1 Introduction

The exploration of the isotope chart is essential to deepen our understanding of nuclear structure and nucleosynthesis mechanism. For this purpose the construction of the SPES facility at the "Laboratori Nazionali di Legnaro" intends to provide us with fundamental information on exotic, neutron rich, nuclei for forefront research on nuclear physics. The SPES acronym stands for "Selective Production of Exotic Species" and the project goal is to provide high intensity and high quality neutron rich beams, not only for research on structure and dynamic of nuclei, but also for interdisciplinary fields like nuclear medicine, biology or material studies.

Recent progresses in particle accelerator science have allowed the use of beams of unstable isotopes, which enables us to access the uncharted regions of the neutron rich isotopes on the nuclei map. Depending on the number protons (Z) and the number of neutron (N), an isotope can be classified as stable, bound but unstable and unbound. The difference between a bound and an unbound nucleus is determined by the binding energy, or the energy necessary to extract a nucleon. When the binding energy becomes negative,

nucleons will not be bound together anymore and, as a result, an isotope will start to decay by particle emission of either a proton or a neutron toward a stable state. Following this definition, it is possible to delineate drip lines along the nuclei chart by mapping the binding energy zero crossing position for each isotope. There are two known drip lines, the proton drip line and the neutron drip line. The proton drip line traces the border of the region after which the addition of a proton makes an isotope unbound and, therefore, starting to decay by proton emission. For light nuclei the proton drip line approximately rest in the region of isotopes with the same number of neutrons and protons (N=Z). Similar to the proton drip line, the neutron drip line defines the limit after which unbound nuclei start to decay by neutron emission. Due to the absence of Coulomb repulsion, isotopes with a large abundance of neutrons are allowed to exist in the bound state and, as a result, the neutron drip line lays much further away from stability respect then its proton counterpart. The position of the neutron drip line is known only for light nuclei, with atomic mass number $Z \sim 30$. One of SPES goals is to further draw the neutron drip line also for heavier nuclei. The interest on nuclei with a great excess of neutron is not only limited on the neutron drip line drawing, but also on other phenomenons such as the effective nucleons interaction dependence on the density, for nuclei with exotic N/Z ratios. In general, as we approach the neutron drip line, nuclear properties are dependent on how the nuclear shell is affected by an excess of neutron, so the change in density by increasing the N/Z ratio is expected to lead to new symmetries. In the case of light nuclei researches have identified the formation of an halo-like structure, while heavier nuclei are predicted to develop a neutron skin. These structural changes have consequences on the ground state properties as well as single particle and collective excitation. The formation of a neutron skin is also expected to lead to new modes of collective motion, in particular an oscillation of the neutron skin against the nucleus core, in a similar fashion

to the soft dipole mode observed in light neutron halo nuclei.

The study of neutron rich isotope will also be interesting for processes like tunneling effects in sub-barrier fusion reactions, when Q-values are very positives. This kind of information, along with basic nuclear properties like lifetimes, neutron capture probabilities and nuclear masses, have great impact on the astrophysical models. For example in understanding the behaviour of compact astrophysical systems like neutron stars, where exotic isotopes forming a Coulomb lattice are submerged in a sea of neutrons. Fig. 2.1 shows isotope abundances as a function of the mass for neutron stars marger, but also for neutrino wind [12].

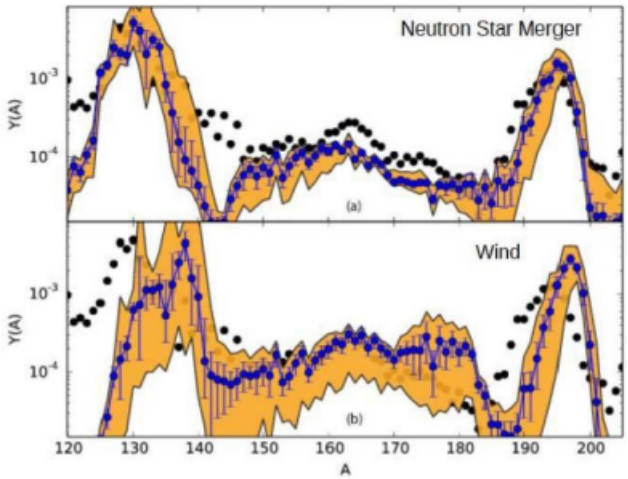

FIGURE 2.1: Isotopes abundances for for neutron stars marger and neutrino wind. Picture available in ref. [12]

2.2 SPES Project and Components

The ions for the radioactive beam will be produced through ISOL technique [3], by proton induced fission reactions directly on a target of uranium carbide (UC_x), and are then accelerated using the ALPI Linear accelerator (LINAC) [**ALPI**]. The protons necessary for the fission reactions are provided by a cyclotron, capable of reaching a maximum beam intensity of 0.75 mA of current [13]. The cyclotron has two exit ports for the protons and has the ability to

accelerate up to two proton beams simultaneously, traveling in opposite directions. One beam will have a current of 200 μA and an energy of 40 MeV, in order to reach the desired 10^{13} fissions per second. The other, with a maximum current of 500 μA and energy 70 MeV, will be used mainly for the production of radiopharmaceuticals through direct proton neutron exchange reaction (p,n) and for the production of neutron in general for material research or the study of new isotopes.

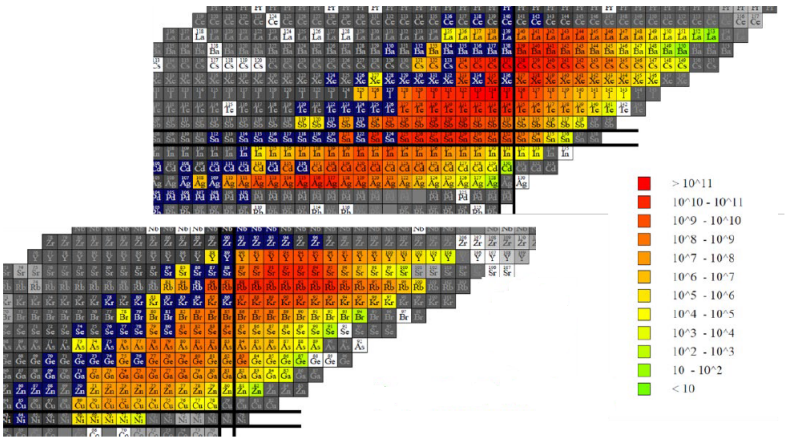

FIGURE 2.2: Isotopes chart of the nuclides produced by inducing fission on a ^{238}U target with protons of 40 MeV. Image available in ref. [14]

SPES operating energy conditions will make it possible to thoroughly investigate neutron rich matter, providing us with basic information on nuclear forces, level density, viscosity, barrier, neutron pairing and collective modes

The SPES project is organized in four main stages: the alpha (α), beta (β), gamma (γ) and delta (δ) stages [14]. Fig. 2.3 shows a scheme of SPES components.

The first stage is SPES-α, the cyclotron employed to accelerate protons to induce fission reaction on the target. As already mentioned, the machine operates in the energy range between 35 and 70 MeV, with a maximum current of 700 μA. The cyclotron belongs to the Azimuth Varying Field (AVF) category, where the main magnet is energized by resistive coils, with two delta

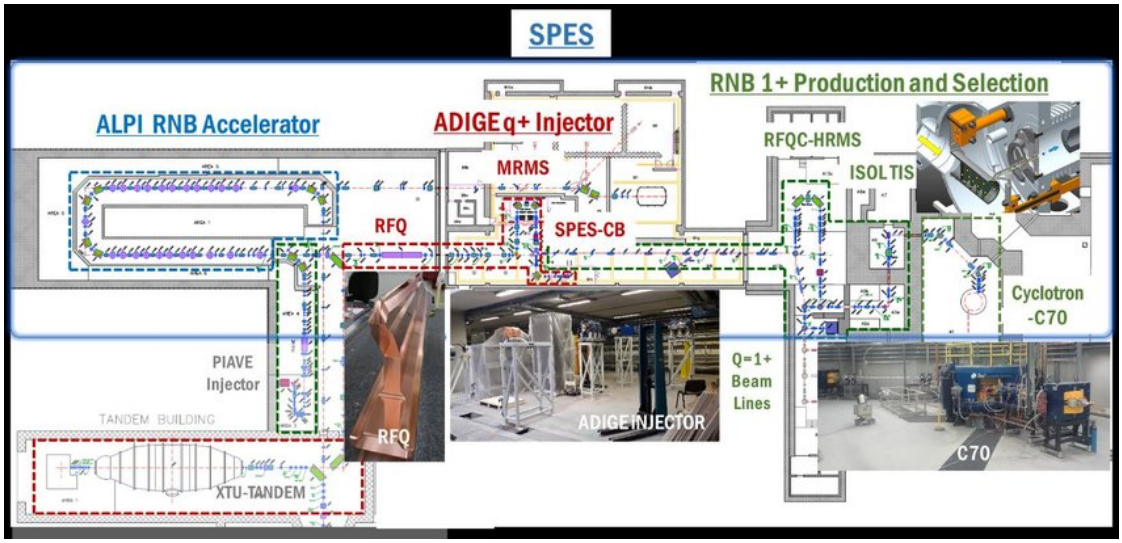

FIGURE 2.3: Scheme of SPES main components. Image available in ref. [14]

shaped electrodes. Each electrode is powered with 55 kW at 56 MHz frequency and can reach a voltage of 70 kV. Ions of H^- are injected axially, with the aid of an electrostatic inflector, from a multi ion cusp source. Protons are then stripped from the H^- nucleus thanks to a thin graphite foil.

FIGURE 2.4: SPES α cyclotrone. Image available in ref. [14]

SPES-β is for the production and acceleration of the ion beam, using the ions produced with SPES-α, for nuclear physics studies. The station main challenges are the construction of the target ion source (TIS) and the ion beam

high resolution mass purification [15] [16]. The TIS is a thick UC_x target, capable of withstanding 200 μA proton beam current and 40 MeV energy. Since the beam power is released directly on the target, the UC_x is actually divided in several slices to optimize heat dissipation and ions extraction efficiencies. The proton beam is coupled to the TIS with a front end, integrated with the target itself, through a proton entrance channel. The resulting ion beam is expected to emerge from the front end-TIS system at 90° respect to the impinging protons. In total three targets have been designed to cover a wide variety of applications: a surface ion source with high selectivity and high efficiency for ions like Caesium and Barium, a plasma ion source required for elements with high ionization energies and finally a highly selective laser ion source based on resonant photo-multiplication. The RIB extraction procedure is then followed by a low mass resolution spectrometer (LMRS). The LMRS is composed by a first selection Wien filter with a resolution of $\Delta M/M \sim 1/150$ and a magnetic dipole for a final mass resolution of $\Delta M/M \sim 1/200$. The ions that survives this stage are slightly ionized 1^+ and accelerated with a 40 kV potential through the high potential platform of the front end, in such a way to transport the beam to the next station with electrostatic elements. At this point the beam is sent either to a tape station (further details on the tape station will be given in sec 2.4), an experimental area for non re-accelerated beams or to the post acceleration process. The diagnostic tape purpose is to develop and optimize the TIS, as well as provide a first characterization of the ion beam for the users. It is worth noting that, at this point, all the lines are designed to allow the purification of the beam through a high resolution mass separator (HRMS) with a nominal resolution of $\Delta M/M \sim 1/2000$ [17] . This kind of resolution is possible only for beams with transverse emittance of few π·mm· mrad. For this purpose a beam cooler is installed as an injector to the HRMS. Finally post accelerated beam are directed towards the the ADIGE complex [18] [19] In ADIGE the RIB undergoes a charge breeder for

charge multiplication, a medium mass separator and a RFQ injector, before being sent to ALPI accelerator, more details on the post acceleration process will be given in sec. 2.4.

SPES-γ is dedicated for the production of radionuclides, mainly for medical applications, in the LARAMED and ISOLPHARM projects [20] [21] [22] [23]. The LARAMED initiative is dedicated to the production of difficult to obtain isotopes for radiopharmaceuticals. In particular the project focus is to optimize the production route of theranostic isotopes like ^{67}Cu, ^{47}Sc and ^{52}Mn. This isotopes are of particular interest because of their gamma and beta emission, in an energy range suitable both for diagnostic (through imaging) and therapeutic purposes. ISOLPHARM target is to take advantage of the ISOL technique to acquire radioisotopes after on-line separation. This method should allow to collect samples with a high and pure specific activity.

Finally, SPES-δ focus is the production of secondary neutron beams for application in biology, material science and reactor physics. There will be two irradiation ports: one with a standard Be target and moderator to reproduce neutrons with an energy profile similar to the ones produced in reactors. The other will use a rotating mixed Pb-Be target with variable thickness. This technique allows to obtain neutron fluxes in the desired energy range, as well as obtaining quasi mono energetic neutrons. This two techniques will be used in the two facilities: NEPIR and FARETRA [24] [25] [26].

2.2.1 ISOL Front-end

The target material is the core of facilities that accelerate RIBs. A target needs specific characteristics to efficiently work as an ISOL target. The main mechanical properties needed are:

- high cross section for the fission reaction

- heat resistance in order to work in high temperature condition without structural degradation
- good heat conductivity and emissivity to dissipate the proton beam power.

Another important aspects to keep into consideration in the choice of on ISOL target material is the isotopes release efficiency. The release process is divided in two phases:

- diffusion: ability of the generated isotopes to reach the target material surface. A process governed by the Fisk law $J = -D \cdot (d\phi/dx)$ where:
  - J is the diffusion flux and is the amount of substance that passes through a certain area in a period of time ($[1/m^2 s]$)
  - D is the diffusion coefficient ($[m^2/s]$)
  - ϕ is the concentration of substance ($[1/m^3]$)
- effusion: isotopes capacity to reach the ion source either through the material pores or the free space between the disks in high vacuum.

The SPES ISOL target, as already mentioned, is composed by seven UC_x disks, along with another three coaxial graphite disks. All the disks measure 40 mm in diameter and 1 mm in thickness [3] [27].

The target is designed to fully stop the primary proton beam incoming from the cyclotron (SPES α). It is contained in an high vacuum water cooled aluminum chamber, connected to the cyclotron through a series gate valves. As the beam dissipates its power in the target, several exotic nuclei are generated by fission, with atomic mass between 80 and 160. Fig. 2.5 shows the main elements that will be produced, as well as the ionization mechanism to start the RIB acceleration. Another important aspect to take into consideration is the target response under the high temperature conditions induced by

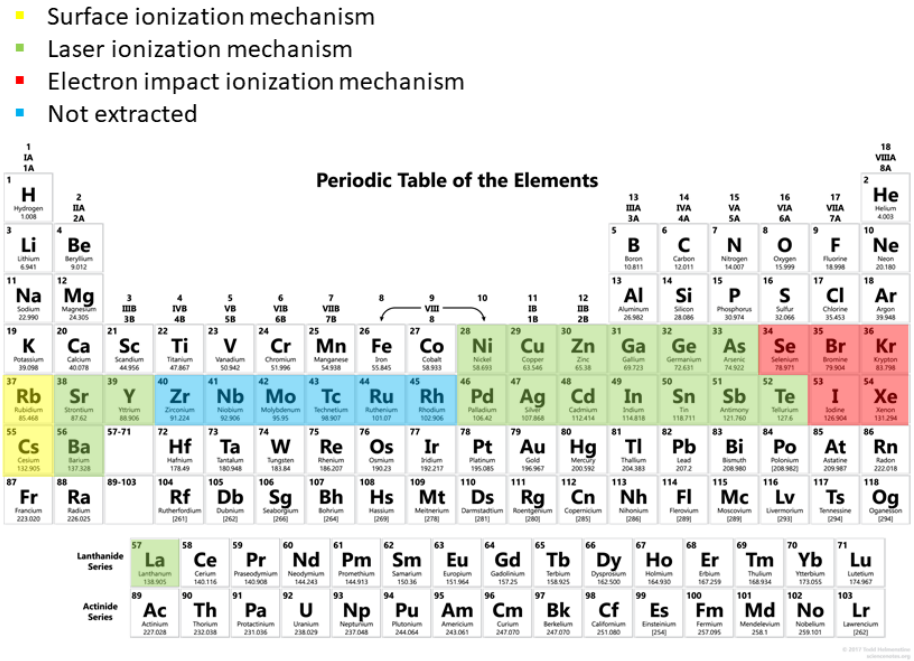

FIGURE 2.5: List of main element produced in the Uranium fission process togheter with an indication of the ionization mechanism that will be used.

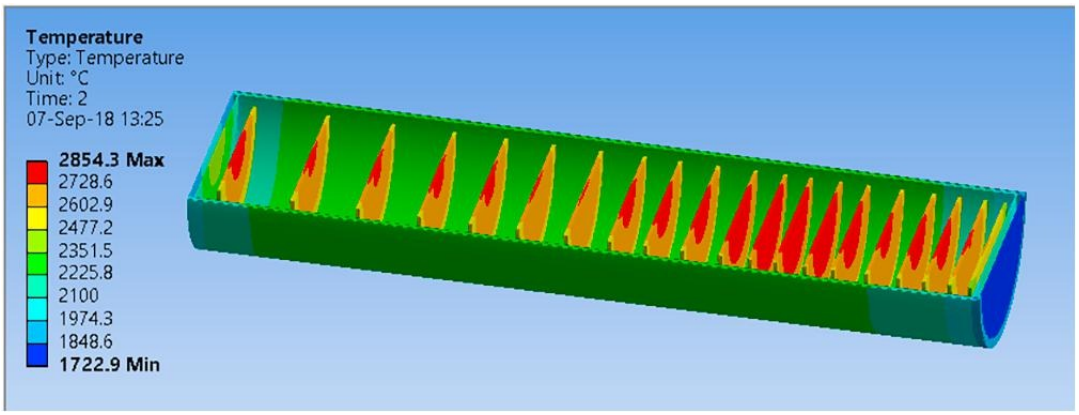

FIGURE 2.6: Result of heat dissipation study on the ISOL target **[MC-isol.]**

the beam. The results of the study on the target thermal behaviour are shown in Fig. 2.6. The study have been carried out through a simulation employing the ANSYS software, while the power distribution on the target was evaluated through Monte Carlo calculations [28]. The simulation seems to indicate

that the UC_x disk temperature is generally around 2000 and 2300 °C. The target chamber is placed in a bunker, in a coupling table. The connection to the beam lines is done through a series of electro-pneumatic actuators, that will open and close the vacuum valves between the beam lines and the chamber. The movement to and from the online zone is done thanks to two independent systems. The device responsible for the vertical movement grabs the target passing through the roof and using an interface tool placed on top of the target vacuum chamber. The horizontal device will enter the bunker through a door and will connect to the rear end of the chamber.

2.2.2 Beam transport

Once the RIB exits the HMRS it is sent to the ALPI linear accelerator. However before the injection the beam pass through a Charge Breeder. This process increases the charge of the ions composing the beam from 1^+ to n^+ and is essential for a successful re acceleration. SPES Charge Breeder is expected to produce ions with ratio of atomic mass over the number of electrons (A/q) of approximately 6, in the case of ions with atomic mass A of 130. The method of operation is based on ion electron cyclotron resonance (ECR). The RIB finally enters ALPI after passing through a second mass spectrometer to clean the beam from eventual impurities caused by the Charge Breeder. The injection in ALPI will be performed by a radio frequency quadrupole (RFQ) that will operate in Cockcroft–Walton with a duty factor of 100% and at a resonant frequency of 80 MHz, which is the same frequency of the lowest energy RFQ of ALPI. The injection beam injection energy value is set to 5.7 keV/u while the extraction energy of the RFQ is set to 727 keV/u to optimize the ALPI beam dynamics. The ALPI acronym stands for *"Acceleratore Lineare Per Ioni"* or ion linear accelerator. ALPI works in superconductivity regime

and is composed of a total of 80 quarter wave resonator (QWR) cavities divided in three sections. The cavities are made of Cu coated with Nb, and are superconductive at a temperature of 9.2 K (-264°C), achieved thanks to a liquid He bath. The superconductive regime of operation allows to generate significantly higher electromagnetic field then a cavity operating in normal conduction regime. This operating condition permits to achieve a good energy efficiency per number of cavity, furthermore it considerably cut the costs of keeping the machine running, even factoring in the necessary power to maintain the cavities cold. The cavities are kept cold thanks to a series of twenty cryostats, each one containing a four cavities. The cryostats keep the cavities in an high vacuum environment to inhibit heat exchange through convection, while heat irradiation is limited thanks to a series of screens kept at various temperatures, in such a way to isolate the cavities from the outside. The ALPI linac finally delivers the beam to experimental targets. Considering the ions production rate in the target and a total transport efficiency of 2% before entering ALPI, it was estimated that expected beam on target count is of the order of 10^8 particles per seconds (pps) for ^{132}Sn and ^{90}Kr and of about 10^6-10^5 pps for ^{134}Sn and ^{95}Kr for example.

2.2.3 NEPIR

The Neutron and Proton Irradiation (NEPIR) facility has been established to conduct Soft Error studies and reliability assessments of cutting-edge electronic devices and systems. The NEPIR facility offers three tools: a continuous intense "white" energy spectrum neutron source, a source of quasi-monoenergetic neutrons, and a direct proton source of variable energy. The first tool, the neutron source, provides a high degree of similarity with the atmospheric spectrum in the energy range of 1 to 50 MeV. Approximately 60% of atmospheric neutrons with energy greater than 1 MeV fall within this

FIGURE 2.7: ALPI accelerator. Picture available online at: "https://www.lnl.infn.it/en/piave-2/"

range. The neutron flux in the energy range of 1 to 50 MeV will be comparable to standard fluxes at existing facilities, and for non-standard applications, the flux can be increased tenfold. The wide and uniform beam allows for the irradiation of large electronic systems, and the beam is delivered to the user area through collimators with varying apertures. The atmospheric neutron spectra is directly produced from the proton beam, and no moderator is required, thus the threshold energy of the neutron spectra is around a few keV. The thermal part of the spectra can be obtained by adding a small amount of moderator, which will thermalize the epithermal neutrons in the bare spectra. The second tool, the quasi-monoenergetic neutron source, is produced by selecting proton energies and corresponding thin lithium targets to produce QMN beams with a controllable peak energy in the 11-65 MeV range. A beryllium target can be used when full Cyclotron current is necessary, though the spectra produced will be "less" quasi-monochromatic. The third tool, the direct proton source, provides protons of variable energy up to 70 MeV. However, the NEPIR facility will not study the high energy neutron-induced effects greater than 200 MeV, such as Single Event Latch-up

and catastrophic Hard Errors like Single Event Burn-outs. These effects can be studied using heavy ion beams, although the correlation with neutron-induced Single Event Effects is not immediate. Heavy ion SEE studies are routinely conducted at Legnaro using the TANDEM and ALPI beams.

2.2.4 FEARETRA

The focus of nuclear energy research is currently directed towards the next generation of fission reactors. It is acknowledged that the ultimate development of Generation IV/ADS-like reactors necessitates cross section data for various actinides and structural material isotopes within the energy range of 100 keV to 10 MeV. For short-lived nuclides, in particular, the conventional experimental technique at facilities such as GELINA, nTOF, and LANSCE, is inadequate, and integral cross section measurements employing intense neutron fluxes with appropriate energy distributions are a viable alternative. To address this requirement, the FARETRA (Fast Reactor Simulator for Transmutation Studies) facility has been proposed. The facility consists of a neutron converter and a moderator. The neutron converter is a high power thick target of Ta or W that can stop the 70 MeV 0.5 mA cyclotron proton beam. The moderator will alter the neutron spectrum to mimic the energy distribution of neutrons within a reactor, with a range from a few keV to a few MeV and a peak in the 200-300 keV region. Within the moderator, several irradiation boxes of 500-1000 cm^3 will be created to accommodate samples for study.

2.3 The β Decay Station

The β decay station (Fig. 2.8) is one of SPES experimental hall and it is dedicated to the study of exotic nuclei β decay using non re-accelerated RIB and is structured in three main parts:

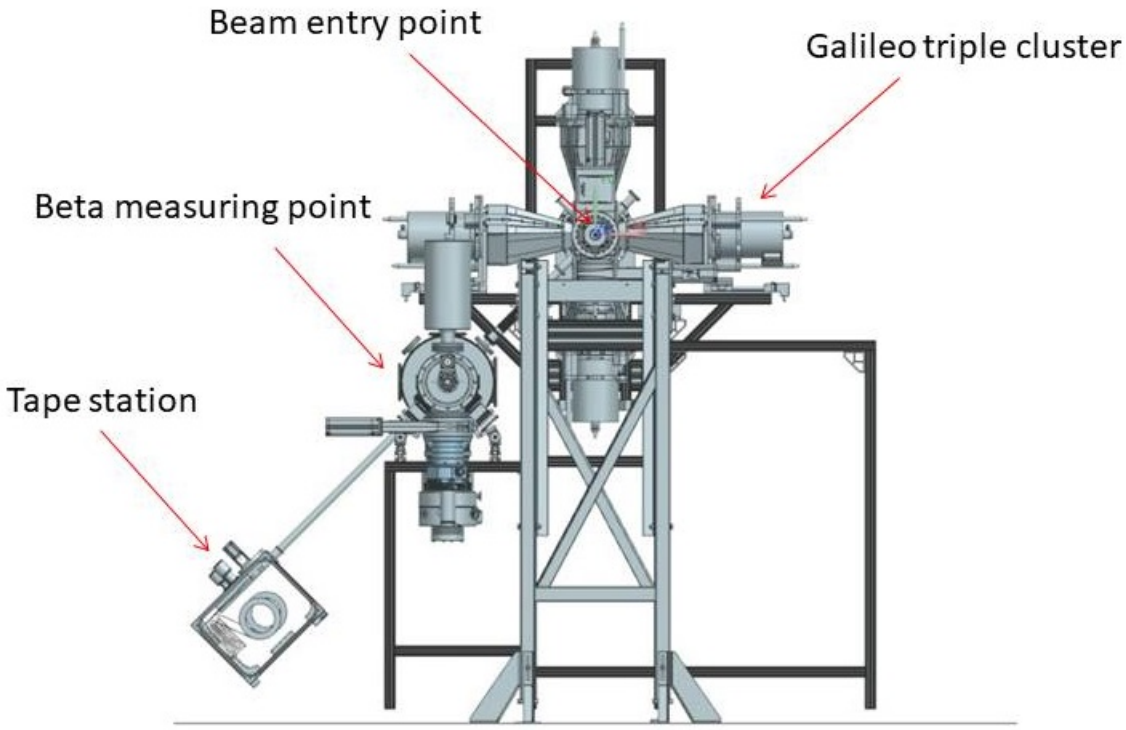

FIGURE 2.8: Frontal view of the entire β decay station.

- γ measuring point and implantation chamber
- conversion electron measuring point
- β decay tape station

The structure containing the implantation chamber and the γ measuring point is aligned with the beam line at approximately 2.3 meters of height. Gamma measurements in this station are performed with a gamma array composed by five HPGe triple clusters (GTC), which consists of three HPGe detectors paired with a cryostat in the same configuration as the Galileo experiment at LNL laboratories. The geometry of the Galileo clusters is design to cover as much of solid angle and to maximize the photopeak efficiency. Under typical in beam counting rates, it was observed an efficiency of 0.20% at 1332 keV [29]. Furthermore the HPGe detectors are surrounded with BGO for anti Compton measurements. The Galileo performances show a peak to Compton ratio of approximately 40% in the case of ^{60}Co. A detailed view

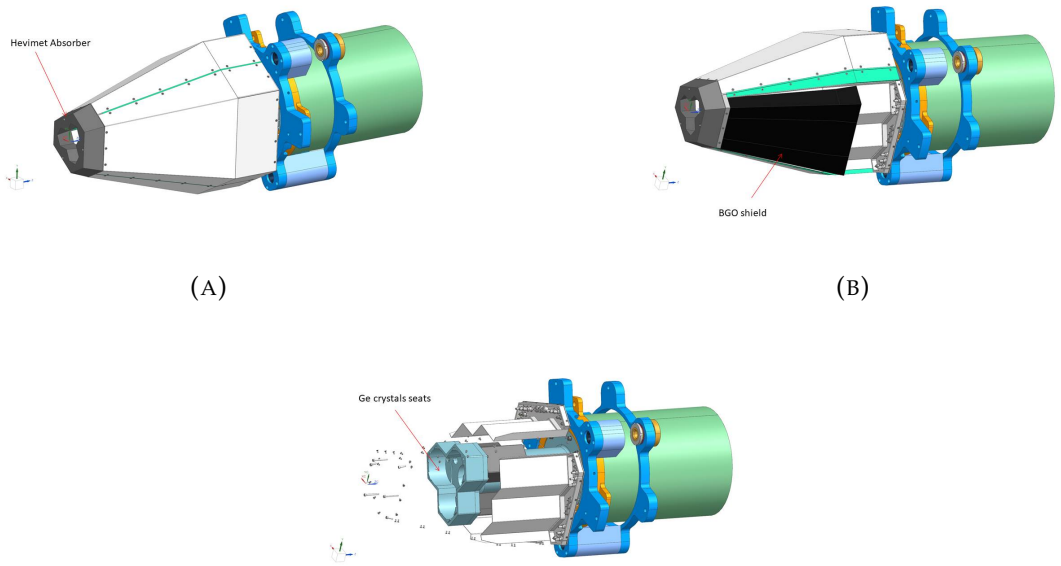

(A) (B)

(C)

FIGURE 2.9: (A) Fully mounted GTC, (B) GTC with BGO shielding showing and (C) open view of the GTC seat.

of a single GTC, with all its components, is presented in Fig. 2.9. Panel 2.9a is a closed view of the system, the Hevimet absorber is 5 cm thick and its function is that of reducing direct γ interactions in the BGO, to further improve the peak to total ratio. It is an alloy composed of tungsten (90%), nickel (7%) and copper (3%). Panel 2.9b and panel 2.9c are instead inside pictures of the system, showing one of the BGO crystals and the mechanical structure without the detectors respectively.

The measuring system also performs beta coincidence measurements, for this purpose the HPGe detectors are also coupled with six 4 mm thick EJ212 plastic scintillators, housed in a 5 mm thick aluminum vacuum chamber placed at the center of the GTC. Beta coincidence measurements are vital to extract information on the isotope decay process, but are also important to identify and reduce the background coming from long lived isotopes implanted in the tape station. Four of the scintillators composing the array are rectangular and are placed on the lateral area of the chamber, while the other

two are octagonal shaped and place at the two ends of the chamber facing the beam. The array design needs to allow the RIB beam to hit the tape on the implantation point, to this purpose one of the two octagonal scintillator has an hole in the center. Finally, the other octagonal scintillator is covered with a 10 μm mylar foil to protect it from accidental hits from the RIB. A view of the chamber and the mounted scintillators is shown in Fig. 2.10.

The measuring point for conversion electrons is 1 m from the implantation point and the measuring is done through the Spes Low energy Internal Conversion Electron Spectrometer (SLICES) [30], placed 1.6 m above the floor. The tape from the tape station crosses a vacuum tube at 45° respect to the vertical line. The set-up is composed by a magnetic lens and a silicon drift ion detector with a large area of 4500 mm^2. More details on slices are given in sec. 2.3.1.

The beta decay tape station collects radioactive isotopes implanted on the tape, after being accelerated by a 40 kV high voltage. The tape is moved after every implantation in order to minimize as much as possible contamination from long lived isotopes. The tape velocity is controlled by a rising and breaking ramp, so it is to be expected that a longer tape traveling distance leads to a higher velocity.

Several RIB are expected to be ready for measurements since day one in SPES and Tab. 2.1 presents a few example of some interesting exotic species.

2.3.1 SLICES

SLICES (see Fig. 2.11) is dedicated to the detection of conversion electrons and its main components are: a boron implanted 4500 mm^2 area Si drift detector and magnetic lenses. The magnetic lens function is to guide electrons toward the detector around a gamma shield, while the great dimension of

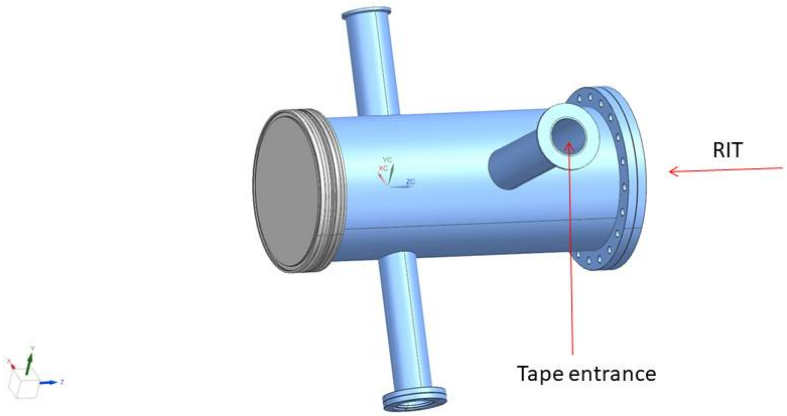

(A) External view of the scintillators chamber .

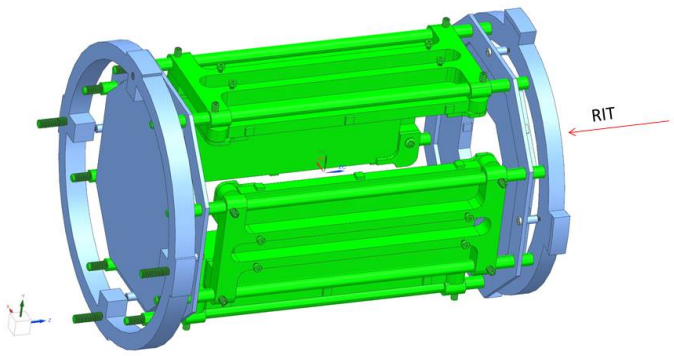

(B)

FIGURE 2.10: View of the scintillators maunted on their support.

Element	A	Z	N	T1/2	Intensity at 40 keV
Cu	69	29	40	$1.71 \cdot 10^{2}$	$9.87 \cdot 10^{6}$
Cu	72	29	43	6.6	$1.39 \cdot 10^{7}$
Zn	73	30	43	23.5	$2.64 \cdot 10^{7}$
Zn	76	30	46	5.7	$1.18 \cdot 10^{7}$
Ga	75	31	44	$1.26 \cdot 10^{2}$	$2.02 \cdot 10^{8}$
Ga	81	31	50	1.22	$1.13 \cdot 10^{7}$
Ge	79	32	47	$1.9 \cdot 10^{2}$	$1.38 \cdot 10^{8}$
Cs	144	55	90	$5.94 \cdot 10^{-1}$	$3.42 \cdot 10^{7}$

TABLE 2.1: Example of neutron abundant isotope beam available at SPES

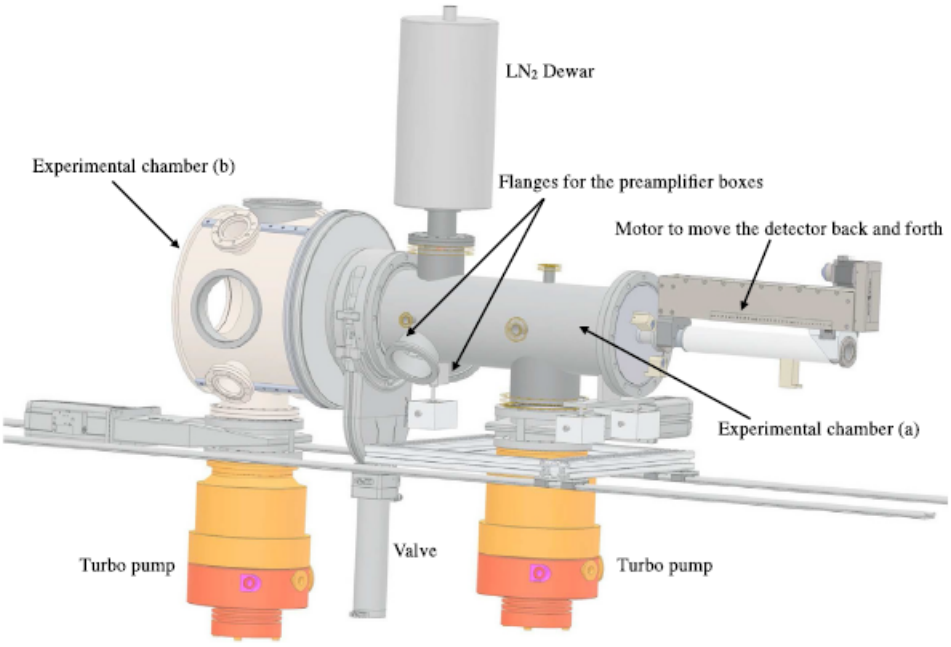

FIGURE 2.11: View of the SLICES system for the detecction of conversion electrons [30].

the Si drift grants a good detection efficiency. The entire system is housed in two independent vacuum chambers with wall thickness of about 3.5 mm, connected by a gate valve. One chamber contains the tape and the magnetic transport lenses, while the other the Si-drift and the cooling and handling system. The handling system moves the detector back and to the measuring point, to allow the closure of the valve connecting the two chambers while also enabling adjustment on the set-up during the typical cold temperature

and vacuum conditions. It also allows to finely tune the detection transmission by tweaking the magnetic lenses detector distance. Finally the detector is cooled with liquid nitrogen through a dewar and a copper braid connected to the system.

2.3.2 Si detector

The Si-drift detector has a thickness of 6.8 mm, enough to stop electrons up to 4 MeV energy, since it is larger then their penetrating distance [31]. The detector large dimensions can lead to capacitance accumulation at the field effect transition (FET) input of the preamplifier, harming the overall resolution. In order to limit this effect the detector is radially segmented for a total of 32-channels. Each channel covers an 11.25° angle and is surrounded by a guard ring, to reduce cross talk between adjacent channels. In typical working condition the detector is cooled to -150 °C, with liquid nitrogen and is then biased to 800 V to achieve full depletion. The detector is then placed near a HV filter to dampen incoming noise from the HV cable. Fig. 2.12 shows an example of a ^{207}Bi energy acquisition with the Si detector, obtained by summing the energy spectra from all the 32 acquisition channels. The resolution obtained was of 5.5 % for the 1064 keV energy ^{207}Bi line .

2.3.3 Magnetic Lenses

The magnetic lens function is to guide electrons toward the detector around the gamma shield, to further improve the detection efficiency. The magnetic lenses need to be designed to allow a good compromise between the maximum and the width of the transmission curve, defined as the ratio between the number of electron detected with magnetic lenses ($N(E)_{MS}$) and

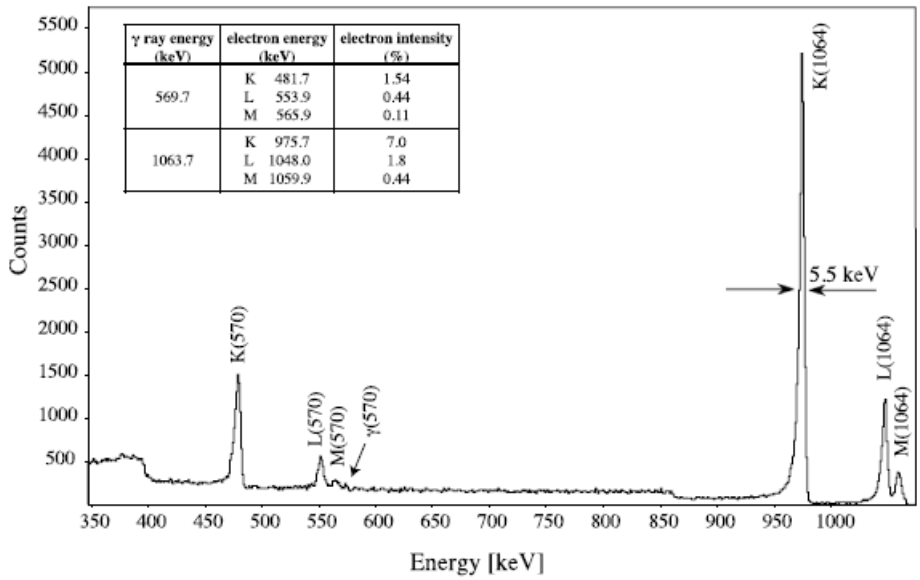

FIGURE 2.12: The spectrum of a ^{207}Bi source was generated by combining the Si(Li) detector spectra from all sectors, using an analog acquisition system with a spectroscopy amplifier shaping time of 6 μsec. The spectrum was acquired without the use of a magnetic transport system, and it displays distinct Compton edges of the γ lines from the 207 Bi source. Furthermore, a minor peak corresponding to the 570 keV γ line (indicated by an arrow) can also be observed. The table reports the energies and intensities of the internal conversion electron transition [30].

the number of electrons of the same energy, without the magnetic lenses ($N(E)_0$):

$$T(E) = \frac{N(E_{MS)}}{N(E)_0} \tag{2.1}$$

The absolute detection efficiency of a sysyem is defined as the ratio between the number of detected electrons and the electrons emitted by the radioactive source. The efficiency however can also be expressed in terms of the transmission curve ($T(E)$) multiplied by the solid angle between the source and the detector (Ω):

$$\epsilon(E) = T(E)\Omega \tag{2.2}$$

The absolute electron detection efficiency of the Si detector when the magnetic lenses are mounted has been tested by measuring a ^{207}Bi radioactive source. The resulting efficiencies as a function of the energy are shown in Fig. 2.13 and 2.14. The blue line in Fig. 2.13 has been obtained through a GEANT4 simulation, while the red points represent the experimental data. Fig. 2.14 are GEANT4 simulated efficiencies for different lens magnet thickness.

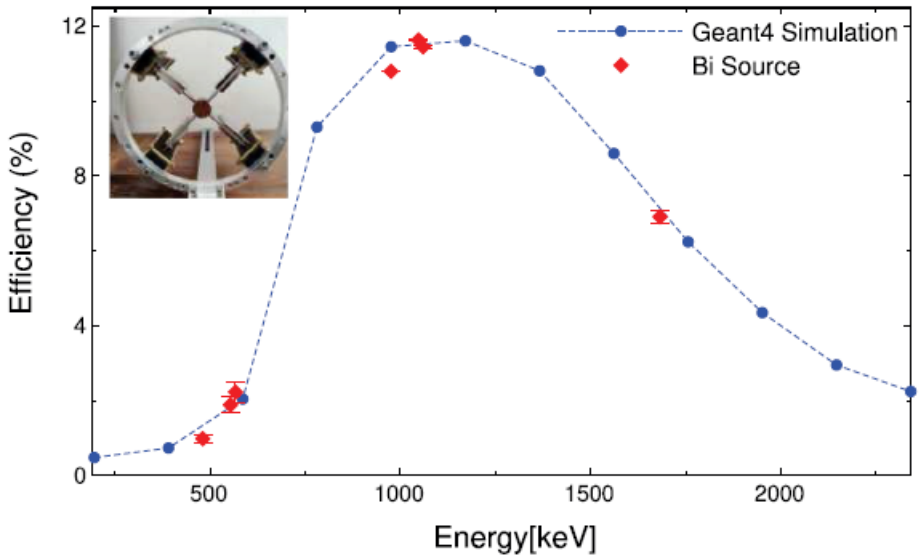

FIGURE 2.13: Efficiency of SLICES evaluated for a detector-source distance of 117 mm and utilizing four magnet clusters. The efficiency curve obtained from GEANT4 simulation is depicted by a blue dashed line, while the experimental data points obtained measuring conversion electrons from a source of radioactive ^{207}Bi are represented in red. An inset image showcases a photograph of the magnetic transport system that was assembled for this particular measurement [30]

2.4 Tape Station

The purpose of a tape station is to control the tape in which short lived radioactive isotopes are collected to allow energy resolution measurements in radioactive ion beam facilities. There are two possible working configurations for a tape station: in one case the implantation point is different then

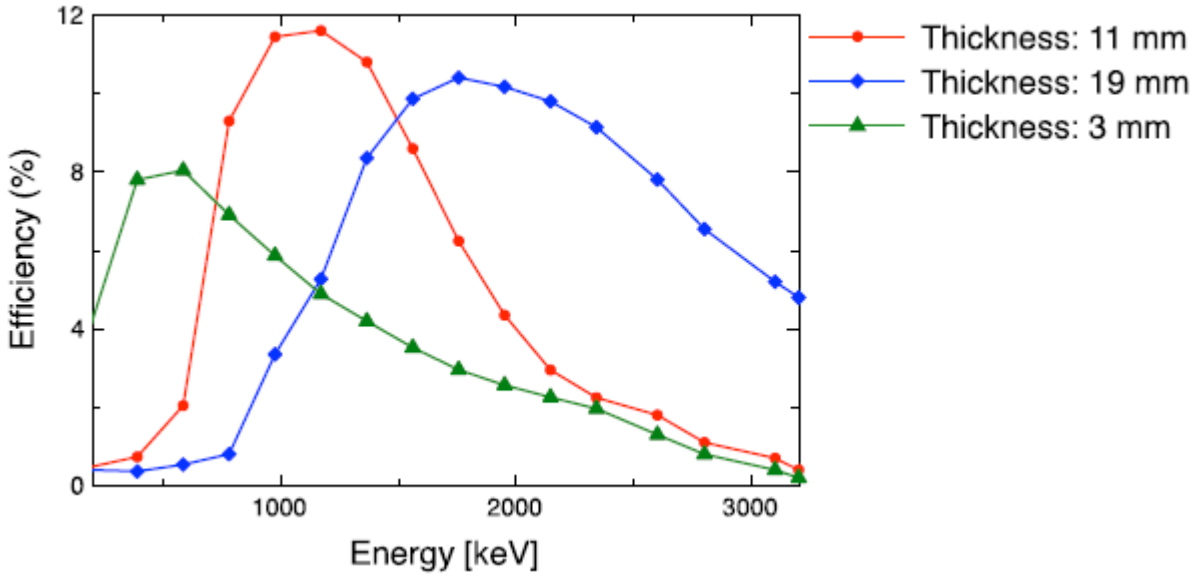

FIGURE 2.14: SLICES detection system absolute efficiency when the detector-source distance is 117 mm and four magnet clusters are used, with three different thicknesses: 3 mm (represented by green triangles), 11 mm (represented by red points), and 19 mm (represented by blue diamonds) [30].

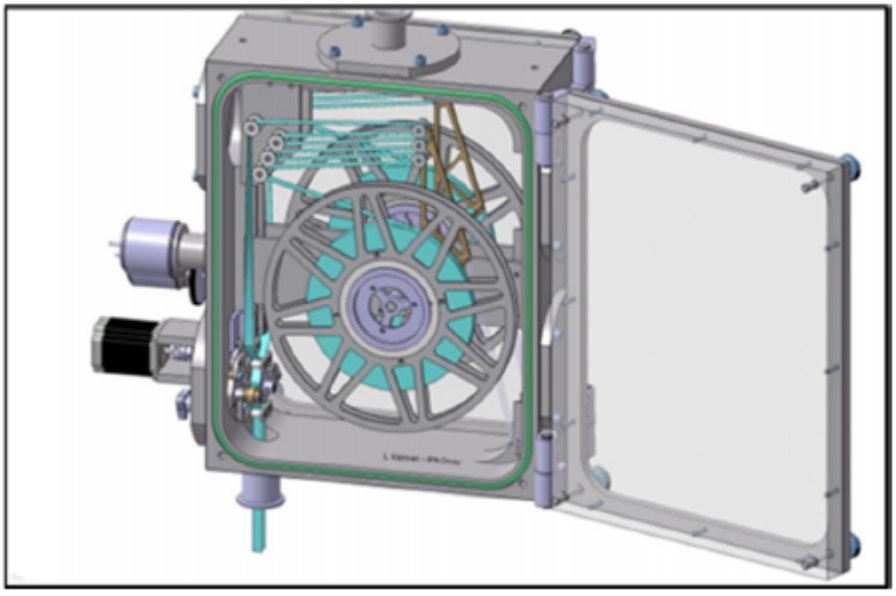

FIGURE 2.15: SPES tape cassette [32].

the measuring point and in the other they coincide. In the first case the scope of the possible measurable isotopes is limited by the speed of the tape station, as the implanted activity must be transported to the measuring point in a lower time then the isotope half life. In the second case there is no time

loss between implantation and measurement, however the implanted nuclei must be taken away from the measuring point before the number of daughter nuclei builds up to overwhelming values. The SPES tape station belongs to the first kind, ions are implanted in an aluminated mylar tape and then the needed information is extracted through γ spectroscopy and β-γ coincidence [32]. There are a total of two tape station in SPES one after the production of the ions composing the ion beam, located in the β decay station, while the other for diagnostic is placed before the high resolution mass spectrometer. The tape station cassette 2.15 consists of two disks that move the mylar tape in either direction in a similar fashion as a movie projector. The tape motion is controlled by a total of three motors, one is a stepper motor that defines the tape velocity and the direction, the other two are DC motors that roll the tape around the two disks. The tape station is being designed to drive the tape motion according to user programmable parameters, like speed, number of steps and of total cycles, and to coordinate with other subsystems acting as the master handler. To this purpose the master functions for tape motion control are going to be implemented all in the same server and the dialogue with other subsystems will be done through digital signals. This approach allows the servers for other subsystems to remain independent, avoiding the need for real time software communication. The logic behind the tape station control is already developed and is being used in IPN [33], a scheme of is shown in Fig. 2.16

The flux diagram of the logic presents different parallel processes for the user to design the experiment according to the experiment paramenters. For example it is possible to modify the rotation of the tape direction using different velocity profiles according to the initial configuration. Several tests have been performed on the tape station speed and stopping point precision. It was recorded that the top speed is 4.5 m/s, however in run of distance of 555 mm the tape reached a maximum speed of 2.1 m/s, finishing in 0.75 s and

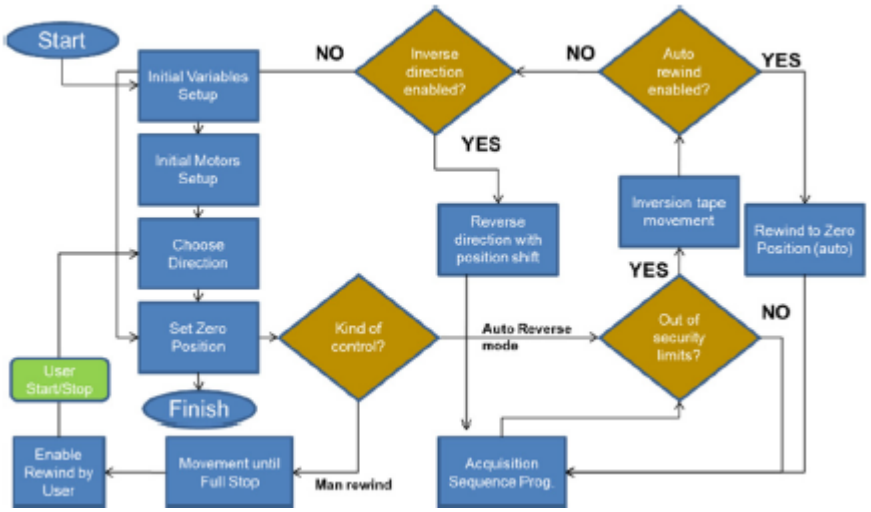

FIGURE 2.16: Logic to control the motor of the tape station [32].

with a stopping precision of 2 mm.

Chapter 3

β-Decay Station Performance Simulation

3.1 Introduction

In this chapter we have built a simulation of the β-decay station to try and assess its capabilities. Simulations of the experimental set-up performance are a powerful tool to obtain information on the feasibility of a measurement and to optimize the measuring procedure. In the case of the β decay station, a GEANT4 simulation can provide us with an accurate list of all the possible isotopes present on the tape through radioactive decay of the implanted specie. Through a simulation is also possible to establish the optimal implantation and measuring time windows given a fixed beam current value, in order to optimize the γ ray acquisition and the overall duration of the measurement. However, in typical working condition the β decay station will deal with very exotic species with little to no information on the database used by GEANT4. Furthermore, processes like the neutron delayed β decay are not considered and will have to be somewhat implemented to this purpose, a series of four software have been realized, in order to gain the needed information for an exhaustive simulation. These codes have been written in

Wolfram Mathematica 13.0 which is a powerful tool to solve both numerical and analytical problems and, more importantly, it gives easy access to the NNDC database to updated information. In our simulation ^{148}Cs was selected as the implanted specie due to its 146 ms half life, which provide a good example of a short lived isotope, while remaining compatible with the tape moving time. The following sections provides a detailed description as well as the functioning of the codes and the simulations. The codes we built aims to:

- create a complete isotope list of the ion of interest decay tree
- optimize the measuring time window for the γ and β spectroscopy
- create a proper input for GEANT4
- update the GEANT4 database

These codes need to be run before starting the simulation, in order to first obtain a

3.2 Isotope List

The primary objective of the first code is to provide a comprehensive list of all the radioactive species that exist within a selected isotope decay chain. The software also features the ability to eliminate long-lived isotopes, as isotopes with excessively long half-lives ($T_{1/2}$) are incompatible with the measurement type planned for the β Decay Station and could potentially overburden the computational process, thereby compromising the simulation precision. Finally, it is also possible to add by hand other values that may be deemed important for a correct evaluation of a measurement, or are simply not up to date with the latest measurements in the database, like the half life and

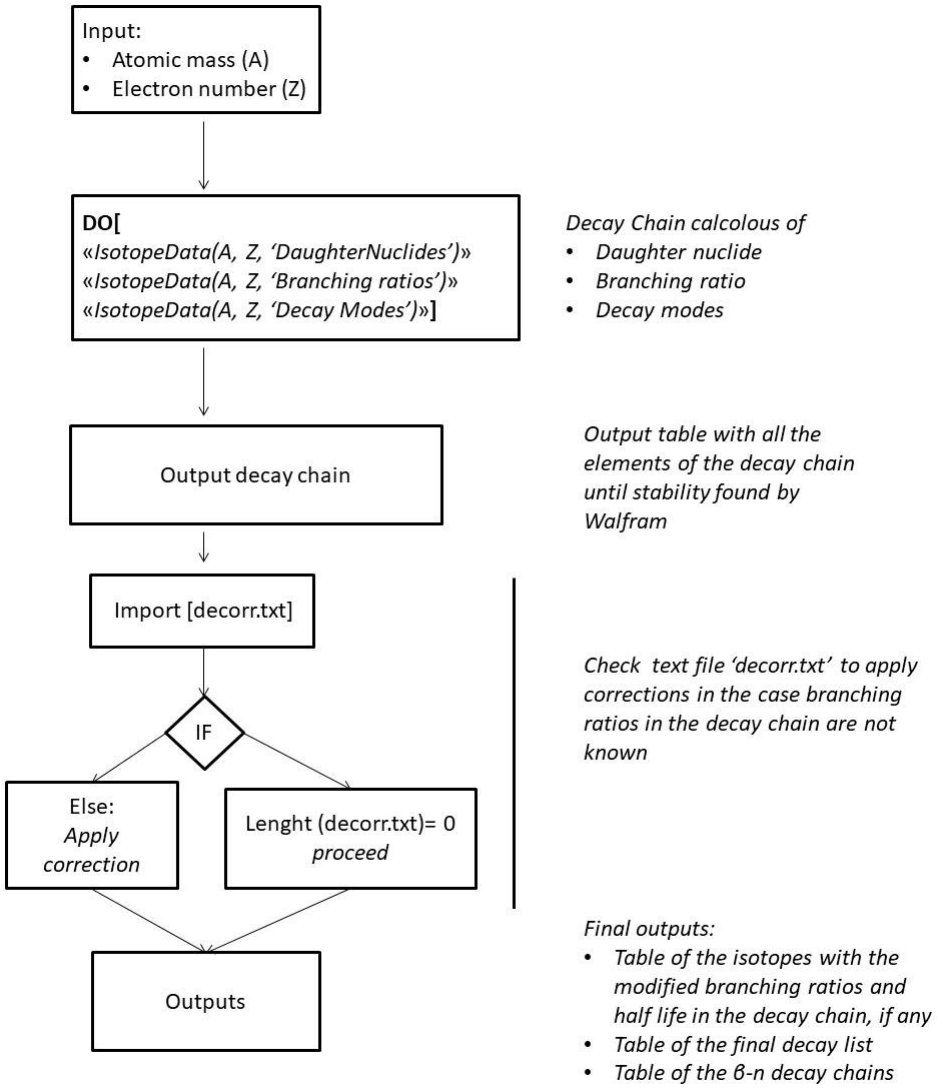

FIGURE 3.1: Flux diagram of the first code ("*Decaychain*) working princile. The code take the A and Z numbers of a desired isotopes and then proceeds to calculate the decay chain through the "*Wolfram Mathematica*" "*IsotopeData*" command. After the decay chain calculation the software apply corrections, if necessary, by reading the text file "*decorr.txt*" and finally produce three tables as outputs. The first table shows the isotopes with the modified branching ratios and halflives in the decay chains, the second one the final list of isotopes and the third one the β-n decay chains.

the branching ratio. The code takes the atomic mass A and the proton number Z of the father isotope, 158 and 55 respectively for ^{148}Cs, it then starts calculating the decay chain and stores all the daughter nuclides information like atomic number, branching ratio, decay mode and half life. The search of

the information on the decay chain is done with the Wolfram Mathematica database through the function *IsotopeData*, which given the the nucleus Z and A all the needed isotope properties for future calculation.
The code defines a function called "dNuclides" that takes an isotope entity as input and returns a list of its daughter nuclides, while removing any "Missing" elements from the list. A list of all the isotopes present in the decay is obtained by the function "chain" that takes an isotope entity as input and repeatedly finds the daughter nuclei until it reaches the stable isotope. It then generates a table of information for each daughter nuclide in the decay chain. Each row of the table contains the atomic number, neutron number, and half-life of the daughter nuclide, while removing any daughter nuclides with infinite half-lives (i.e. stable isotopes). The code then defines a loop that iterates over each row of the decay table. For each row, the loop retrieves the daughter nuclides, branching ratios, and decay modes using the "IsotopeData" function. The decay mode is determined using a user defined function, which takes the atomic and proton numbers of the parent and daughter nuclei as input. The function assigns a decay mode based on the differences in atomic and proton masses. If the proton number difference is one and the masses remain equal, then it is a β^--decay. If the proton number decreases by one, it could be a β^+-decay or electron capture. If the mass number decreases by one, while the difference in proton number is one, then it is a β^--delayed neutron emission. If the proton number increases, it is a β^+-delayed neutron emission. If the mass number difference is four and the proton number decreases by two, then it is α-decay. If the mass number difference is between two and three, the decay mode is unknown; otherwise, it is a fission process.

The code then iterates over each daughter nuclide and checks whether the corresponding branching ratio is a metastable state. Based on this check, the loop appends a new row to the table list that contains information about the decay process. Finally the table is then formatted for display again to

show branching ratios, and decay modes of the father and daughter nuclides in the decay process. In the case under consideration of ^{148}Cs, the list of the isotopes found by the code is shown in Fig. 3.2, while Fig. 3.3 shows the decay chain of ^{148}Cs with the β-delayed neutron processes.

3.3 Time Windows and Measuring Cycles

As already explained in the previous chapter, the β decay station is composed of two separate vacuum chambers, the first one for measuring the radiation emitted by the implanted species through the five GTC and the second one for measuring conversion electrons with the SLICES spectrometer. It is then necessary to consider two distinct measuring cycles, one for each of the two measuring points. The second software was designed to precisely determine the optimal irradiation and measurement time for the desired implanted isotope based on the fixed cycles times for the two stages. In the case of the γ station the measuring point and implantation points coincides, while for the β stage the implantation point is actually approximately 1 m above the implantation point. This means that in the first measurement there is no dead time introduced by the tape moving, but instead only an extra time of 25 μs is considered due to the beam opening and closing. Although, the β measuring stage is affected by a transportation time of approximately 500 ms. If we define the transportation time and irradiation time T_{TR} and T_{IRR} respectively, the measuring cycle for the γ rays goes as follows: the beam will irradiate the tape for a time T_{IRR} and then after a $T_{TR} > 25$ μs the beam is stopped and the measurement can start. Here T_{TR} actually only contains the time for the beam opening and closing since there is no transportation time, however it is still used for simplicity of notation. In the second stage, for the β measurement, the implantation time T_{IRR} and measuring time will be simultaneous, with the system only being offline for the duration of T_{TR}. Since after every

#	Father nuclide	Daughter nuclide	Halflife (s)	Decay branching	Decay type
1	$^{148}_{55}Cs_{93}$	$^{148}_{56}Ba_{92}$	0.146	0.75	BetaDecay
2	$^{148}_{55}Cs_{93}$	$^{147}_{56}Ba_{91}$	0.146	0.251	BetaDelayedNeutronEmission
3	$^{148}_{56}Ba_{92}$	$^{148}_{57}La_{91}$	0.611	1.0	BetaDecay
4	$^{148}_{56}Ba_{92}$	$^{147}_{57}La_{90}$	0.611	0.0040	BetaDelayedNeutronEmission
5	$^{147}_{56}Ba_{91}$	$^{147}_{57}La_{90}$	0.893	1.00	BetaDecay
6	$^{148}_{57}La_{91}$	$^{148}_{58}Ce_{90}$	1.26	1.0	BetaDecay
7	$^{148}_{57}La_{91}$	$^{147}_{58}Ce_{89}$	1.26	0.0015	BetaDelayedNeutronEmission
8	$^{147}_{57}La_{90}$	$^{147}_{58}Ce_{89}$	4.015	1.0	BetaDecay
9	$^{147}_{57}La_{90}$	$^{146}_{58}Ce_{88}$	4.015	0.00040	BetaDelayedNeutronEmission
10	$^{147}_{57}La_{90}$	$^{147}_{58}Ce_{89}$	4.015	1.0	BetaDecay
11	$^{147}_{57}La_{90}$	$^{146}_{58}Ce_{88}$	4.015	0.00040	BetaDelayedNeutronEmission
12	$^{148}_{58}Ce_{90}$	$^{148}_{59}Pr_{89}$	56.	1.00	BetaDecay
13	$^{147}_{58}Ce_{89}$	$^{147}_{59}Pr_{88}$	56.4	1.00	BetaDecay
14	$^{147}_{58}Ce_{89}$	$^{147}_{59}Pr_{88}$	56.4	1.00	BetaDecay
15	$^{146}_{58}Ce_{88}$	$^{146}_{59}Pr_{87}$	811.2	1.00	BetaDecay
16	$^{147}_{58}Ce_{89}$	$^{147}_{59}Pr_{88}$	56.4	1.00	BetaDecay
17	$^{146}_{58}Ce_{88}$	$^{146}_{59}Pr_{87}$	811.2	1.00	BetaDecay
18	$^{148}_{59}Pr_{89}$	$^{148}_{60}Nd_{88}$	137.	1.00	BetaDecay
19	$^{147}_{59}Pr_{88}$	$^{147}_{60}Nd_{87}$	804.	1.00	BetaDecay
20	$^{147}_{59}Pr_{88}$	$^{147}_{60}Nd_{87}$	804.	1.00	BetaDecay
21	$^{146}_{59}Pr_{87}$	$^{146}_{60}Nd_{86}$	1449.	1.00	BetaDecay
22	$^{147}_{59}Pr_{88}$	$^{147}_{60}Nd_{87}$	804.	1.00	BetaDecay
23	$^{146}_{59}Pr_{87}$	$^{146}_{60}Nd_{86}$	1449.	1.00	BetaDecay
24	$^{147}_{60}Nd_{87}$	$^{147}_{61}Pm_{86}$	9.487×10^{5}	1.00	BetaDecay
25	$^{147}_{60}Nd_{87}$	$^{147}_{61}Pm_{86}$	9.487×10^{5}	1.00	BetaDecay
26	$^{147}_{60}Nd_{87}$	$^{147}_{61}Pm_{86}$	9.487×10^{5}	1.00	BetaDecay
27	$^{148}_{62}Sm_{86}$	$^{144}_{60}Nd_{84}$	2.2×10^{23}	1.00	AlphaEmission
28	$^{144}_{58}Ce_{86}$	$^{144}_{59}Pr_{85}$	2.4616×10^{7}	1.00	BetaDecay
29	$^{147}_{61}Pm_{86}$	$^{147}_{62}Sm_{85}$	8.2732×10^{7}	1.00	BetaDecay
30	$^{147}_{61}Pm_{86}$	$^{147}_{62}Sm_{85}$	8.2732×10^{7}	1.00	BetaDecay
31	$^{146}_{62}Sm_{84}$	$^{142}_{60}Nd_{82}$	3.25×10^{15}	1.00	AlphaEmission
32	$^{142}_{58}Ce_{84}$	$^{138}_{56}Ba_{82}$	$2.\times10^{24}$	Unknown	AlphaEmission
33	$^{142}_{58}Ce_{84}$	$^{142}_{60}Nd_{82}$	$2.\times10^{24}$	Unknown	DoubleBetaDecay
34	$^{147}_{61}Pm_{86}$	$^{147}_{62}Sm_{85}$	8.2732×10^{7}	1.00	BetaDecay
35	$^{146}_{62}Sm_{84}$	$^{142}_{60}Nd_{82}$	3.25×10^{15}	1.00	AlphaEmission
36	$^{142}_{58}Ce_{84}$	$^{138}_{56}Ba_{82}$	$2.\times10^{24}$	Unknown	AlphaEmission
37	$^{142}_{58}Ce_{84}$	$^{142}_{60}Nd_{82}$	$2.\times10^{24}$	Unknown	DoubleBetaDecay
38	$^{144}_{60}Nd_{84}$	$^{140}_{58}Ce_{82}$	7.23×10^{22}	1.00	AlphaEmission
39	$^{144}_{59}Pr_{85}$	$^{144}_{60}Nd_{84}$	1037.	1.00	BetaDecay
40	$^{147}_{62}Sm_{85}$	$^{143}_{60}Nd_{83}$	3.35×10^{18}	1.00	AlphaEmission
41	$^{147}_{62}Sm_{85}$	$^{143}_{60}Nd_{83}$	3.35×10^{18}	1.00	AlphaEmission
42	$^{147}_{62}Sm_{85}$	$^{143}_{60}Nd_{83}$	3.35×10^{18}	1.00	AlphaEmission
43	$^{144}_{60}Nd_{84}$	$^{140}_{58}Ce_{82}$	7.23×10^{22}	1.00	AlphaEmission

FIGURE 3.2: Complete list of isotopes in the decay chain, as found by the software.

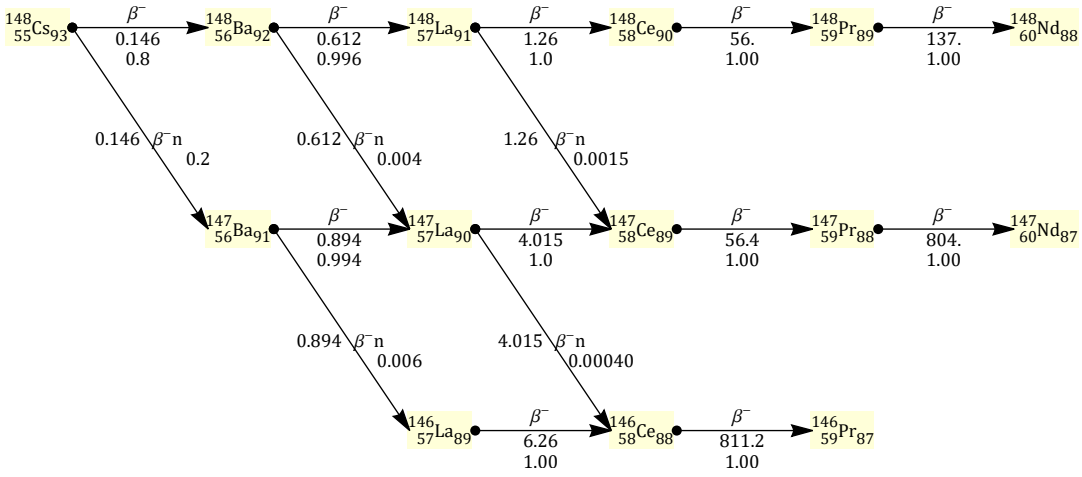

FIGURE 3.3: Decay chain obtained from the isotope of ^{148}Cs with the branching caused by the β^- with delayed neutron emission.

measuring cycle the tape is moved away and the implantation is performed in a brand new part of the tape, each implantation is independent from the other, hence it is possible to consider the results only of the first cycle and then multiplying by the number of cycle that would happen over all the desired duration of the experiment shift. The two measuring cycles for the γ and β cases are graphically explained in Fig. 3.4.

In the γ case the cycle consists of an irradiation time, a switching time to deflect the beam from the tape, the measuring time (T_{MEAS}) and finally the T_{TR} necessary to move away the tape in order to prevent the contaminants build up. In the β cycle instead the measurement only happens after the time T_{IRR} to irradiate the tape and the time T_{TR} to get the source to the measuring point. In this case, since the irradiation and the measurement stages happen in different locations of the tape, measurement and irradiation can be done at the same time, in order to save time especially when dealing with short lived isotopes. Let's consider an implantation time T_{IRR} and a beam current I_{BEAM}, for example 200 PPS, then the beam current is essentially a θ function with amplitude I_{IRR} for a time $T = T_{IRR} + T_{MEAS} + T_{TR}$ and zero

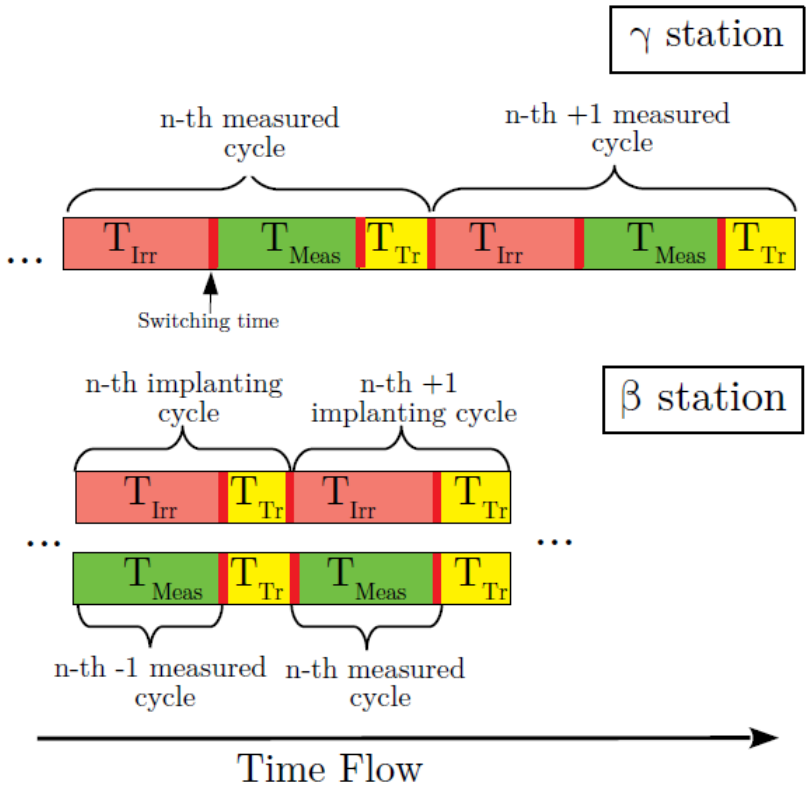

FIGURE 3.4: Measuring cycles for the γ (above) and β (bottom) stages.

elsewhere. Considering that the daughter isotope population is zero at $T = 0$, it is possible to solve the differential linear equation system in the case of the beam current previously defined, obtaining the implanted population. At this point it is possible to evaluate the population of the daughter isotope of interest, respect to the rest.

The implanted activity transportation time is fixed by the system characteristics, like how long the tape has to travel and the distance it must be put between two different implantations, however what can be optimized are T_{IRR} and the measuring time. The second code function is exactly to find the best irradiation and measuring windows. In order to do so, it considers the β decay of an isotope while remaining in the same mass, solving the linear equations system to estimate the decay branching ratio (in the example we are following it considers the atomic mass 148). The software takes in input the A and Z numbers of the isotope of interest and read the text file produced

by the decay chain code (discussed in the previous section), containing the information on the decay chain of the implanted isotope, and finally the tape transportation time and the beam current in pps. Fig. 3.7 shows a flux diagram of the program, the code finds a solution to the Bateman equation for several values of the measuring time and irradiation time, in order to establish the best combination of T_{IRR} and T_{MEAS} for the isotope of interest. As already explained in chapter 1, the decay process is described by the following equations:

$$\frac{dz_i}{dt} = \sum_{j<i} b_{ij}\lambda_j z_j - \lambda_i z_i. \tag{3.1}$$

Here z_i is the concentration of the i_{th} nuclide, λ is the decay constant of the isotope, b is the fraction of the j_{th} nuclide forming from the i_{th} isotope. We can define a lower diagonal matrix A:

$$A = \begin{pmatrix} -\lambda_0 & 0 & \dots & \dots & 0 \\ b_{10}\lambda_0 & -\lambda_1 & 0 & \dots & \vdots \\ b_{20}\lambda_0 & b_21\lambda_1 & -\lambda_2 & 0 & \vdots \\ \vdots & \vdots & \vdots & \ddots & \\ b_{N0}\lambda_0 s & \dots & \dots & \dots & -\lambda_N \end{pmatrix} \tag{3.2}$$

and express eq. 3.1:

$$\begin{pmatrix} \frac{dv_1}{dt} \\ \vdots \\ \frac{dv_N}{dt} \end{pmatrix} = A \times \begin{pmatrix} u_1 \\ \vdots \\ u_N \end{pmatrix} \tag{3.3}$$

The software solves eq. 3.3 numerically using the built in Mathematica function "NDsolve". It is also possible to set some optional parameters for "NDSolve", such as the accuracy and precision of the numerical solution, and the maximum size of the time step.

The output of NDSolve is a list of functions that represent the solution to the system of differential equations over the specified time domain. These functions are then used to compute the activity of each nuclide at each time step, and to integrate the activity over the measurement period to obtain the measured decay counts. Finally, it generates a color map of the number of measured decays as a function of irradiation and measurement times. The output of the code is a plot that shows the optimum irradiation and measurement times for the detection of the initial isotope, ^{148}Cs in our case (Fig. 3.5). The activity for several radioactive species following the decay of the implanted ^{148}Cs, as a function of time, are shown in Fig. 3.6. The light red area indicates the population trend during the irradiation process, the yellow one represents the dead time introduced by the electromagnetic beam deflector (25 μs), the light green area is the measuring interval, while the gray one is the time the tape takes to move away from the measuring position.

3.4 GEANT4 Input

The third code was developed to produce a proper GEANT4 input file to start the simulation. The GEANT4 database do not consider lower masses in the radioactive decay chain formed from the delayed neutron emission process. It is therefore necessary to add in the input file the isotopes caused by the β delayed neutron emission. In dealing with this kind of problems, it is important to consider the β-neutron decay timing of the process and its β decay yield. When it comes to the events timing, the measuring cycle described in sec 3.4 needs to be taken into consideration. The delay of the nth event, T_n, produced by GEANT4 is:

$$T_n = T_{IRR} \cdot n/n_{tot}, \tag{3.4}$$

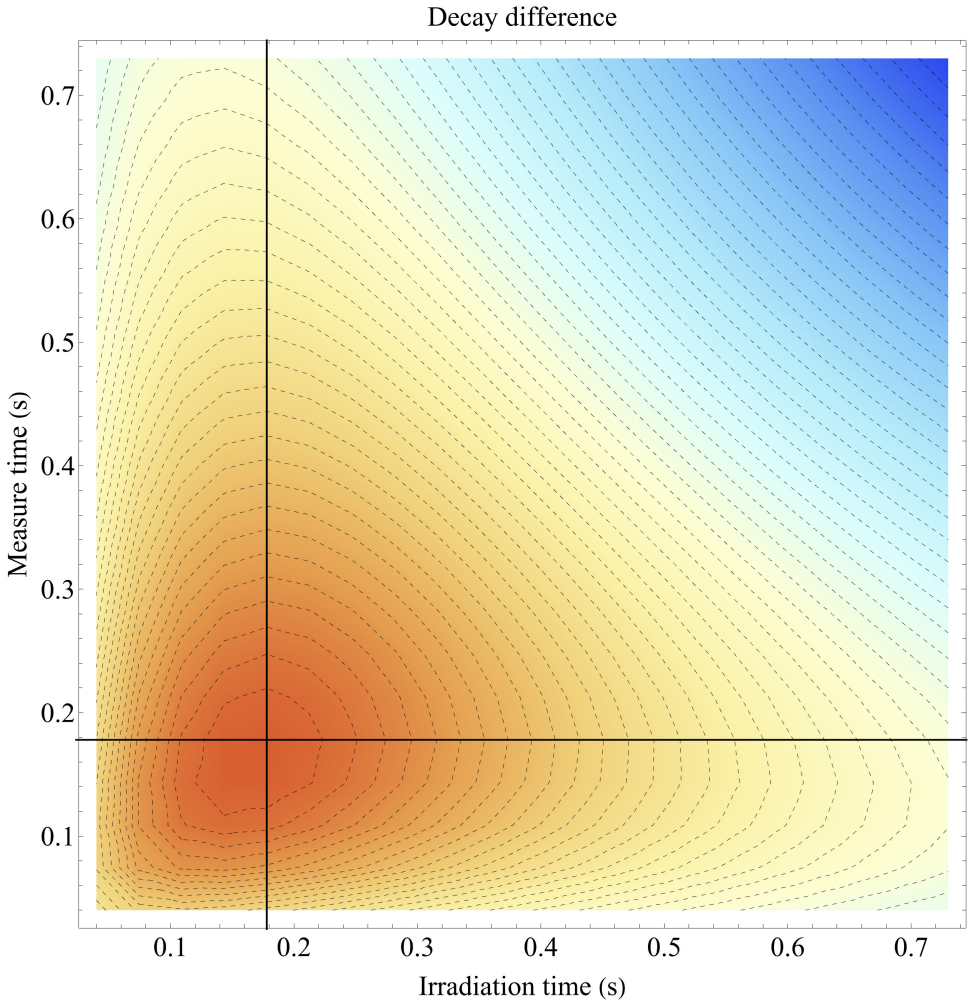

FIGURE 3.5: Color map showing the activity of the implanted ^{148}Cs as a function of the irradiation time and the measuring time.

where n_{tot} is the total number of events in the GEANT4 simulation and T_{IRR} is the irradiation time, assuming a uniform beam current I_{beam}. Due to the initial uniform delay and the random exponential decay connected to the *beta* decay, which is directly considered by GEANT4, the subsequent isotope with the same mass is generated at the appropriate time after the primary vertex for that isotope has been generated. However, the β neutron delayed process, which must be manually added, makes temporization at lower masses more difficult. The first closer mass should be created with a delay which is the sum of the uniform delay for the implantation of the father and a random exponential delay with decay constant $\lambda = \mathrm{Log}[2]/T_{1/2}$,

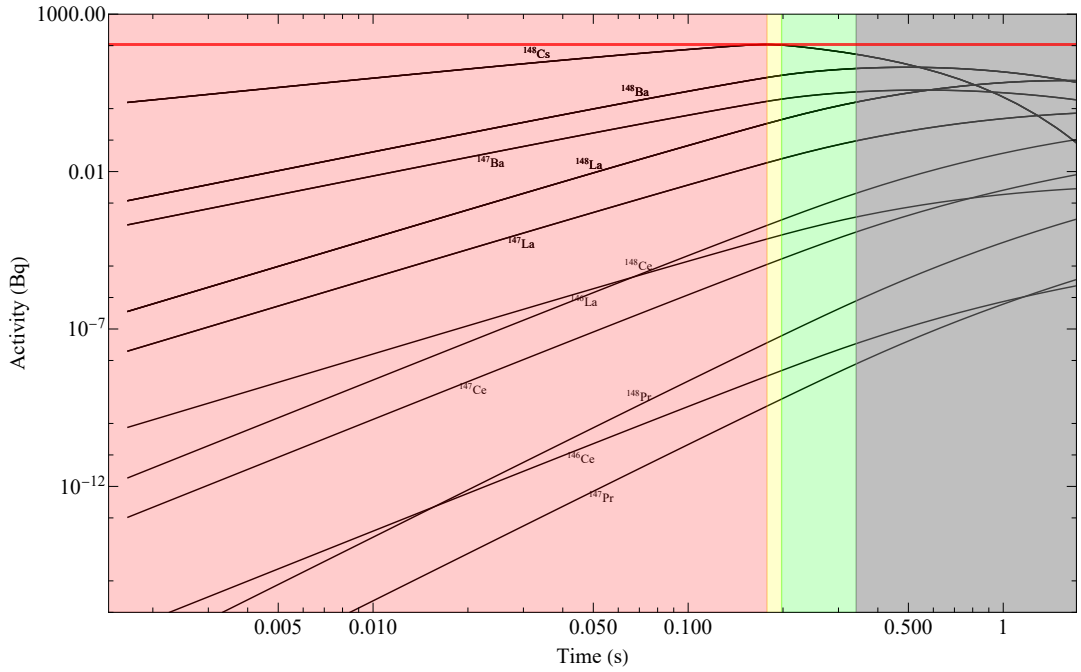

FIGURE 3.6: Plotted activities as a function of time of different nuclear species generated after the decay decay of the implanted ^{148}Cs isotope, according to the code. The light red area is the population trend during the irradiation stage, the yellow one represents the dead time introduced by the electromagnetic beam deflector (25 μs), the light green stage is during the measurement interval, and the gray area indicates the time after the displacement of the tape from the measure position.

where is the half life of the father. The same argument can be done for the subsequent β-n decay and the uniform delay must be added to the random exponential delay that connects the new isotope to the father, in such a way:

$$\begin{cases} e^{-\lambda_1 \cdot t} \\ \frac{e^{-\lambda_1 \cdot t}}{\lambda_2 - \lambda_1} \\ \frac{e^{-\lambda_1 \cdot t}}{(\lambda_2 - \lambda_1)\cdot(\lambda_3 - \lambda_1)} + \frac{e^{-\lambda_2 \cdot t}}{(\lambda_1 - \lambda_2)\cdot(\lambda_3 - \lambda_2)} + \frac{e^{-\lambda_3 \cdot t}}{(\lambda_1 - \lambda_3)\cdot(\lambda_2 - \lambda_3)} \end{cases}$$

In order to understand the yield of the β decay, it is necessary to understand the physics of the β neutron delayed process. The probability for β decay is P_β = 1 - $P_{\beta-n}$ because the β-neutron decay is a competitive process to the β decay that occurs with a probability of $P_{\beta-n}$. When the Q-value of

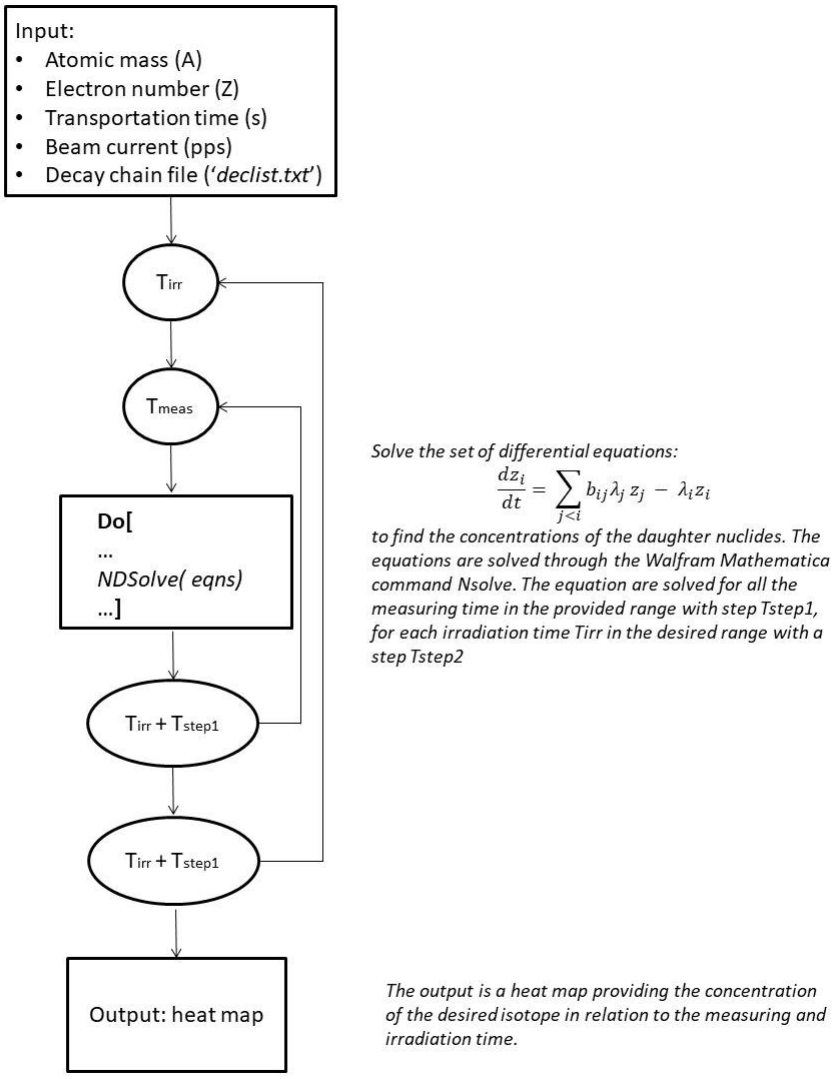

FIGURE 3.7: Flux diagram of the second software. It recieves in input the atominc mass (A) and the number of electron Z, along with the tape transportation time (in seconds), the proton beam current (in pps) and the decay text file generated with the first software. The differential equation to evaluate the concentration of isotopes implanted for a wide range of measuring time and irradiation time. It generates in output a heat map showing the best measuring and irradiation time for to maximize the number of isotope implanted.

the decay is high, the father nucleus can feed either the discrete excited state of the daughter or the quasi-continuum states. The de-exitation process can then progress with a neutron emission to the exited state of the A-1 mass nucleus or it can continue with a cascade of γ rays, in the case the quasi-continuum state of the daughter is fed. The likelihood of falling either into

the discrete or in the quasi continuum states is taken into account in the probability P_β. Since there is no possibility to correctly measure the cascade of γ rays in the quasi continuum state, due to the pandemonium effect explained in sec. 1.5.3, some approximations must be done. The first approximation is to consider that each time the father nucleus goes into the quasi continuum states of the daughter, a neutron emission follows to reach the excited state of the A-1 isotope, while maintaining the $P_{\beta-n}/P_\beta$ ratio. The energy of a β transition that populate the quasi continuum states ranges between 0 and Q_{β^-} - $Q_{\beta-n}$ -$\epsilon^*_{\substack{A-1\\N-1}Y_{Z+1}}$, where Q_{β^-} and $Q_{\beta-n}$ are given by:

$$\begin{cases} Q_{\beta^-} = \{M[Z,A] - M[Z+1,A]\} \cdot c^2 \\ Q_{\beta-n} = \{M[Z,A] - M[Z+1,A-1] - m_n\} \cdot c^2 \end{cases} \tag{3.5}$$

and $\epsilon^*_{\substack{A-1\\N-1}Y_{Z+1}}$ is a generic exited state of the daughter nuclide. Therefore, the quasi-continuum state energy varies between $Q_{\beta-n}$ + ϵ and Q_{β^-}. According to the Effective Level Density (EDM), the Maxwell Boltzmann distribution indicates the likelihood of decaying to one of these levels, where the Maxwell Boltzmann is as usual

$$\rho[E] = \frac{e^{a_d \cdot \sqrt{E[MeV]}}}{E[MeV]^{\frac{3}{2}}} \tag{3.6}$$

where a_d is a fitting parameter dependent on the number of neutrons N and the protons number Z in the following way

$$a_d = a_1 N' + a_2 Z' + a_3 \sqrt{N} + e^m. \tag{3.7}$$

N' and Z' are:

$$\begin{cases} N' = N - (N'_m + 2) \\ Z' = Z - Z'_m \end{cases} \tag{3.8}$$

and finally m is $m_n/\sqrt{N}$ where N - 2 is a magic number (28, 50 or 82) and 0 elsewhere.

Here a_1, a_2, a_3, a_3 and m_n are fitting parameters and are listed in Tab 3.1 [34].

	Even-Even	Odd	Odd-Odd
a_1	0.011	0.0013	0.0097
a_2	-0.0347	-0.0285	-0.0513
a_3	-0.36	-0.4462	-0.3908
m_n	4.7785	3.4462	6.1302

TABLE 3.1: Fitting Parameters for the Maxwell Boltzmann distribution, indicating the likelihood of decaying into a quasi continuum state.

Another important assumption is that the probability of a β^- decay to the quasi continuum states with energy range [E, E+ΔE] is proportional to the number of states in the energy interval, ϕ[E] · ΔE, the electron yield if the decay from the ground state of the father to the quasi continuum is defined by the Fermi theory:

$$P(x, Q_{val}, Z_D) = N \cdot F(x, Z_D) \cdot (x + m_e \cdot c^2) \cdot \sqrt{x^2 + 2m_e c^2 x} \\ (Q_{val} - x)^2 \frac{e^{a_d \sqrt{E(MeV)}}}{E(MeV)^{\frac{3}{2}}} \tag{3.9}$$

where F is the Coulomb function is defined as usual as:

$$F(x, Z_D) = \frac{(1 + e^{\pm 2\pi Z_D \alpha}) \cdot (x + m_e c^2)/x}{1 - e^{\pm 2\pi Z_D \alpha (x + m_e c^2)/x}} \tag{3.10}$$

The sign +, in eq. 3.10, represents β^+ decay and - represents β^- decay. The variable P should be calculated by integrating over all values of the electron's kinetic energy (x) between 0 and Qβ^- - Q$\beta - n$ -ϵ, where α is the fine structure constant (specifically, 1/137 for ^{148}Cs).

$$P_e^-(x, Z_D) = \int_x^{Q_{\beta^-} - Q_{\beta^- n} - \epsilon^*} P(x, Q_{val}, Z_D) \cdot dE \tag{3.11}$$

This calculation must be repeated for each quasi continuum energy state that is populated in the decay chain. The results of each calculation must then be added together and weighted by the probability of populating each specific state. However, in our calculation we assumed that there is only one possible excited state of the nucleus ${}^{A-1}_{N-1}\mathrm{Y}_{Z+1}$, as the β-n decay process is not well understood in many cases, making it difficult to obtain the necessary information about the excited states of the nucleus ${}^{A-1}_{N-1}\mathrm{Y}_{Z+1}$. The goal of the simulation is to check the intensities of the gamma transitions and ensure that the lines do not overlap. To accomplish this, the simulation only considers the highest excited state of the daughter nucleus ${}^{A-1}_{N-1}\mathrm{Y}_{Z+1}$. The code takes in four inputs: I_{BEAM}, T_{IRR},T_{TR} and T_{MEAS}. It then defines a function "bfunc" that take T_{IRR} and T_{TR} and models the activation of the beam during the irradiation period. The code continues to calculate the total number of implantations, which is the expected number of radioactive decays that will occur during the experiment. The next section of the code calculates the beta emission spectrum for each decay. This involves the Coulomb correction factor for the beta yield, the density of states in the final (daughter) nucleus which are used to calculate the beta emission yield for a given energy range. Once the beta emission yield is calculated, the code generates a set of Monte Carlo simulations to model the behavior of the radioactive decay process, taking into account the parameters defined earlier. The output of the simulations is then used to create histograms of the beta energy spectra for each decay.

At this point a list of delayed neutron emitters is identified and sorted. For each delayed neutron emitter, it finds the corresponding decay products and calculates their populations. It then solves a system of ordinary differential

equations to determine the time evolution of the populations. Finally, it adds the new isotopes and their populations to the existing lists.

The software then generates a table of results related to implanted ions, with various properties and parameters listed in different columns which are various properties such as "Nuclide", "Z", "A", "Half-life", etc. . It then remove duplicates from the lists and create another list called "decfilev" that contains information about nuclear decays. This list contains the same information as the previous one, but with the number of decays multiplied by the total number of implantations. Finally, It creates a list called "bndec" that contains information about beta-minus decays. The information is extracted from the output of the previous mathematica code ("decaychain"). The "bndec" list contains information about the properties of the beta-minus decay, such as the Q value and the branching ratio. In the last part of the code, several operations are performed to transform the data acquired into a useful format for the Geant4 input file.

In summary, the code produces several outputs, including a table with information about the experimental setup and the number of implanted ions, and all the information about the β yield needed for the GEANT4 input file (Fig. 3.8) to correctly simulate the β-n emission. The input file is divided into different sections, one for each of the most common β-n emitters. The last output includes the I$BEAM$, TIRR,T$_{TR}$ needed to reproduce the uniform implantation delay and the half-life of the specific β-n emitters used to produce the exponential delay time of the produced isotope. Fig. 3.9 shows the flux diagram of the third code.

```
#
/run/verbose 0
/event/verbose 0
/process/had/rdm/setRadioactiveDecayFile 55 148 RadioactiveDecay_out/z55.a148
/process/had/rdm/setRadioactiveDecayFile 57 148 RadioactiveDecay_out/z57.a148
/process/had/rdm/setRadioactiveDecayFile 55 147 RadioactiveDecay_out/z55.a147
/process/had/rdm/setRadioactiveDecayFile 56 146 RadioactiveDecay_out/z56.a146

/process/had/rdm/setPhotoEvaporationFile 56 148 PhotonEvaporation_out/z56.a148
/process/had/rdm/setPhotoEvaporationFile 57 148 PhotonEvaporation_out/z57.a148
/process/had/rdm/setPhotoEvaporationFile 58 148 PhotonEvaporation_out/z58.a148
/process/had/rdm/setPhotoEvaporationFile 56 147 PhotonEvaporation_out/z56.a147
/process/had/rdm/setPhotoEvaporationFile 57 147 PhotonEvaporation_out/z57.a147
/process/had/rdm/setPhotoEvaporationFile 58 147 PhotonEvaporation_out/z58.a148
/process/had/rdm/setPhotoEvaporationFile 57 146 PhotonEvaporation_out/z57.a146

#/tracking/verbose 0
#IMPLANTED ION
/gps/source/intensity 1
/gps/particle ion
/gps/ion 55 148 0 0.
```

FIGURE 3.8: Input text file for the GEANT4 simulation.

3.5 Update

As previously mentioned, the simulation requires the informations on exotic species, so the GEANT4 database may not be up to date with the latest measurements of γ transitions and intensities. To address this, it is necessary to access the Experimental Unevaluated Nuclear Data List (XUNDL). The data sets for the radioactive decay option of GEANT4 are located in the folders "RadioactiveDecayX.Y" and "PhotonEvaporationX′.Y′", where X.Y and X′.Y′ are the version numbers, for example 5.6 and 5.7 for EvaporationDecay and PhotonEvaporation respectively. The first folder contains all the information required for the parent-to-daughter decay process, such as which levels are populated, while the second contains data for the generation of gamma and beta transitions. Both of these databases must be updated with the information available on the ENDF database.

The code begins by reading in the "PhotonEvaporation" file and the "ENDF" database, merging all levels found in both sources to ensure completeness. The levels are defined by their energy, spin, and parity.

The code then evaluates the energy differences between all pairs of levels

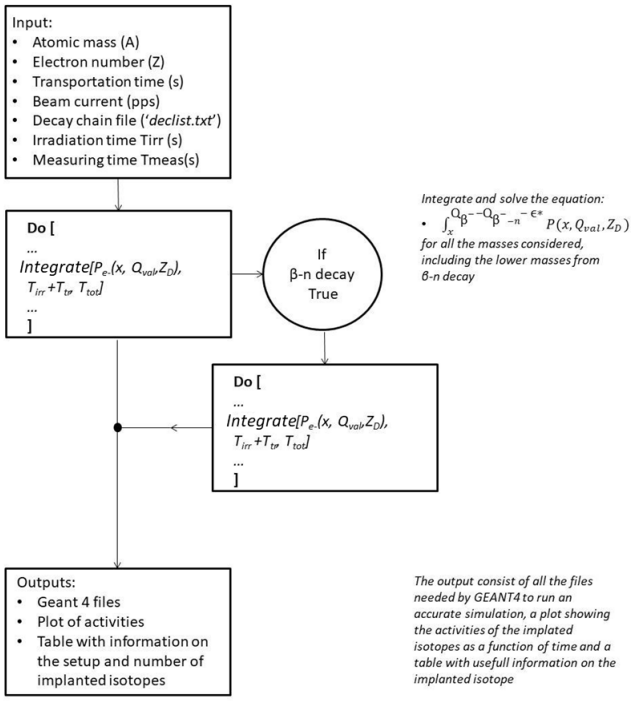

FIGURE 3.9: Flux diagram of the third software. It receives in input the atomic mass (A) and the number of electron Z, along with the tape transportation time (in seconds), the proton beam current (in pps), the decay text file generated with the first software, the irradiation and measuring times (in seconds). It calculates the populated radiactive species and generates all the files for GEANT4 to run a precise simulation, the plotted activities as functions of time for all the isotopes and a table containing useful information on the implated isotope.

and compares them to the transitions present in "PhotonEvaporation" and "ENDF". If a gamma transition is present in the GEANT4 database, the code uses the information in "PhotonEvaporation". However, if the transition is only present in "ENDF", additional information needs to be integrated.

If the multipolarity and parity/spin of the parent or daughter nucleus are known, then all necessary information for the simulation is available. Otherwise, the code assigns the transition as E1 or M1, as these are the most common types.

The "ENSDF" database does not provide the conversion coefficients of the transition. Therefore, the code estimates them using a Bezier function. The

Bezier functions are smooth and continuous functions defined for a set of n+1 control points P0, P1, ..., Pn. The Bezier function for a given transition is defined as:

$$B(t) = \sum_{i=0}^{n} B_{i,n}(t) \cdot P_i \tag{3.12}$$

where $B_{i,n}(t) = \frac{n!}{(i!\cdot(n-i)!)\cdot t_i \cdot (1-t)^{n-i}}$, t_i is a scalar parameter between 0 and 1 that defines the position along the curve, and P_i is the i-th control point.

The code also identifies the β transitions not present in "PhotonEvaporation" but present in the "ENDF" database and evaluates the Q-value of the transitions. The Q-value is computed from the mean energy of the β-decay, provided by "ENDF" (EAV), using the Fermi function. The equation for the Q-value is given by:

$$\frac{\int_0^Q x \cdot F(x,Q)dx}{\int_0^Q F(x,Q)dx} = EAV$$

where $F(x,Q)$ is the Fermi function.

The code then updates both "PhotonEvaporation" and the "RadioactiveDecay" files in a format suitable for GEANT4, including all the necessary information for the simulation.

Finally, the code calculates the conversion coefficients for E0 transitions, which are transitions between two excited states with a change in angular momentum quantum number of 0. These coefficients are calculated separately using a similar approach as for the E2 transitions. The calculated conversion coefficients are then used to update the photon evaporation database.

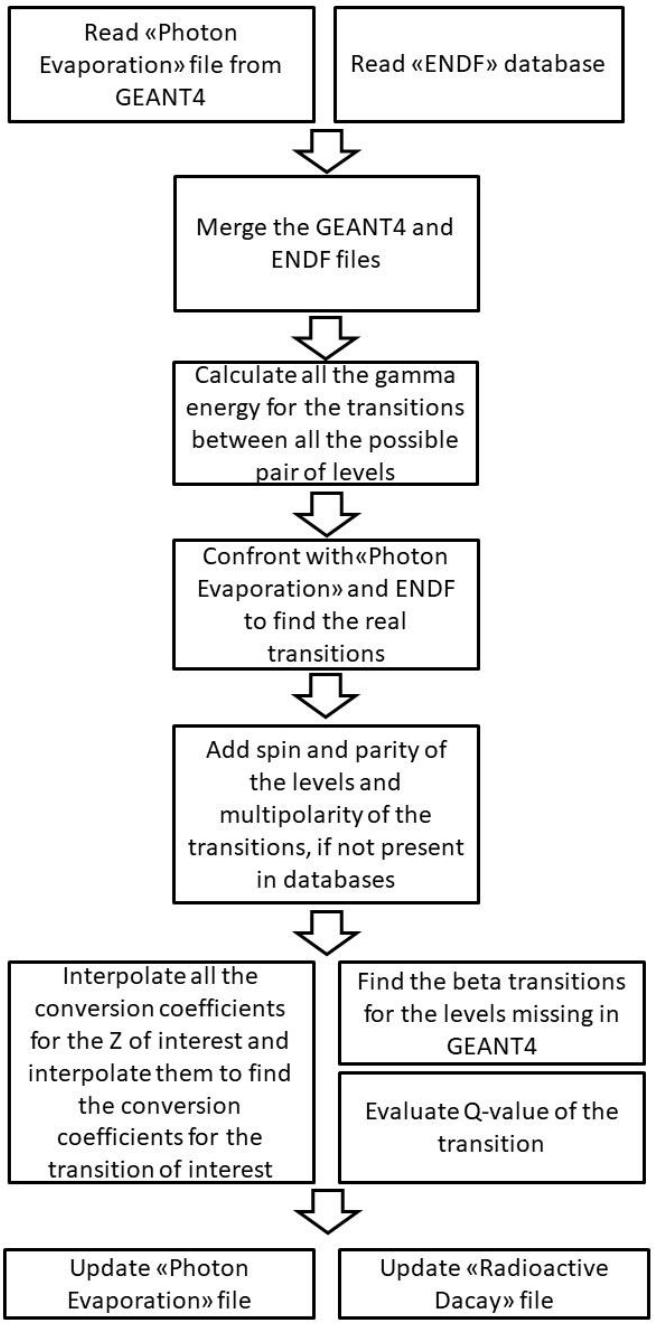

FIGURE 3.10: Flux diagram for the fourth software. The code takes data from the photon evaporation and radioactive decay database of GEANT4 and updates them with information found on the ENDF database. It also calculate coversion coefficient in case are not found in GEAT4 database.

3.6 β Decay Station Simulation

3.6.1 GEANT4 introduction

GEANT4 is a free, open-source simulation package designed to accurately model the interactions between particles and matter as the particles traverse through it. The software operates over a broad energy range and is implemented in the C++ programming language. The physical interactions between particles and matter are modeled through the application of object-oriented programming techniques, utilizing Monte Carlo techniques through both composition and rejection methods.

These methods have become widely adopted by the physics community as an effective means of simulating and verifying the performance of detection systems. The GEANT4 software is arranged into seventeenth class categories, with the categories highlighted in red in the figure forming the kernel of the toolkit. This kernel provides essential functionality such as managing runs, events, tracks, steps, hits, and trajectories, implementing GEANT4 as a state machine and providing a framework for physics processes, visualization drivers, graphical user interfaces, persistency, histogramming and analysis, as well as user code.

The "global" category manages units of measure, constants, and random numbers. The "particle" and "material" categories contain the necessary functions to describe the particle physics and its interaction with matter, while the "geometry" category allows for the establishment of a geometrical structure in which to propagate the particles. The "track" and "process" categories provide the implementations for the models for physical interactions, such as electromagnetic interactions of leptons, photons, hadrons, ions, and hadronic interactions. The "tracking" category oversees the "process" category to manage the evolution of the particle track. The "event" category manages the events in terms of their tracks, while the "run" category manages collections

of events that share a common beam and detector implementation. Finally, the "readout" category manages pile-up.

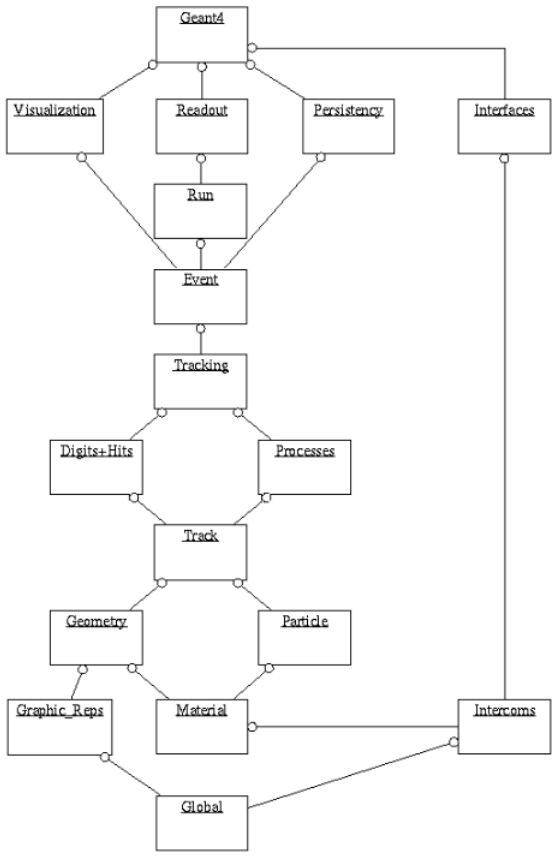

FIGURE 3.11: GEANT4 block diagram showing the varius categories and dependecies.

The GEANT4 toolkit for Monte Carlo high energy particle transport is known as the GPS (General Particle Source). It provides a platform for the specification of the spectral, spatial, and angular distribution of primary particle sources. The tool is configured for applications through either command line inputs or macro-based inputs. A diagram of the GPS class dependencies can be seen in Fig. 3.11. The General Particle Source Data, which is a thread-safe singleton, provides access to the source information for the GPS class. It is possible to have multiple instantiations of GPS, each with its own unique positional, angular, and energy distributions, as well as incident particle types.

The GPS allows for various spatial configurations, including spatial sampling

on 2D or 3D surfaces. The angular distribution can be set to be isotropic, cosine low, beam, or arbitrary. The energy spectrum can be linear, exponential power low, Gaussian, blackbody-like, or piecewise. The GPS also allows for the handling of multiple sources. here are various fundamental shapes that can be utilized to define the location of particles. The simplest among them is a point source, which can be considered as a single point in space. In addition to point sources, there are also planar sources such as disks, circles, and ellipsoids, as well as 1D and 2D accelerator beam spots. Furthermore, there is the option to use GPS to define volumes, which allows particles to be confined within a surface or distributed throughout a volume. The 3D shapes that are available include spheres, ellipsoids, cylinders, and parallelepipeds. To facilitate the definition of sources, the planes and shapes are conventionally aligned with a specific direction relative to the coordinate axes. However, it is possible to provide vectors that can be used to rotate the axis system.

3.6.2 Efficiency Simulation

In the β-decay station the RIB beam is transported to the implantation point of the β decay station by a an electrostatic quadrupole triple lens. Since it has been calculated that the beam spot will have a diameter of 3 mm, the simulation considers the radioactive source has a disk with a 1.5 mm radius placed in the origin (0,0,0). Furthermore the source in the simulation is surrounded by a mylar cylinder 20 μm thick and with a 2 mm radius. The mylar cover is added due to the kinetic recoil effect that GEANT4 assigns to the daughter nucleus in the decay process when the GEANT4 *"RadioactiveDecay"* options is used. In this way, the next species in the decay chain is prevented from moving away the implantation point, which would invalidate the results of any simulation, since long lived isotopes will possess much more statistics then the short lived ones. Furthermore the mylar volume can give precise

information on the time of creation of daughter nuclei which, together with the γ ray time of arrival in the Ge triple clusters help in creating time correlations. However, the evaluation of the detection efficiency of the setup is done through a prompt source, without radioactive decay. The prompt source emits one gamma for each event uniformly from a list counting energy values between 10 keV and 4 MeV. In order to test the scintillators-Ge coincidence each gamma emission is paired with an electron with energy between 0 and 9 MeV. The electrons are emitted with a flat energy distribution to better evaluate the scintillator detection efficiency. The detectors where assigned a timed resolution of 50 ns, 10 ns and 5 ns for the Ge triple clusters, the BGO and the plastic scintillators respectively. It was then assumed that the plastic scintillators operated with energy resolution of 15.8%, 22 % the BGO, while the energy resolution of the Ge triple cluster is defined by following formula:

$$FWHM[keV] = \sqrt{P_0 + P_1 \cdot E[keV] + P_2 \cdot E[kev]^2} \tag{3.13}$$

where P_0 = 2.651, P_1 = 1.832 x 10^{-3} and P_2 = 4.8127 x 10^{-3}. The energy thresholds for the BGO and the Ge clusters were both set to 5 keV and the coincidence window between the two, for the compton suppression, is set to 20 ns. The coincidence for the beta tagging measurement fires only when both the energy enetering the Ge surpass the energy thresholds. The results for the detection efficiencies are shown in Fig. 3.12 for three configurations. The first case is for the five Ge triple clusters after the add-back configuration, which means that energies left in different Ge crystals, but with the same timestamps are summed. In the second case is added the anti coincidences with the BGO, while the last one is also in coincidence with the scintillators. To decide the scintillators energy threshold, several simulations where performed. It appears that beta events can be definetly selected with a 500 keV

threshold (Fig. 3.13).

Furthermore the efficiency of the GTC system have been tested with two different configurations in add back configuration and compton suppression. The results are shown in Fig. 3.12, the black curve indicates the add back configuration, the blue one the add-back plus compton suppression configuration, where the compton suppression in performed with the anticoincidence between the HPGe and the BGO. Finally the orange curve in the efficiency in the case of add back plus β-tagging. The continuous lines are the detectors in the closest position possible to the source and without the Heviment absorber, while the dashed lines are the same but in the furthest position and with the absorber inserted. As a point of reference, at the energy of the first gamma of ^{60}Co (1332 keV), the highest efficiency (closest position and no Hevimet) was of 3.5%.

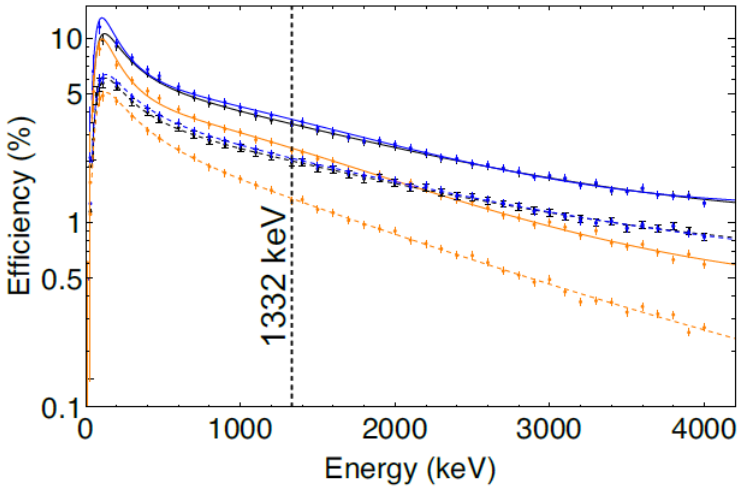

FIGURE 3.12: Efficiency curves of the HTC, the black curve indicates the add back configuration, the blue one the add-back plus compton suppression configuration, where the compton suppression in performed with the anticoincidence between the HPGe and the BGO. Finally the orange curve in the efficiency in the case of add back plus β-tagging. The continuous lines are the detectors in the closest position possible to the source and without the heaviment absorber, while the the dashed lines are the same but in the furthest position and with the absorber inserted.

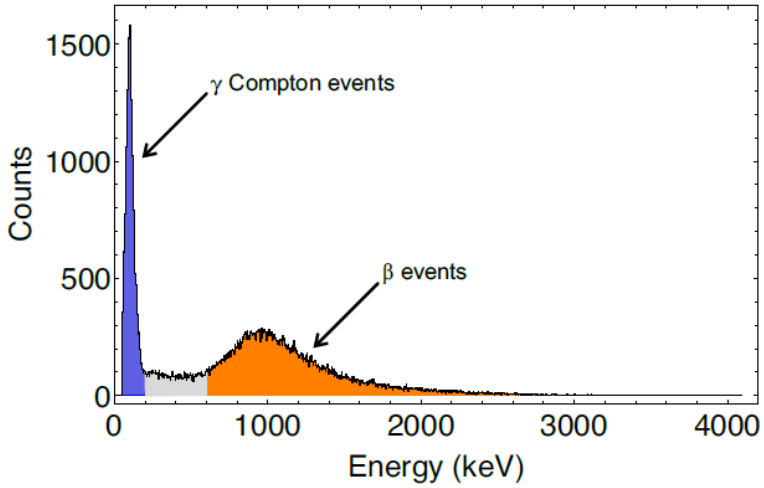

FIGURE 3.13: GEANT4 simulation of an acquisition of ^{148}Cs isotope. The result shows a net separation between the γ-compton and β events.

3.6.3 Simulation with Isotope ^{148}Cs

The simulations is composed by the following classes:

- Action Initialization
- Biased RDP Physics
- Detector Construction
- Event Action
- Histo Manager
- Primary generator action
- Physics List
- Stepping Action
- Tracking Action

the Action Initialization file is responsible for initializing the user-defined actions that will be taken during the simulation. These actions include defining the geometry, setting up the particle source, defining the physics processes to be simulated, and specifying what should happen at each step of

the simulation. The Biased RDP Physics class is used to implement biasing techniques in GEANT4 simulations, which are designed to accelerate the calculation of rare events or reduce the variance of important observables. In particular, it allows for the use of weight windows, which are a technique for biasing the sampling of the scattering process by selectively accepting or rejecting events based on their weight. In our simulation, this class has been added in order for GEANT4 to work also with the processes added in the input file, created with Mathematica as explained in sec. 3.5. Otherwise the simulation would work only with its own "RadioactiveDecay" database. The Detector Construction in Geant4 is responsible for defining the geometry of the detector and specifying the materials that make up the detector components. In our simulation the detectors defined are five HPGe, five BGO and a scintillator, disposed in the geometry described in Chapter 2. The Event Action is a user-defined class that is responsible for defining the actions to be taken at the end of each event during a simulation. Where an "event" is defined as the simulation of one or more particles passing through the detector and the subsequent interactions that occur. In particular, in the "EventAction" we define the correct timing for the events, for the species implanted it considers a delay which is the implantation time, divided by the evaluated number of events for the implantation. For subsequent species it also add an additional exponential delay which depends on the decay rate of the first implanted species. These values are stored in an additional file called "mssetup.hh", in our case it holds the informations for the implanted species ^{148}Cs and the isotopes produced through β neutron delayed: ^{147}Ba and ^{147}La. In addition in the file are also present the beam current in pps for the implantations, the transport and measuring time windows found in the previous mathematica codes. The Histo Manager is another user-defined class responsible for managing the creation and filling of histograms during a simulation. In our case, it fills histograms with the energy distribution of

all the possile particle emitted, along with the histograms of the detectors in use. The Primary Generator Action is also user-defined and generates the primary particles, outside of the detector, and then travel through the detector. The primary particles are typically generated according to some pre-defined distribution or user-specified parameters. The PhysicsList class is used to define the set of physics processes that are used to simulate the interaction of particles with matter. It is responsible for managing the initialization, creation, and deletion of all the particles, physics processes, and associated data that are used in a simulation. The physics processes we have used are: the radioactive decay, hadronic inelastic physics, the ion elastic scattering and the ion inelastic physics, as well as the Gamma nuclear physic process. In the Run Action class the user defines the actions to be taken at the beginning and end of a run. The Stepping Action controls the actions to be taken at each step of a particle in the detector, which is the segment of the particle's trajectory between two points where it undergoes a change in its state, such as a change in energy or direction. Here are also defined the energy resolution for the detectors, we have used a resolution of 15.8 % [35] for the scintillator, 22 % for the BGO, in accordance with previous measurements and tests of the detector, while for the HPGe we have used eq. 3.13. The Tracking Action is a user-defined class that is responsible for defining the actions to be taken when a particle is created, enters or leaves the world volume, or is destroyed. The TrackingAction class can be used to define a wide range of actions that should be taken during the tracking of particles, depending on the specific needs of the user. For example, the user might want to modify the properties of a particle before it is tracked, such as by adding some random fluctuations to its energy, or they might want to retrieve some information about the final position or energy of a particle after it has been tracked. In our case we have not used this class.

In total we have simulated three processes, the radioactive decay of ^{148}Cs,

^{147}La and ^{147}Ba. This was done because, as already explained, GEANT4 only takes account β decays along the same mass, so β-delayed neutrons are not considered. We have added only the masses ^{147}La and ^{147}Ba because the others decay present in Fig. 3.3 happens with too low branching ratios so do not affect the measurement. In fact, the branching ratio for β-delayed of ^{148}Cs is 25% and for ^{148}Ba is 0.4%. However the β-delayed neutron decay of ^{147}La and ^{147}Ba have branching ratios 0.04% and 0.06% respectively. The isotope ^{148}La instead decays β delayed neutron with 0.15%. Fig. 3.14 shows the resulting spectra obtained from the simulation, the top left panel is the sum of all the simulation processes of ^{148}Cs, ^{147}Ba and ^{147}La, the top right shows the result from ^{148}Cs, while the two on the bottom are ^{147}Ba (left) and ^{147}La (right). The spectrum of ^{147}La has few counts, but this is consistent with its relatively long half life (4.06 s) which results in few decay events during our measuring time window.

Fig. 3.15 shows the matrices resulting from the simulations. The matrix in the upper panel is the energy/time matrix of the GTC, while in the bottom is the coincidence between the GTC and the scintillator. The coincidence matrix shows a clear separation between the γ and β events.

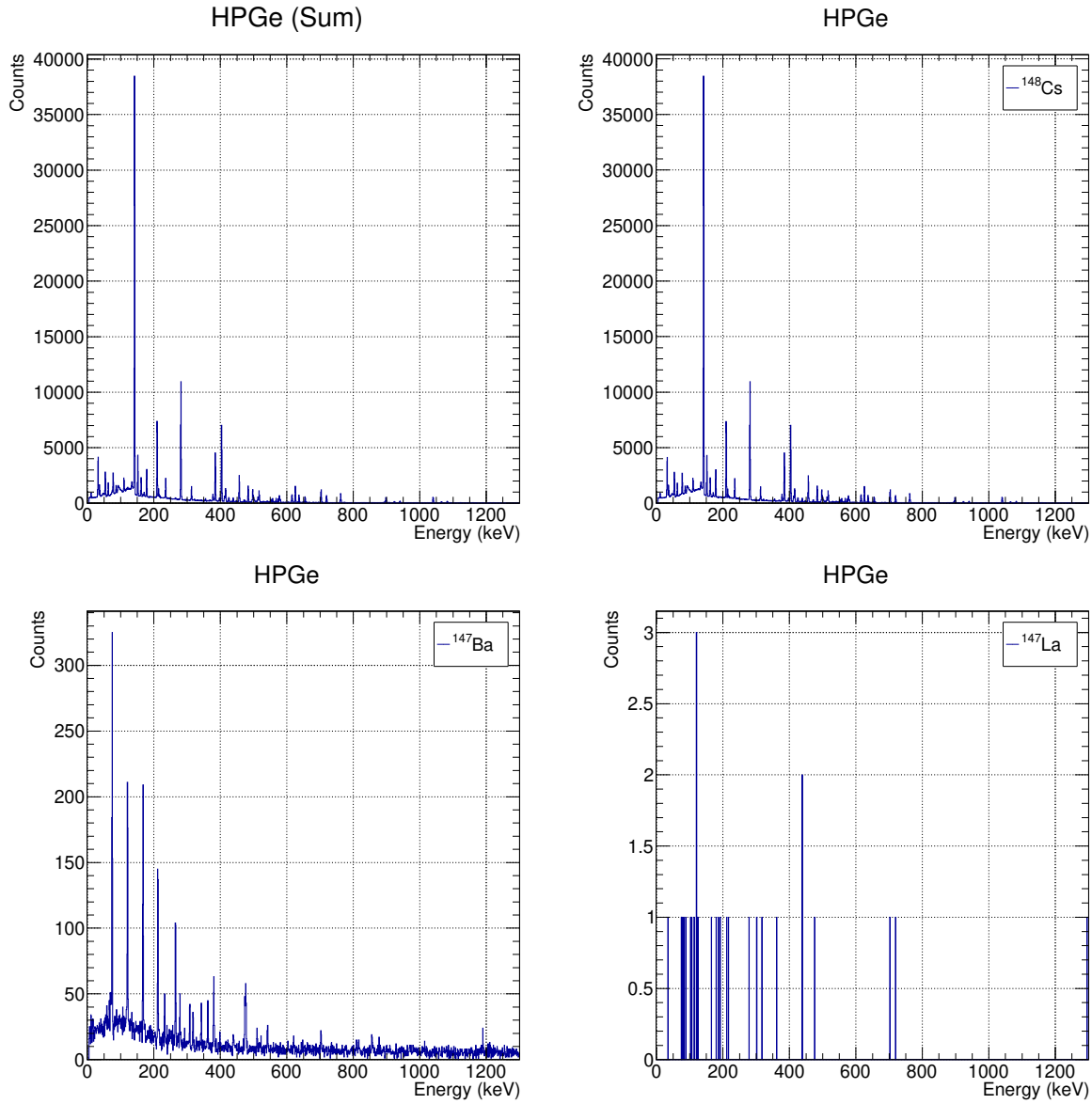

FIGURE 3.14: Resulting spectra obtained from the simulation, the top left panel is the sum of all the simulation processes of ^{148}Cs, ^{147}Ba and ^{147}La, the top right shows the result from ^{148}Cs, while the two on the bottom are ^{147}Ba (left) and ^{147}La (right).

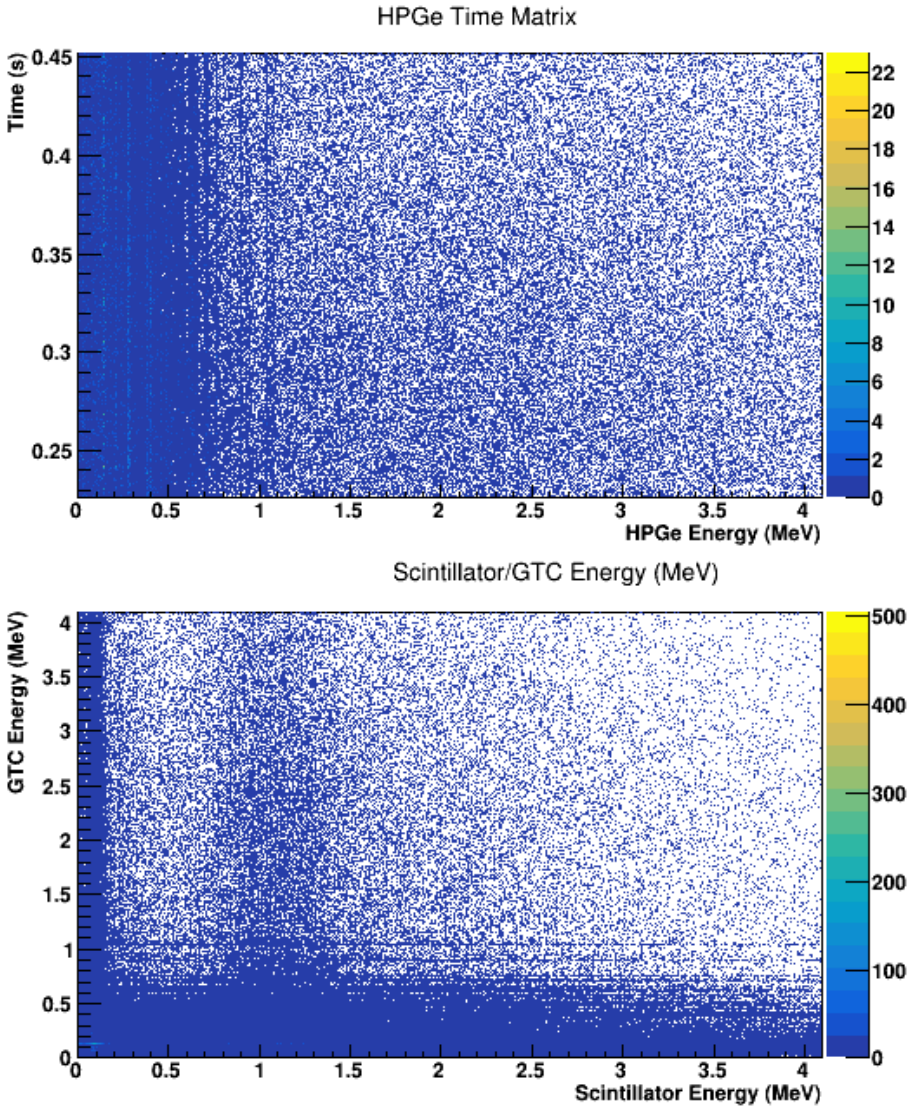

FIGURE 3.15: The matrix in the upper panel is the GTC energy/time matrix, while the one in the lower panel shows the coincidence between the plastic scintillator and the GTC. Based on the figure, it appears that the system is capable of distinguishing between Compton γ and electron events detected by the scintillator. This means that we can use energy cuts in the scintillator to separate gamma events resulting from beta decay from those caused by long-lived isotopes that have built up in the tape station.

Chapter 4

Conclusions

In this thesis work we have studied the capabilities of the β-decay station to be installed at LNL through a GEANT4 simulation. The simulations of experimental setups are a valuable tool for assessing the feasibility of actual measurements and are helpful in the analysis of experimental data. Two challenges exist in achieving accurate simulations: firstly, the GEANT4 radioactive decay process does not account for β decays accompanied by delayed neutron emissions, which are prevalent in neutron-rich nuclei. Secondly, the GEANT4 database may lack current decay information on rare nuclear species. We have created four Mathematica software programs specifically designed to collect all the essential nuclear decay information needed for a thorough simulation. Once a radioactive species is applied to the tape, the measuring cycle outlined in section 3.4 commences. At this phase, it's critical to maximize the efficiency of the irradiation and measurement time frames to guarantee a favorable measurement outcome. The second software's objective is to determine the most optimal measurement and irradiation duration, taking into account the tape's movement time. The third program accounts for β delayed neutron decay and generates a input file with the correct temporization. The last code performs two key functions: firstly, it updates the GEANT4 databases for PhotonEvaporation and NuclearDecay by incorporating the latest information sourced from the NNDC databases; secondly, it is equipped to compute the conversion coefficients if some of the details

pertaining to a given transition cannot be located. The softwares have been tested in the case of ^{148}Cs and the results have been used to produce the simulation. An initial efficiency simulation revealed that the detection system should be able to provide a good separation between γ compton and β events, with the possibility to definitely select β events with a threshold of 500 keV, in the case of ^{148}Cs. A second efficiency simulation as been carried out using prompt sources at various energies and in different detector configurations. In total we have tried three configuration for the GTC, specifically: (1) the five GTC crystals after the add-back procedure, (2) the same as (1) in anticoincidence with BGO shields and (3) the same as (1) in coincidence with the scintillators. The highest efficiency was of 3.5% for an energy of 1332 keV in the case of (1). Finally we have done a complete simulation of the system with the decay of the ^{148}Cs isotope, the spectra obtained seems to accurately reproduce the real case. Furthermore the comparison between the spectrum obtained with the old GEANT4 database and the one with the updated information seems to confirm the robustness of the method. The new spectrum retains all the old γ lines, and additionally includes lines from transitions that are not typically considered by GEANT4.

The β decay station is set to start its first measurements in SPES in five years. In the foreseeable future scintillator arrays will be added to perform neutron measurements in order to have a more comprehensive view of the decaying isotopes.

Appendix A

A New ASIC Based Front End for γ Energy Acquisition

A.1 Introduction

The study of nuclear physics and its diverse implementations in sectors such as industry, healthcare, academia, and practical research, necessitates the development of novel readout technology capable of handling a large number of acquisition channels. Application Specific Integrated Circuit (ASIC) chips are a great option to fulfill this requirement, as it enables the integration of intricate circuits within a compact device while consuming minimal power.

We utilized the CAEN A5202 FERS-5200 board [36], incorporating two Citiroc 1A ASIC chips developed by Weeroc [37] to perform several energy acquisitions, in order to test the feasibility of performing γ spectroscopy. The selection of this board was based on its large acquisition channels capacity (64 channels, with 32channels per chip), while still allowing for easy scalability to accommodate hundreds of channels by synchronizing several boards through optical links

The performance of the Citiroc 1A chip has been extensively studied and characterized in previous works, including evaluations of trigger efficiency, linearity, temperature response, and optical cross talk [38]. Its durability and

adaptability makes the Citiroc 1A chip suitable for a wide range of applications. For instance, it has been employed in cosmic ray measurements [39], anti-coincidence gamma measurements for astrophysics [40], X and γ-ray detectors for space missions [41], wearable Positron Emission Tomography (PET) in medical applications [42], and high-density channel Pulse Shape Discrimination (PSD) measurements [43].

Furthermore the board single-photon caunting capabilities have been examined in various applications, such as high granular calorimetry for high-energy physics, multi-channel dosimetry for brachytherapy [44], and radioactive waste monitoring [45]. Characterization and preliminary cosmic ray measurements using the A5202 board instead have been reported in [36] and [46], respectively.

In particular we have explored the possibility of employing the Citiroc 1A chip to acquire γ energy spectra from scintillator detectors with relatively slow light decay times comparable to or longer than the shaping time of the chip [1]. Severeal energy measurements have been peformed with three scintillator crystals, namely LYSO, Caesium Iodine (CsI(Tl)), and Bismuth Germanate (BGO), with respective decay times of 40 ns, 1000 ns, and 300 ns.

While the Citiroc 1A chip has a maximum shaping time of 87.5 ns, which theoretically might only be suitable for the LYSO detector, satisfactory energy resolutions were achieved for all three detectors. The obtained energy spectra from three γ radioactive sources emplyed (^{22}Na, ^{60}Co, and ^{137}Cs) exhibited resolutions consistent with expectations from existing literature [47] [48] [**res2**] [49] and were comparable to those obtained using an alternative system employing a digitizer with a charge integration algorithm as the acquisition system [50].

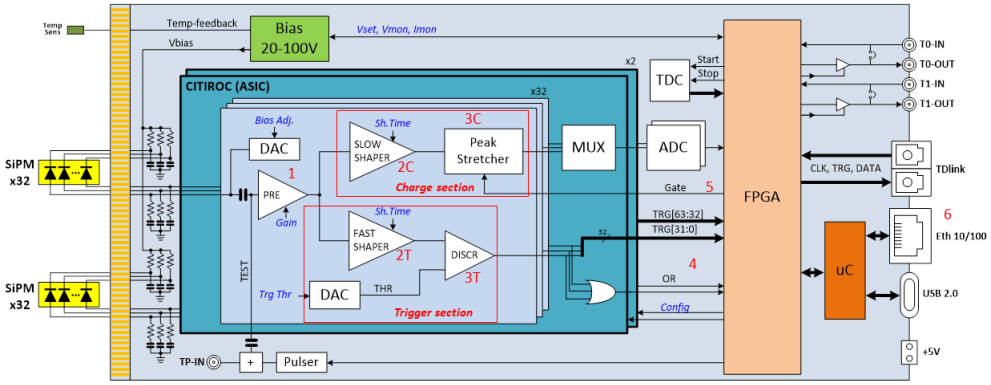

FIGURE A.1: Scheme of A5202 board. The boards is composed by two Citiroc 1A chips (petrol green boxes), a power supply (green box) that feed the bias voltage to the SiPM, an FPGA (light orange box), and general purpose I/Os.

A.2 Front-End Electronic Structure

The A5202 board, shown in Fig. A.1, is an all in one SiPM readout system. It integrates two Citiroc 1A chips (highlighted as petrol green boxes in the figure), providing a total of sixty-four acquisition channels. The board also includes a power supply module (green box) to feed the bias volatage to the SiPMs, an FPGA (light orange box), multiple communication interfaces (USB, Ethernet, and optical link), and general-purpose I/Os.

Furthermore, individual channels DACs are present in the Citiroc 1A chips and allow for precise channel-by-channel voltage tuning, while a temperature feedback circuit compensates for temperature variations.

The A5202 performs γ spectroscopy through a pulse height analysis (PHA) algorithm. This algorithm evaluates the energy deposited in the detector by measuring the height of the output pulse generated by the detector. The Citiroc 1A chip acquisition line consists of a preamplifier (labeled as "1" in the figure), along with two main sections: the charge measurement section (labeled as "Charge section" in the figure) and the time measurement section (labeled as "Trigger section" in the figure). The preamplifier offers two gain options, a high gain (HG) and a lower gain (LG), to cover a wide dynamic range of pulse amplitudes. Individual preamplifiers can be selectively shut

down to isolate potentially noisy channels.

The trigger section comprises a fast shaper (2T) with a fixed peaking time of 15 ns and a discriminator (3T). The output of the discriminator is sent to the FPGA of the A5202 board. The trigger signals from individual channels, as well as the logic OR combination line (labeled as "4"), can be propagated to the FPGA. Although the chip includes an additional discriminator, it is not utilized in this particular study.

The charge measurement section employs a slow CR-RC^2 shaper (2C) and a peak-and-hold circuit (3C). The shaping time of 2C can be adjusted between a minimum of 12.5 ns and a maximum of 87.5 ns, with a 12.5 ns increment. This shaping time is common to all channels but can be distinguished between the low gain and high gain portions of the Citiroc 1A chip.

The pulse height analys Fig. A.2 illustrates the operational principle of the peak sensing mechanism. This functionality is performed by the peak and hold circuit, denoted as 3C in Fig. A.1. The peak and hold circuit operates in three distinct phases:

- OFF Phase: Prior to the arrival of the trigger signal, the peak and hold circuit remains inactive.

- Peak Sensing Phase: When the trigger signal is received from the FPGA (labeled as 5), the peak detector is activated and records the maximum value of the input signal. This phase is held until a rising edge of the hold signal is detected.

- Hold Phase: In this phase, the peak and hold circuit is disconnected from the slow shaper to prevent any further values from being stored. The hold phase is utilized during the serial read-out of the ASIC. The duration between the trigger and the hold phase is referred to as the "Hold Delay." This value is tunable by the user and has been optimized in Section A.4. After the hold phase the peak detector goas back to the

OFF phase, so another cycle can begin upon the arrival of a new trigger signal

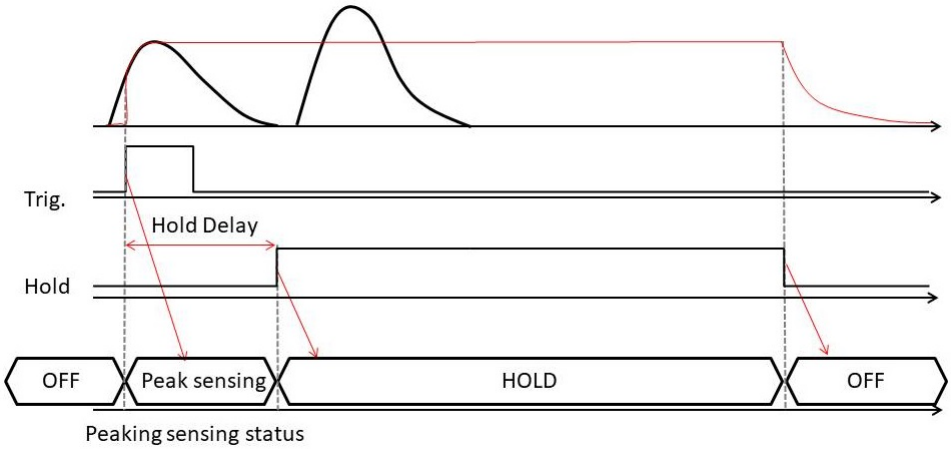

FIGURE A.2: Citiroc 1A peak sensing working principle. Once the trigger signal is issued, the system switches to the peak sensing phase and finds the peak on the incoming pulse. Upon the arrival of the hold signal the system goes to the "hold" phase in which it disconnects to the shaper to avoid any other pulse entering the system and invalidate the measure. At the arrival of the hold signal falling edge, the "OFF" phase starts and the cycle begins again upon the arrival of a new trigger.

A.3 Experimental Setup

Two different experimental setups were utilized for the measurements. The first setup (I) aimed to validate the acquisition of energy spectra using a single crystal coupled with a SiPM, while the second setup (II) employed different hardware to confirm the consistency of the results obtained in setup I.

Setup I involved the use of three scintillator crystals, specifically CsI(Tl), LYSO, and BGO, obtained from Hilger Crystals LTD [51]. These crystals had dimensions of $6 \times 6 \times 15$ mm^3 and were coupled with optical grease. Each crystal was coupled with a Hamamatsu SiPM MPPC S13360-6050CS [52], which was a single-channel SiPM with an effective photosensitive area of

6×6 mm^2 and a pixel size of 50 μm. The SiPM operated at a voltage of 53.8 V, and all measurements were conducted at room temperature. To connect the detectors and SiPMs to the A5202 board, the A5253 adapter [53] was utilized.

We have performed energy acquisitions with one channel active at a time using three radioactive sources: ^{22}Na, ^{137}Cs, and ^{60}Co with activities of approximately 87 kBq, 7 kBq, and 12 kBq, respectively. The top panel of Fig. A.3 displays an image of the first experimental setup, while the bottom panel labels a single SiPM and LYSO detector as (A) and (B), respectively.

The CAEN Janus software [54] was employed to control the acquisition settings, plot the spectra, and save the acquired data.

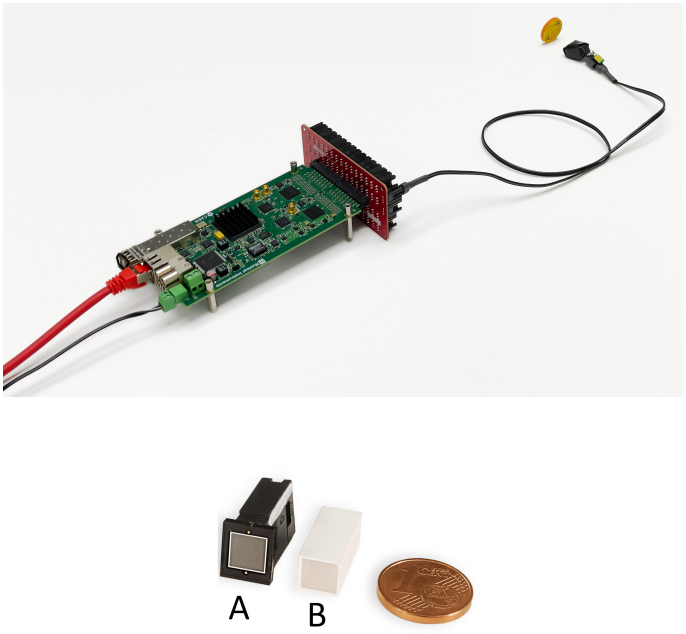

FIGURE A.3: The top panel shows a picture of setup I, whith the A5202 board connected through the A5253 adapter to a single SiPM coupled with a LYSO crystal, and a ^{22}Na radioactive source. The bottom panel shows the 6×6 mm^2 SiPM used used marked by the letter (A), while (B) is the single LYSO detector. The one cent euro coin is added a raference for scale.

In setup II, we utilized the CAEN SP5600 amplification unit [55] and the DT5720A desktop digitizer [50]. The SP5600 served as the power supply for

the SiPM and provided the preamplification stage. On the other hand, the DT5720A is a digitizer with a sampling time of 4 ns and a 12-bit ADC.

The DT5720A performs energy acquisition through a charge integration algorithm [56] which is particular suitable for processing signals with longer decay times, such as those from CsI(Tl) and BGO. The DT5720A samples the incoming signal and sum the content of the samples contained in a gate time window, defined by the user, that encompass the entirety of the signal.

To ensure the quality of the measurements obtained with the A5202, all the acquisitions performed with the DT5720A where carried out with the same SiPM and crystals used with the A5202

A.4 Event Selection

We have first conducted several tests to verify the Citiroc 1Acorrect processing of the events. The chip offers monitoring signals, including the output of the slow shaper (2C) and the output of the preamplifier (1), which can be propagated to one of the output connectors of the A5202 and displayed on an oscilloscope. In Figure A.4, the top panel displays the output of the trigger discriminator (3T) in blue and the output of the slow shaper in red.

The shape of the red pulse is influenced by the chosen shaping time (87.5 ns in this instance). The positive component of the red pulse remains consistent across all crystals, while the pole-zero compensation varies depending on the tail of the input pulse. The bipolar shape is an expected characteristic of the Citiroc 1A shaper amplifier circuit. However, for energy calculation purposes, only the positive part of the pulse is considered.

To determine the optimal shaping time for our measurements, we conducted a scan of the available shaping time values. Taking into account the decay times of the three crystals (LYSO with 40 ns, BGO with 300 ns, and

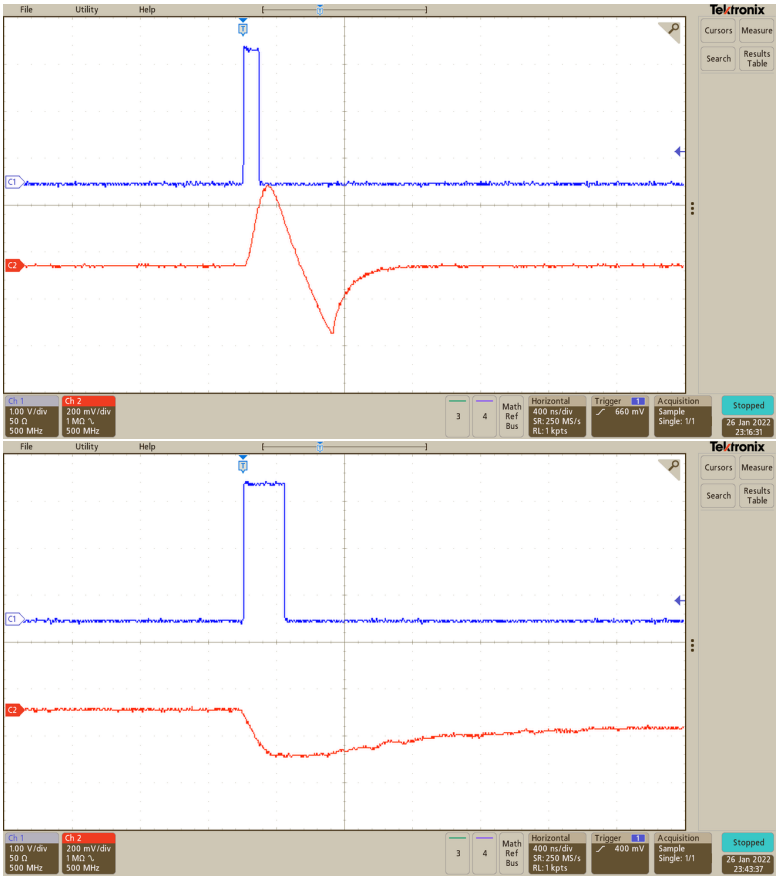

FIGURE A.4: On the top panel, the outputs of the trigger discriminator (blue) and of the slow shaper (red) in case of the LYSO detector, with a shaping time of 87.5 ns. The red pulse in the bottom panel is the output of the preamplifier with the CsI(Tl) detector.

CsI(Tl) with 1000 ns) and the shaping time range of the Citiroc 1A (12.5 ns to 87.5 ns).

We collected the ^{22}Na energy spectrum using the LYSO detector for each allowed shaping time value. As the shaping time increased, we observed a shift of the spectra towards higher energy values. This phenomenon can be attributed to a reduction in charge collection when using smaller shaping times. Since the light decay time of the LYSO crystal is 40 ns, smaller shaping times result in the slow shaper capturing only a portion of the signal. Consequently, the output amplitude of the shaper is diminished. The spectra, along with the resolution (R) of the 511 keV annihilation peak, are presented in Fig. A.5. The resolution is calculated as the Full Width Half

Maximum (FWHM) of the peak divided by the mean value of the peak obtained through a Gaussian fit, with background subtraction performed using a polynomial function.

For shaping times higher than 50 ns (exceeding the 40 ns decay time of LYSO), the resolution at 511 keV stabilizes at around 9.5-9.6%. Based on these results, and considering that the other crystals have longer decay times, we decided to use the shaping time of 87.5 ns for CsI(Tl) and BGO without conducting further scans. Although only a portion of the pulse is captured in the case of CsI(Tl)and BGO, this portion is still proportional to the total pulse energy.

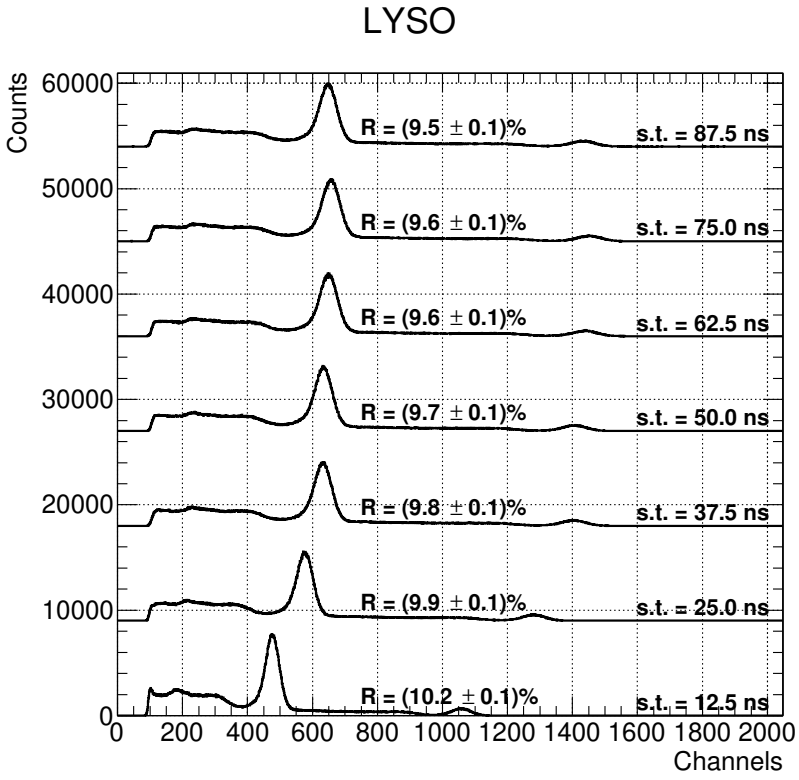

FIGURE A.5: ^{22}Na energy spectra acquired with the LYSO detector by varying the shaping time (s.t. in the figure). When the shaping time is less than 40 ns, the system collects only a portion of the signal generated by the LYSO crystal, while for larger shaping times all the signal is collected and the 511 keV annihilation peak resolution stabilizes around 9.5%-9.6% .

Another setting that needs to be optimized is the "hold delay," which

refers to the time difference between the trigger signal and the arrival of the hold signal (as shown in Fig. A.2). This parameter is crucial because it determines the time interval in which the peak of the slow shaper output should arrive, for its maximum to be accurately evaluated. If the hold signal arrives too early, the peak sensing mechanism captures only a portion of the pulse, leading to incorrect results.

To optimize the hold delay parameter, we conducted additional measurements of the ^{22}Na energy spectrum using the LYSO crystal and a single 6×6 mm^2 SiPM. We set the shaping time to the optimized value of 87.5 ns and varied the hold delay from 50 ns to 350 ns. For each spectrum, we determined the position of the 511 keV peak and plotted this value against the corresponding hold delay, as shown in Fig. A.6.

We observed that the peak position stabilizes at approximately 200 ns of hold delay, indicating that after this time threshold, the peak sensing mechanism can accurately evaluate the maximum height of the pulse. However, for hold delay values below 200 ns, the energy is underestimated. Based on these findings, we chose a hold delay value of 300 ns for the measurements described in this paper, ensuring that the peak sensing mechanism can reliably capture the maximum pulse height.

A.5 Results

The results obtained from setups I and II all shows the characteristic energy spectra for the three gamma radioactive sources used in this paper: ^{22}Na, ^{137}Cs, and ^{60}Co. Fig. A.7 and Fig. A.8 display the spectra acquired with the LYSO, CsI(Tl), and BGO detectors (from top to bottom) and the ^{22}Na, ^{137}Cs, and ^{60}Co sources (from left to right) for setups I and II, respectively.

Tab. A.1 presents the resolutions and statistical uncertainties of the four peaks (511 keV for ^{22}Na, 662 keV for ^{137}Cs, and 1172 keV and 1332 keV for

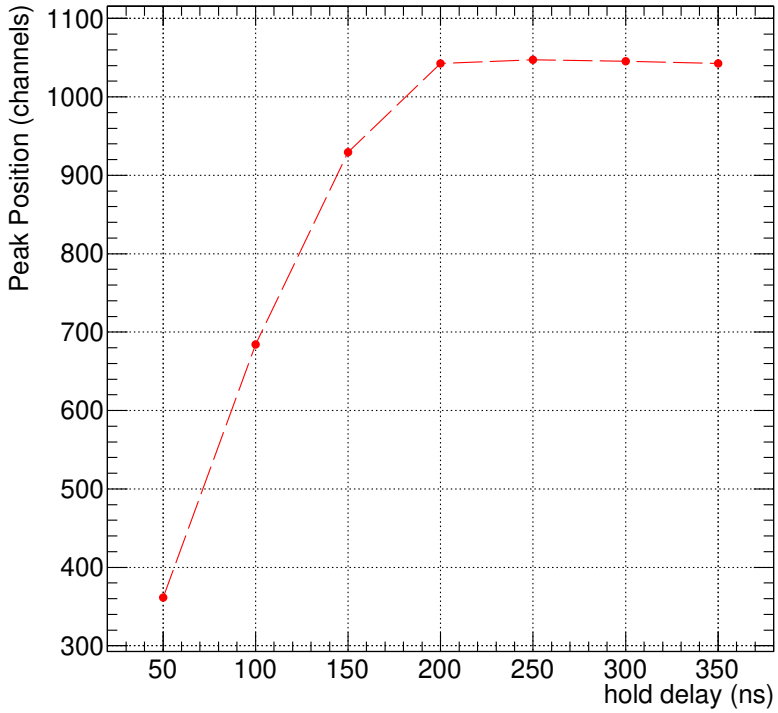

FIGURE A.6: Position of the ^{22}Na annihilation peak, in channels, as a function of the hold delay parameter. The measurements have been performed with the LYSO crystal.

^{60}Co) for both setup I and II. Corrections for SiPM saturation were not considered since this contribution will cancel out in the comparison between setups I and II. However, it is worth noting that according to the linearity curve calculated from [57], SiPM saturation will primarily affect the peaks of the ^{60}Co source, which have higher energy. For energy values below those peaks, the SiPM operates in the linear region and is less impacted by saturation effects.

Comparing the results presented in Table A.1 and the plots in Fig. A.7 and A.8 between setups I and II, we find that compatible results were obtained for both systems.

The LYSO crystal exhibits its own gamma radioactivity, resulting in a prominent background in the energy region of the 662 keV peak of ^{137}Cs (2 in Fig. A.7 and A.8). This effect is not visible for the ^{22}Na source, despite the 511 keV annihilation peak being close to the energy emission of LYSO,

TABLE A.1: Resolutions Obtained with A5202 FERS-5200 Board (Setup I) and with the DT5720A Desktop Digitizer (Setup II).

	^{22}Na (511 KeV)	^{137}Cs (662 KeV)
A5202+LYSO (I)	(9.5 ± 0.1)%	(9.3 ± 0.1)%
DT5720A+LYSO (II)	(12.3 ± 0.1)%	(10.3 ± 0.1)%
A5202+CsI(Tl) (I)	(11.9 ± 0.1)%	(10.9 ± 0.1)%
DT5720A+CsI(Tl) (II)	(9.6 ± 0.1)%	(8.9 ± 0.1) %
A5202+BGO (I)	(14.4 ± 0.1)%	(13.5 ± 0.1)%
DT5720A+BGO (II)	(12.0 ± 0.1)%	(11.0 ± 0.1)%
	^{60}Co (1172 KeV)	^{60}Co (1332 KeV)
A5202+LYSO (I)	(5.8 ± 0.1)%	(5.0 ± 0.1)%
DT5720A+LYSO (II)	(6.3 ± 0.4)%	(5.4 ± 0.2)%
A5202+CsI(Tl) (I)	(5.8 ± 0.2)%	(5.6 ± 0.1)%
DT5720A+CsI(Tl) (II)	(5.6 ± 0.2)%	(5.4 ± 0.1)%
A5202+BGO (I)	(8.7 ± 0.1)%	(7.1 ± 0.1)%
DT5720A+BGO (II)	(7.7 ± 0.3)%	(6.8 ± 0.4)%

because the source activity was high enough to overcome the background.

Compton background is more pronounced, especially in the case of the CsI(Tl) crystal (plots 4, 5, and 6), due to the reduced dimensions of the crystals. Nevertheless, the characteristic peaks are clearly visible for all sources and detectors.

Regarding the LYSO crystal (plots 1, 2, and 3 in Figures A.7 and A.8), the resolution obtained with setup I is better by about 20-30% compared to the more traditional setup II.

For the CsI(Tl) and BGO detectors, measurements from setup II and the literature [**res2**, 47] exhibit better resolutions by a factor of approximately 20%, although the order of magnitude of the resolutions for the ^{60}Co source remains the same. This discrepancy is expected, as the maximum shaping time of 87.5 ns in setup I is too short to capture the full amplitude of the CsI(Tl) and BGO signals, which are better integrated with the charge integration algorithm. Saturation effects also limit the resolution and peak separation for the ^{60}Co peaks.

In conclusion, we have successfully explored the possibility of performing nuclear spectroscopy measurements using scintillator detectors coupled

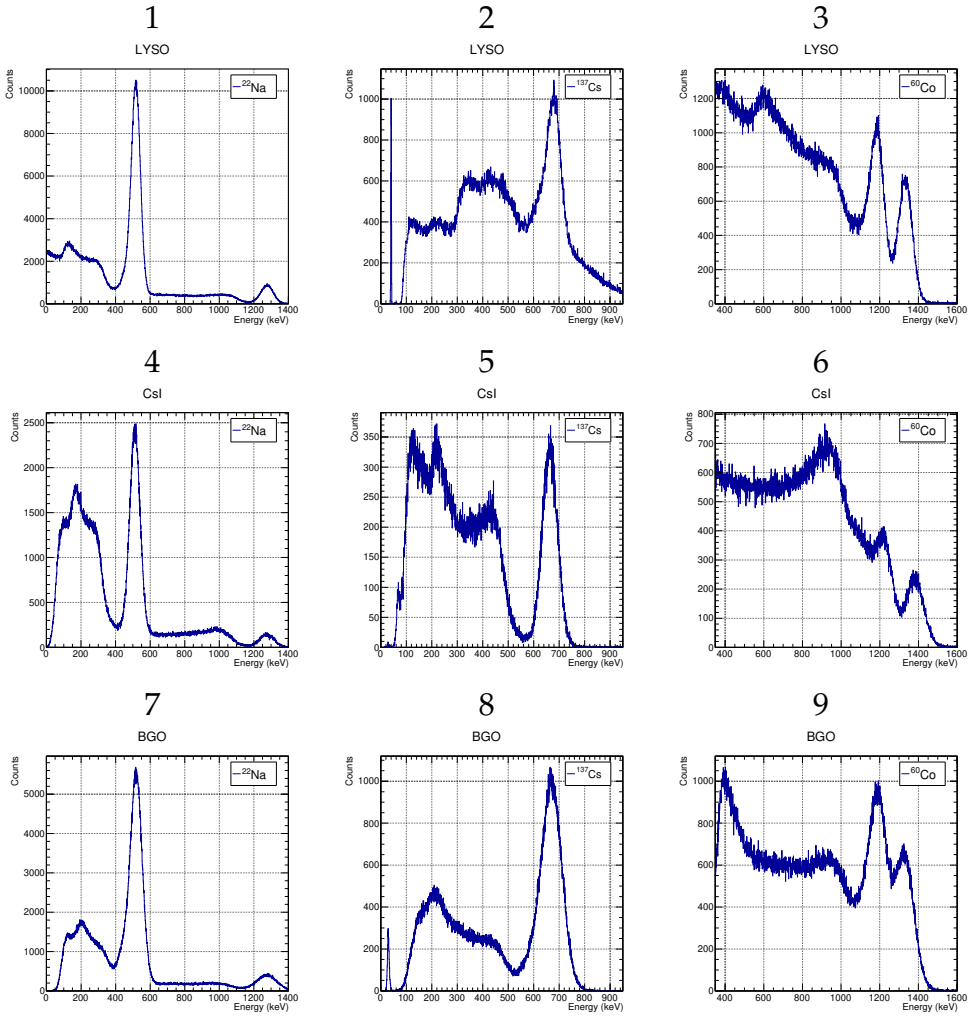

FIGURE A.7: Calibrated energy spectra from ^{22}Na, ^{137}Cs, and ^{60}Co γ radioactive sources (from left to right) measured with LYSO, CsI(Tl), and BGO crystals (from top to bottom) coupled with single 6×6 mm^2 SiPMs and acquired with the A5202 board.

with SiPMs, acquiring radiation from three different gamma sources with the Citiroc 1A chip integrated into the A5202 board. The A5202 proves to be a suitable candidate for SiPM-based γ spectroscopy applications requiring high channel density, as it provides comparable resolutions for slower detectors like CsI(Tl) and BGO.

Future measurements can further exploits the capabilities of this readout system in conjunction with scintillator crystals with faster decay times, such as $LaBr_3$ or $CeBr_3$, and with larger dimensions, to explore their performance

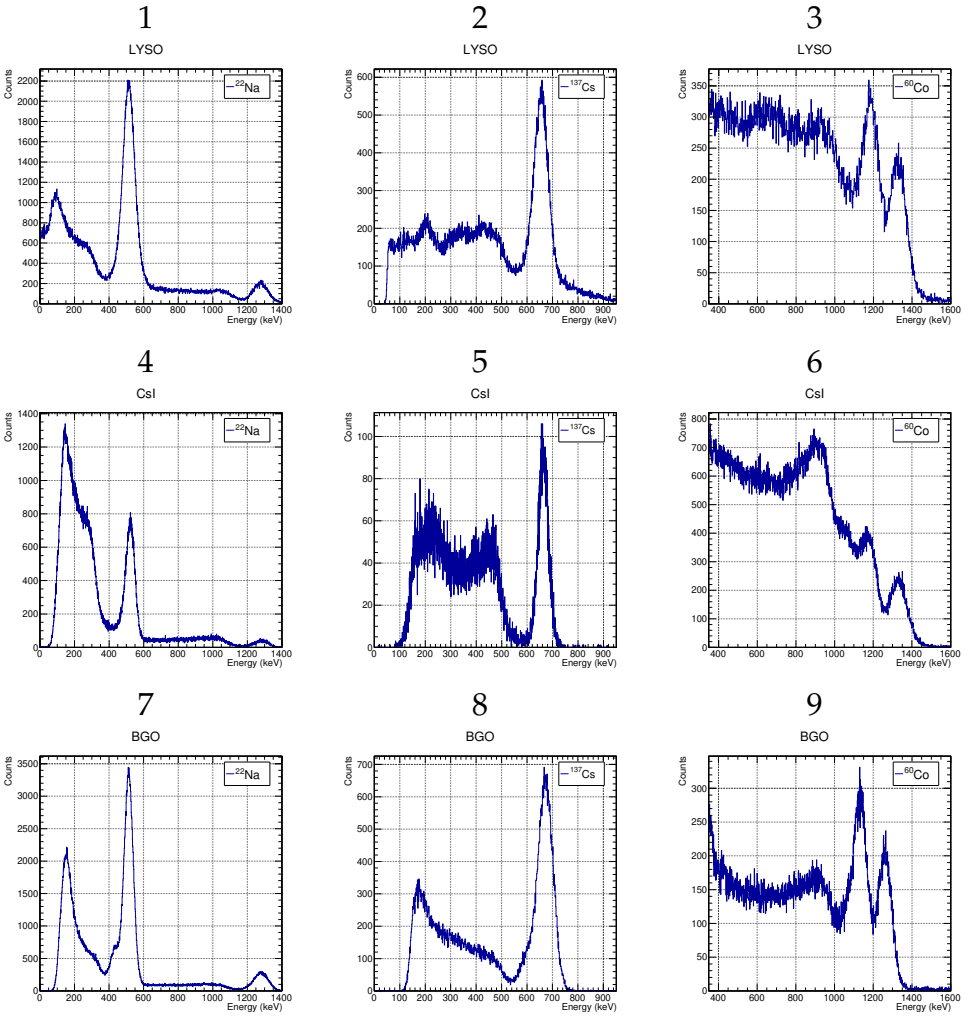

FIGURE A.8: Calibrated energy spectra from ^{22}Na, ^{137}Cs, and ^{60}Co γ radioactive sources (from left to right) measured with LYSO, CsI(Tl), and BGO crystals (from top to bottom) coupled with single 6×6 mm^2 SiPMs and acquired with the DT5720A board.

in gamma spectroscopy applications.

Bibliography

[1] M. Perri et al. "Amplitude Measurements with SiPM and ASIC (Citiroc 1A) Front-End Electronics". In: *IEEE Transactions on Nuclear Science* (2023), pp. 1–1. DOI: 10.1109/TNS.2023.3262409.

[2] Kenneth S. Krane. *INTRODUCTORY NUCLEAR PHYSICS*. John Wiley & Sons Inc., 1987.

[3] A. Andrighetto et al. "The SPES High Power ISOL production target". In: *Nuovo Cimento della Societa Italiana di Fisica C* 38 (Jan. 2015). DOI: 10.1393/ncc/i2015-15194-x.

[4] B. Rubio and W. Gelletly. "Beta Decay of Exotic Nuclei". In: *The Euroschool Lectures on Physics with Exotic Beams, Vol. III*. Ed. by J.S. Al-Khalili and E. Roeckl. Berlin, Heidelberg: Springer Berlin Heidelberg, 2009, pp. 99–151. ISBN: 978-3-540-85839-3. DOI: 10.1007/978-3-540-85839-3_4. URL: https://doi.org/10.1007/978-3-540-85839-3_4.

[5] H Bateman. "The solution of a system of differential equations occurring in the theory of radioactive transformations". In: *Proceedings of the Cambridge Philosophical Society, Mathematical and physical sciences.* 15 (1910). URL: https://archive.org/details/cbarchive_122715_solutionofasystemofdifferentia1843.

[6] O.I. Batenkov et al. "Study of the mechanism of Cf-252 spontaneous fission neutron emission". In: 1987.

[7] Oleg Batenkov et al. "Comparison of Measured and Calculated Mass Distributions of Fission Fragments in Proton-Induced Fission of ^{232}Th,

^{235}U, ^{238}U, and^{237}Np at Intermediate Energies". In: *AIP Conference Proceedings* 769 (Apr. 2005), p. 625. DOI: 10.1063/1.1945087.

[8] K F Eckerman et al. "Availability of nuclear decay data in electronic form, including beta spectra not previously published". In: *Health Physics* 67.4 (Oct. 1994). DOI: 10.1097/00004032-199410000-00004. URL: https://www.osti.gov/biblio/54455.

[9] T W Burrows. "The program RADLST (Radiation Listing)". In: (Feb. 1988). DOI: 10.2172/6838683. URL: https://www.osti.gov/biblio/6838683.

[10] R. M. Thaler. "Nuclear Physics: Physics of the Nucleus. M. A. Preston. Addison-Wesley, Reading, Mass., 1962. x + 661 pp. Illus. $15." In: *Science* 137.3533 (1962), pp. 848–848. DOI: 10.1126/science.137.3533.848.a. eprint: https://www.science.org/doi/pdf/10.1126/science.137.3533.848.a. URL: https://www.science.org/doi/abs/10.1126/science.137.3533.848.a.

[11] J. C. Hardy et al. "The essential decay of pandemonium: A demonstration of errors in complex beta-decay schemes". In: *Physics Letters B* 71.2 (Nov. 1977), pp. 307–310. DOI: 10.1016/0370-2693(77)90223-4.

[12] A. Perego et al. "Neutrino-driven winds from neutron star merger remnants". In: *Monthly Notices of the Royal Astronomical Society* 443 (May 2014). DOI: 10.1093/mnras/stu1352.

[13] M. Maggiore et al. "SPES: A new cyclotron-based facility for research and applications with high-intensity beams". In: *Modern Physics Letters A* 32.17 (2017), p. 1740010. DOI: 10.1142/S0217732317400107. eprint: https://doi.org/10.1142/S0217732317400107. URL: https://doi.org/10.1142/S0217732317400107.

[14] T Marchi et al. "The SPES facility at Legnaro National Laboratories". In: *Journal of Physics: Conference Series* 1643.1 (Dec. 2020), p. 012036. DOI: 10.1088/1742-6596/1643/1/012036. URL: https://dx.doi.org/10.1088/1742-6596/1643/1/012036.

[15] A. Andrighetto et al. "The SPES multi-foil direct target". In: *Nuclear Instruments and Methods in Physics Research Section B: Beam Interactions with Materials and Atoms* 266.19 (2008). Proceedings of the XVth International Conference on Electromagnetic Isotope Separators and Techniques Related to their Applications, pp. 4257–4260. ISSN: 0168-583X. DOI: https://doi.org/10.1016/j.nimb.2008.05.134. URL: https://www.sciencedirect.com/science/article/pii/S0168583X08007155.

[16] Mattia Manzolaro et al. "THE SPES PROJECT: RESEARCH AND DEVELOPMENT FOR THE MULTI-FOIL DIRECT TARGET". In: (Mar. 2023).

[17] Michele Comunian et al. "Design of High Resolution Mass Spectrometer for SPES". In: *9th International Particle Accelerator Conference*. June 2018. DOI: 10.18429/JACoW-IPAC2018-THPAK021.

[18] A Galatà et al. "ADIGE: the radioactive ion beam injector of the SPES project". In: *Journal of Physics: Conference Series* 874.1 (July 2017), p. 012052. DOI: 10.1088/1742-6596/874/1/012052. URL: https://dx.doi.org/10.1088/1742-6596/874/1/012052.

[19] A Galatà et al. "Towards the first beams from the ADIGE injector for the SPES Project". In: *Journal of Physics: Conference Series* 1350.1 (Nov. 2019), p. 012090. DOI: 10.1088/1742-6596/1350/1/012090. URL: https://dx.doi.org/10.1088/1742-6596/1350/1/012090.

[20] Francesca Borgna et al. "Early Evaluation of Copper Radioisotope Production at ISOLPHARM". In: *Molecules* 23.10 (2018). ISSN: 1420-3049.

DOI: 10.3390/molecules23102437. URL: https://www.mdpi.com/1420-3049/23/10/2437.

[21] A. Andrighetto et al. "The ISOLPHARM project: A New ISOL production method of high specific activity beta-emitting radionuclides as radiopharmaceutical precursors". In: *International Journal of Modern Physics: Conference Series* 48 (2018), p. 1860103. DOI: 10.1142/S2010194518601035. eprint: https://doi.org/10.1142/S2010194518601035. URL: https://doi.org/10.1142/S2010194518601035.

[22] Juan Esposito et al. "LARAMED: A Laboratory for Radioisotopes of Medical Interest". In: *Molecules* 24.1 (2019). ISSN: 1420-3049. DOI: 10.3390/molecules24010020. URL: https://www.mdpi.com/1420-3049/24/1/20.

[23] Gaia Pupillo et al. "The Laramed project at LNL: 67Cu and 47Sc production for theranostic applications". In: *AIP Conference Proceedings* 2295.1 (2020), p. 020001. DOI: 10.1063/5.0032898. eprint: https://aip.scitation.org/doi/pdf/10.1063/5.0032898. URL: https://aip.scitation.org/doi/abs/10.1063/5.0032898.

[24] L. Silvestrin et al. "SPES and the neutron facilities at Laboratori Nazionali di Legnaro". In: *European Physical Journal Plus* 131, 72 (Mar. 2016), p. 72. DOI: 10.1140/epjp/i2016-16072-0.

[25] Pierfrancesco Mastinu et al. "Fast neutrons at LNL Legnaro". In: *Journal of Neutron Research* (Oct. 2020), pp. 1–15. DOI: 10.3233/JNR-200156.

[26] Dario Bisello et al. "Neutron production targets for a new Single Event Effects facility at the 70 MeV Cyclotron of LNL-INFN". In: *Physics Procedia* 26 (Dec. 2012), p. 284. DOI: 10.1016/j.phpro.2012.03.036.

[27] Fabiana Gramegna and G. Prete. "The SPES Exotic Beam ISOL Facility: Status of the Project, Technical Challenges, Instrumentation, Scientific Program". In: *Nucleus* (June 2018), pp. 48–52.

[28] Alberto Monetti et al. "The RIB production target for the SPES project". In: *The European Physical Journal A* 51 (Oct. 2015). DOI: 10.1140/epja/i2015-15128-6.

[29] A. Goasduff et al. "The GALILEO γ-ray array at the Legnaro National Laboratories". In: *Nuclear Instruments and Methods in Physics Research Section A: Accelerators, Spectrometers, Detectors and Associated Equipment* 1015 (2021), p. 165753. ISSN: 0168-9002. DOI: https://doi.org/10.1016/j.nima.2021.165753. URL: https://www.sciencedirect.com/science/article/pii/S0168900221007385.

[30] N. Marchini et al. "SLICES: Spes Low-energy Internal Conversion Electron Spectrometer". In: *Nuclear Instruments and Methods in Physics Research Section A: Accelerators, Spectrometers, Detectors and Associated Equipment* 1020 (2021), p. 165860. ISSN: 0168-9002. DOI: https://doi.org/10.1016/j.nima.2021.165860. URL: https://www.sciencedirect.com/science/article/pii/S0168900221008457.

[31] T. Krings et al. "Development and characterization of a detector system for electron spectroscopy measurements at the ISOL facility SPES". In: ().

[32] Maurizio Montis et al. "EPICS Based Control System for SPES Tape Station for Beam Characterization: Motion System and Controls". In: *17th International Conference on Accelerator and Large Experimental Physics Control Systems*. 2020, MOPHA097. DOI: 10.18429/JACoW-ICALEPCS2019-MOPHA097.

[33] Maurizio Montis et al. "EPICS BASED CONTROL SYSTEM FOR SPES TAPE STATION FOR BEAM CHARACTERIZATION: MOTION SYSTEM AND CONTROLS". In: Oct. 2019. DOI: 10.18429/JACoW-ICALEPCS2019-MOPHA097.

[34] J. Liang et al. "Compilation and Evaluation of Beta-Delayed Neutron Emission Probabilities and Half-Lives for Z > 28 Precursors". In: *Nuclear Data Sheets* 168 (2020), pp. 1–116. ISSN: 0090-3752. DOI: https://doi.org/10.1016/j.nds.2020.09.001. URL: https://www.sciencedirect.com/science/article/pii/S009037522030034X.

[35] Ngan TRAN et al. "Some Properties of Plastic Scintillators to Construct a LET Spectrometer". In: Jan. 2019. DOI: 10.7566/JPSCP.24.011008.

[36] "UM7945 - FERS-5200 A5202-DT5202 User Manual". In: *CAEN SpA, Viareggio(LU), Italy* (2021). URL: www.caen.it/products/a5202.

[37] "Citiroc 1A Scientific instrumentation SiPM read-out chip Data Sheet". In: *Weeroc, Villebon-sur-Yvette, France* (2021). URL: www.weeroc.com/en/products/citiroc-1.

[38] D. Impiombato et al. "Characterization and performance of the ASIC (CITIROC) front-end of the ASTRI camera". In: *Nuclear Instruments and Methods in Physics Research Section A: Accelerators, Spectrometers, Detectors and Associated Equipment* 794 (2020), pp. 85–192. DOI: https://doi.org/10.1016/j.nima.2015.05.028..

[39] Dimitrios Kyratzis et al. "The Plastic Scintillator Detector of the HERD space mission". In: July 2021, p. 054. DOI: 10.22323/1.395.0054.

[40] C. Kierans. "AMEGO: exploring the extreme multi-messenger universe". In: Dec. 2020, p. 320. DOI: 10.1117/12.2562352.

[41] F. Garufi et al. "The Crystal Eye X and gamma-ray detector for space missions". In: *Journal of Physics: Conference Series* 2429.1 (Feb. 2023), p. 012024. DOI: 10.1088/1742-6596/2429/1/012024. URL: https://dx.doi.org/10.1088/1742-6596/2429/1/012024.

[42] FJ. Allison et al. "Wearable Positron Emission Tomography, WPET". In: *Public deliverable for the ATTRACT Final Conference* (2020).

[43] M. Fang, S. Pani, and A. Di Fulvio. "Enabling PSD-capability for a High-density Channel Imager". In: *Abstract N-03-07 in 2021 IEEE NSS MIC Yokohama Japan*, (2021).

[44] R. Santoro et al. "Qualification of a Silicon Photomultiplier scalable readout system". In: *Abstract N-09-039 in 2021 IEEE NSS MIC Yokohama Japan*, (2021).

[45] Gaetano Poma et al. *Single-Photon Spectroscopy With A Flexible Front-End Readout System For The Radioactive Waste Monitoring*. July 2022.

[46] "AN8288 - Measurement of Cosmic Ray Energy Loss in Plastic Scintillators with A5202". In: *CAEN SpA, Viareggio(LU), Italy* (2021). URL: www.caen.it/products/a5202.

[47] V. Arosio et al. "Development of a Silicon Photomultiplier toolkit for science and education". In: 10.07 (July 2015), p. C07012. DOI: 10.1088/1748-0221/10/07/C07012. URL: https://dx.doi.org/10.1088/1748-0221/10/07/C07012.

[48] T. Szczesniak et al. "MPPC arrays in PET detectors with LSO and BGO scintillators". In: *IEEE Transactions on Nuclear Science* 60 (June 2013). DOI: 10.1109/NSSMIC.2011.6152589.

[49] S David et al. "Imaging performance of silicon photomultipliers coupled to BGO and CsI:Na arrays". In: *Journal of Instrumentation* 8.12 (Dec. 2013), P12008. DOI: 10.1088/1748-0221/8/12/P12008. URL: https://dx.doi.org/10.1088/1748-0221/8/12/P12008.

[50] "UM3244 - DT5720 User Manual". In: *CAEN SpA, Viareggio(LU), Italy* (2021).

[51] "Crystal Materials Data Sheet". In: *Hilger, Margate, England, UK* (2017). URL: www.dynasil.com/knowledge-base/crystal-materials-index.

[52] "MPPC S13360-6050CS Data Sheet". In: *Hamamatsu, Shizuoka, Giappone* (2016). URL: www.hamamatsu.com/eu/en/product/type/S13360-6050CS/index.html.

[53] "A525X - Adapters for FERS-5200 Board Inputs Data Sheet". In: *CAEN SpA, Viareggio(LU)* (2021). URL: www.caen.it/products/a5202.

[54] "UM7946 - Janus Software User Manual". In: *CAEN SpA, Viareggio(LU), Italy* (2021). URL: www.caen.it/products/a5202.%20Accessed%20on%20February.

[55] "'DS2626 - SP5600 SP5600 Power Supply and Amplification Unit Data Sheet". In: *CAEN SpA, Viareggio(LU), Italy* (2018). URL: www.caen.it/products/sp5600c.

[56] "DPP-CI for SiPM User Guide". In: *CAEN SpA, Viareggio(LU), Italy* (2010). URL: www.caen.it/products/sp5600c.%20Accessed%20on%20February.

[57] "'MPPC (SiPM) Linearity". In: *Hamamatsu, Shizuoka, Giappone*, (). URL: www.hamamatsu.com/us/en/resources/interactive-tools/mppc-sipm-linearity.html.

List of Figures

List of Tables